UNIVERSITÀ
DEGLI STUDI
DI BRESCIA

DOTTORATO DI RICERCA IN INGEGNERIA DELL'INFORMAZIONE

FIS/01 FISICA SPERIMENTALE

CICLO XXXV

SIMULATIONS AND RECONSTRUCTION OF ANTIPROTON-MATTER ANNIHILATION EVENTS IN ANTIMATTER EXPERIMENTS

Dottorando:
Dr. Giovanni Costantini

Supervisore:
Prof. Luca Venturelli

Se fossi nato senza sogni,
avrei avuto meno rimpianti
e meno dolori,
ma sarei nato cieco.

Contents

Riassunto

Il Modello Standard (SM) è ad oggi la teoria più completa che siamo riusciti a formulare per descrivere i componenti fondamentali del nostro universo e le loro interazioni. Con essa è possibile descrivere con grande precisione un'incredibile quantità di fenomeni. Spesso viene citata come esempio la previsione dell'anomalia del momento magnetico del muone o dell'elettrone, due delle previsioni più accurate della fisica, confermate sperimentalmente fino al dodicesimo ordine di grandezza. È ben noto, tuttavia, che il Modello Standard non è né completo né pienamente compreso.

Un chiaro esempio dell'incompletezza dello SM è l'incapacità di spiegare l'asimmetria tra la quantità di materia e antimateria osservate su scala cosmologica. Non vi sono infatti osservazioni di alcun tipo di segnale astronomico che indichino la presenza di sistemi di antimateria. Lo SM tuttavia prevede l'antimateria e in particolare la descrizione di quest'ultima è totalmente simmetrica rispetto a quella della materia ordinaria. Si pensa quindi che inizialmente le quantità di materia e antimateria dovessero essere create in egual quantità. Poiché l'antimateria e la materia si annichilano entrando in contatto, per spiegare l'assenza di antimateria nell'universo si può ipotizzare l'esistenza di un meccanismo non previsto dal Modello Standard che favorisca la produzione di materia rispetto all'antimateria. Un possibile meccanismo sarebbe la violazione di una simmetria ritenuta fondamentale e inviolata, la simmetria CPT (Charge, Parity, Time). Per questo motivo sono nati molti esperimenti per cercare di osservare questa violazione.

I progetti presentati in questa tesi sono inquadrati all'interno di un esperimento che indaga questo particolare tema di ricerca. ASACUSA (Antimatter Spectroscopy And Coherent Upward-going Scattering experiment) è un esperimento che si svolge al CERN e che mira a indagare diversi aspetti dei sistemi di antimateria. La collaborazione porta avanti diversi progetti in parallelo. Il principale si focalizza sulla misura di spettroscopia iperfine dell'antidrogeno per confrontare la sua struttura iperfine con quella ben conosciuta dell'idrogeno. Questo è un ottimo test per una possibile violazione della simmetria CPT. Ciò che caratterizza ulteriormente la misura iperfine a cui ASACUSA mira è che positroni e antiprotoni sono intrappolati e mescolati in modo da creare un fascio di anti idrogeno che viene poi polarizzato. Questa configurazione permette di effettuare una misura di spettroscopia iperfine lontano da qualsiasi campo magnetico che possa disturbare la misura. Negli ultimi anni inoltre, parallelamente agli obiettivi principali della collaborazione, sono stati avviati degli studi per caratterizzare i prodotti delle annichilazioni lente dell'antiprotone.

In questa collaborazione ho contribuito negli anni sia alla messa a punto e all'aggiornamento della parte hardware sia a vari progetti di analisi e simulazione dei dati. In particolare, in questa tesi, presenterò due contributi realizzati nell'ambito del progetto di annichilazione lenta di antiprotoni e della misura di spettroscopia dell'antidrogeno.

Il primo riguarda lo sviluppo di simulazioni Monte Carlo per lo studio dei prodotti

dell'annichilazione lenta di antiprotoni su diversi materiali e inoltre la digitalizzazione di queste e altre simulazioni di questa misura. L'obiettivo di questa ricerca è quello di caratterizzare al meglio, attraverso misure sperimentali, i prodotti di annichilazione dell'antiprotone sul nucleo. Questi processi sono essenziali per la maggior parte delle misure nel campo dell'antimateria a bassa energia e, inoltre, i modelli che vengono utilizzati nei software di simulazione Monte Carlo si basano su estrapolazioni dai dati sperimentali per riprodurre questi processi a basse energie. La collaborazione ASACUSA aveva appena terminato la raccolta dei dati per questa ricerca all'inizio del mio dottorato. Il passo successivo e finale per completare questa prima fase dello studio è stato quello di sviluppare simulazioni Monte Carlo che riproducessero la misura effettuata e quindi digitalizzare i dati simulati. In questo modo sarà possibile confrontare i dati reali con quelli simulati attraverso diversi modelli teorici.

Il secondo è l'implementazione del software di ricostruzione del segnale per il rivelatore a barre scintillanti usato per la calibrazione della fase di creazione dell'anti-idrogeno. Questo rivelatore chiamato DANTE (Detector for ANnhilation of Tracking Experiments), nell'ultimo anno è stato sottoposto a un aggiornamento completo, sia hardware che software, per l'utilizzo nel prossimo periodo di acquisizione dei dati. Dato l'aggior-namento che DANTE ha subito, è stato necessario implementare un software di ricostruzione delle tracce delle particelle. Questo contributo è di fondamentale importanza per il processo di misurazione della spettroscopia dell'anti idrogeno. Il rivelatore DANTE viene attualmente utilizzato per tracciare i pioni e altri prodotti di annichilazione nell'area di mixing di positroni e antiprotoni dell'esperimento. Ciò consente di monitorare il plasma di antiprotoni in questa fase delicata.

La tesi si sviluppa come segue: nel primo capitolo introduco alcuni concetti relativi al campo di ricerca sull'antimateria e alcuni tratti generali che caratterizzano la ricerca sperimentale in fisica delle particelle. Nel secondo mi concentro sulla descrizione dei due progetti di ricerca svolti in ASACUSA dove si inquadra il mio contributo all'esperimento. Nel terzo capitolo capitolo descrivo l'apparato sperimentale di ASACUSA. Dedico poi gli ultimi due capitoli ai due progetti sviluppati in questo lavoro di tesi. Concludo quindi con un riassunto dei risultati e menzionando alcuni possibili sviluppi di questi progetti. Del materiale aggiuntivo è riportato nelle due appendici dedicati ai due progetti.

Summary

The Standard Model (SM) is to date the most comprehensive theory describing the fundamental components of our Universe and their interactions. With it, an incredible amount of phenomena can be described with great precision. Often brought up as an example, the predictions of the magnetic momentum anomaly of the muon and electron have been two of the most accurate predictions in physics, experimentally confirmed up to the twelfth order of magnitude. It is well known, however, that the Standard Model is neither complete nor fully understood.

An important example of the SM incompleteness is the inability to explain the observed matter-antimatter asymmetry on a cosmological scale. The inconsistency between observation and theory in this case concerns the fact that a substantial amount of antimatter is not observed in the universe. The SM actually predicts antimatter and in particular the description of the latter is totally symmetrical with that of ordinary matter. Considering the fact that antimatter and matter annihilate by coming into contact, there should be a mechanism not introduced in the standard model that favors the production of matter over antimatter. One possible mechanism would be a violation of a symmetry that is believed to be fundamental and inviolated, the symmetry under inversion of Charge, Parity and Time (CPT). Hence many experiments have been proposed in order to try to observe this violation.

The projects I am presenting in this thesis are framed inside an experiment that deals with this particular research subject. The Antimatter Spectroscopy And Coherent Upward-going Scattering experiment (ASACUSA for short) is held at CERN and it aims to investigate several aspects of antimatter systems. Its collaboration carries on several projects. The main one focuses on hyperfine antihydrogen spectroscopy measurements, in order to compare the hyperfine structure of antihydrogen with the well known one of hydrogen. This is a test for possible CPT symmetry violation. What characterizes further the hyperfine measurement that ASACUSA is aiming for is that positrons and antiprotons are trapped and mixed so to create an antihydrogen beam that is then polarized. This configuration permits to make a spectroscopy measurement of the hyperfine structure of the ground the state of antihydrogen far away any magnetic field that can reduce the precision of the measurement.

In the last years, in parallel with the main goals of the experiment, another line of reaserch started. With the same apparatus used for the antihydrogen spectroscopy measurement a study aiming at the characterization of the products of antiproton annihilation at rest is carried out.

In this collaboration I have contributed over the years both to the set-up and upgrade of the hardware part and to various data analysis and simulation projects. In particular, in this thesis, I will present two main contributions carried out within the framework of the slow antiproton annihilation project and the antihydrogen spectroscopy measurement.

The first concerns the development of Monte Carlo (MC) simulations for the study of slow

antiproton annihilation products on different materials and then the digitization of the resulting energy depositions of these MC simulations. The goal of this research is to determine as best as possible, through experimental measurements, the distributions of the annihilation products of an antiproton on a nucleus. The annihilation processes are essential for most measurements in the field of low-energy antimatter and, in addition, the models on which the MC simulation software is based rely on extrapolations from experimental data to reproduce these processes at low energies. The ASACUSA collaboration had just finished taking data for this research at the beginning of my Ph.D activities. The next and final step to complete this first phase of the research was then to develop Monte Carlo simulations that reproduce the measurement and then simulations of the digitization of the signal itself, in order to compare the data obtained with the models presently used in Monte Carlo simulation software.

The second concerns the implementation of a signal reconstruction software for the scintillating bar detector used for the calibration of the creation phase of antihydrogen. This detector, called DANTE (Detector for Annihilation Tracking Experiment), has undergone a complete upgrade in the last year, both hardware and software to be used in the next data taking period. After the upgrade that DANTE underwent, it was necessary to implement a tracking reconstruction software. This contribution is of fundamental importance for the anti-hydrogen spectroscopy measurement. The DANTE detector is currently being used to track pions and other annihilation products in the positron and antiproton mixing area of the experiment. The software makes it possible to monitor the cloud of antiprotons at this delicate stage.

The thesis is developed as follows. In the first chapter, I introduce the research of antimatter at low energy and some general features that characterize experimental research in particle physics. In the second chapter I will focus on the two lines of research carried out in ASACUSA, where my contribution is framed. In the third chapter, I will describe the experimental apparatus of ASACUSA. I will then devote the last two chapters to the two projects developed in this thesis. I will conclude with a summary of the results and mentioning some further possible developments of these projects. Some additional material about the projects can be found in the appendixes.

Chapter 1

Introduction

In this first chapter I will briefly go through two more technical arguments, which are peculiar of the work of a particle physicist *i.e.* Monte Carlo simulation and detector signal reconstruction. I will then introduce the research field of antimatter at low energy and finally the ASACUSA experiment.

1.1 Monte Carlo methods and signal reconstruction

Before talking about the physics of my research, I will discuss two fundamental aspects that are characteristic of the work of particle physicists, about which I knew very little before I embarked on my research journey in this field. These are the Monte Carlo methods used for the simulation of particle propagation and the problem related to the reconstruction of a detector signal. While I will not provide a formal and precise treatment of these topics, I will provide a brief overview of them, as they form an integral part of my thesis work.

1.1.1 Monte Carlo methods and other types of simulations

Let us begin by discussing Monte Carlo (MC) siFmulations. Firstly, it is important to define what Monte Carlo methods and Monte Carlo simulations are. While there are various definitions of Monte Carlo methods that can be found in litterature, from the most unformal one:

> *Monte Carlo methods are like pornography: no official definition exist, however those who have seen them know what they are about.*
>
> Wlodek Tomasz in [1]

to the most rigorous ones. One of the most commonly accepted definitions in the field of physics is that the Monte Carlo method is a computational technique that uses random sampling to obtain numerical results. In essence, Monte Carlo simulations use computer programs to model and simulate the behavior of a system or process under various conditions. This means that instead of performing long complex calculations, one wants to perform large number of *experiments* using random number generation and see what happens.

A classic example used to explain the application of Monte Carlo methods is the calculation of π. Given a square of side 1 with a quadrant inscribed within it, one can scatter a uniform number of points over the square and count the number of points within the quadrant (i.e., with a distance from the origin less than 1). The Monte Carlo theory states that the ratio of the inside-count and the total-sample-count is an estimate of the ratio of the two areas, $\pi/4$. The accuracy of the result depends solely on the number of randomly drawn dots inside the square. Various methods exist for randomly selecting points inside the square.

In particle physics, Monte Carlo simulations are used to tackle a plethora of complex problems, many of which are unsolvable through conventional means. Monte Carlo simulations are particularly useful in two aspects of particle physics:

- Monte Carlo simulation is used for event generation.
- Monte Carlo simulation is used for detector response simulation.

As experimental particle physicists, we are particularly interested in the second application. In this type of application, Monte Carlo methods are used to compute the probabilities of interactions between particles and various materials that make up the materials of the experimental apparatus. An experiment can be viewed as a large series of individual events, each with its own probability distribution and each influencing some events and being influenced by others. Each event can give rise to energy deposition, creation of other particles through decays or collisions, and so on. This can be seen as a large integral over a probability distribution that lives in a huge parameter space. Ultimately, we are also calculating an area. If we return to the example of calculating π, all possible outcomes of our experiment are represented by the square inside which we can draw points, and an experimental physicist is interested in seeing how much the area of the figure inscribed in the square is.

To deal with this problem, a variety of simulation programs have been developed and extensively optimized by research groups that specialize in this field. The most widely used and well-known simulation programs in the field of particle physics are Geant4 and FLUKA, both of which are developed and maintained at CERN.

In general, particle physicists use Monte Carlo simulations for the following purposes:

1 To evaluate the cost of an actual experiment in terms of money, time, or safety hazards such as radioactivity or building requirements.

2 To evaluate the outcome of an experiment in order to assess the feasibility of a measurement, including background estimation and event selection.

3 To evaluate the performance of a new detector, as part of research and development (R&D) efforts.

4 To estimate detector effects on the measurement.

Monte Carlo simulations are indeed essential tools for the work of particle physicists. In this thesis, we will use Monte Carlo simulations both for reason number 3, when evaluating the efficiency of a detector signal reconstruction software in chapter 5, and for reason number 2 in chapter 4. However, as we shall see, in our case, it is the Monte Carlo simulation software that will be tested, rather than the other way around.

Unfolding

Speaking of Monte Carlo simulations, I must also briefly mention the *unfolding* procedure. While MC simulations are a powerful tool that allows us to reproduce natural behaviors as seen through the eyes of our detectors, they cannot show us the reverse path. Given the distributions of various observables that characterize the process being studied, the MC simulation process can show how the presence of the detector changes those distributions. However, through a Monte Carlo simulation, we cannot reproduce the opposite effect. That is, starting from distributions of observables that contain the effect of a given scientific apparatus, we cannot derive the underlying distributions that characterize the natural process. This type of analysis is called unfolding because we try to ”unfold” the detector effect on the natural process we are observing.

In essence, unfolding refers to the process of extracting the ”true” distribution of a physical process from the observed distribution, which is distorted by the detector response. This is achieved by using an iterative technique that involves comparing the observed distribution to the MC -simulated distribution and modifying the simulated distribution until it matches the observed distribution. The resulting unfolded distribution represents the ”true” underlying distribution of the process, corrected for the detector effect.

This is a fundamental step for comparing different experiments. The process of unfolding attempts to remove the dependence of observations on the specific apparatus and techniques used to obtain them. The effects of a detector that need to be considered in an unfolding procedure are primarily two: efficiency and smearing. The former reduces the number of hits, either through acceptance effects (i.e., particles that do not pass through the sensitive areas of the detector) or through efficiency effects (i.e., the particle passes, but the detector fails to detect it). These effects distort the distributions of observables that characterize the data. Throughout this thesis, we will demonstrate a simple application of unfolding in chapter 4.

1.1.2 Signal reconstruction

The other aspect discussed in this introduction is that of signal reconstruction. This is a complex process that involves several steps, including the mechanisms of electrical signal creation, the processes of analog signal acquisition and conversion to digital signals, and so on. In this thesis, we focus on what is perhaps one of the final steps: the reconstruction of the acquired signal. Specifically, we aim to reconstruct the paths traveled by charged particles, also known as tracks. Generally, a particle physics experiment is equipped with detectors that are specifically designed to provide spatial information about the path of the charged particles.

The variety of experimental setups has led to the development of different pattern recognition methods that cannot be easily compared. The factors on which a reconstruction algorithm depends may vary depending on the type of experiment (fixed target or collider), the types of tracking detectors (linear single-coordinate measurements, radial single-coordinate measurements, stereo angles, etc.), and more. An excellent review on this subject is provided by [2]. It is remarkable that even today, no generally accepted standard software package exists that can perform track finding in a variety of detector setups, a situation that is in marked contrast to the detector simulation software I mentioned earlier.

The problem of signal reconstruction is typically broken down into three steps, which are dealt with separately and in succession:

- Pattern recognition
- Track fitting
- Vertex finding

In the first step, an algorithm attempts to identify and group the hits left by the same particle as it passes through the various layers of detectors. In the second step, it finds the best track that fits these hits, taking into account magnetic fields and other factors that may influence the particle trajectory. Once the tracks have been reconstructed, the final step involves reconstructing the vertex from which the various particles originated, again using a fitting algorithm.

1.2 Antimatter and the ASACUSA experiment

Having introduced some general themes that are common to various branches of research in particle physics, let us now turn our attention to a more specific topic that is relevant to my thesis work.

The study of low-energy antimatter in particle physics is certainly not a recent field. The work and advances made from the first half of the last century to the present day are now exploring several different and interesting directions. In this section, I will introduce some general aspects of low-energy antimatter physics, which will provide a framework for the ASACUSA experiment.

1.2.1 Low-energy antimatter

When we talk about antimatter, we are first talking about antiparticles, since the definition of antimatter is essentially based on them.

Everything started back in 1928, when the British physicist, Paul Dirac successfully integrated the two main theories of our epoch: quantum mechanics and special relativity, in a single theory [3], [4]. This unification came with an unexpected result: the existence of negative energy states of the quantum fields of the theory, or as we call them now, antiparticles. In his famous equation describing relativistic electrons, negative energy quantum states were predicted, leading to the creation of what he said to be

> *A new type of particle with the same mass as an electron but with an opposite charge. We can refer to this particle as an anti-electron. We do not expect to find any of these in nature.* (Paul Dirac in [5])

However, some years later, in 1932, an experimental physicist named Carl David Anderson discovered what he called the positron (e^+), which is the antiparticle of the electron and is produced in cosmic rays [6]. Figure 1.1 shows the well-known image of a positron passing through a lead bar in a bubble chamber that was used for detection. This discovery prompted a search for the possible antiparticle of the proton, which is the antiproton ($\bar{p}$). It was not until the creation of the first particle accelerator, the Bevatron accelerator, at Lawrence Berkeley National Laboratory in 1955, that the antiproton was artificially produced and observed [7]. Figure 1.2 shows a bubble chamber image of one of the recorded events. Dirac's discovery does not stop at the electron or the proton; rather, we can state that for each particle, there exists an antiparticle having the same mass but opposite charges. I use the plural for *charges* since I am not only referring to the electromagnetic charge but also to all charges (color charges, weak isospin, etc.) that characterize a particle. In the years after the discovery of the antiproton, many more particles were found. This was one of the confirmations that the Standard Model (SM) is, indeed, the best theory we have to describe the quantum world.

When one talks about antimatter, one can be referring to various physical systems. In general, I will refer to antimatter when antiparticles, particularly antiprotons and positrons, are involved at low energies. In this field, low energies mean energies that can go from the order of MeV down to molecular energies of the orders of eV. These are the energies that are needed to create complex systems of antimatter, such as antihydrogen. Antihydrogen was

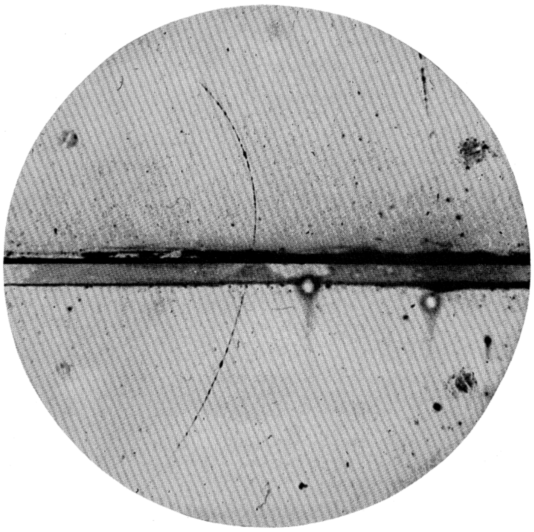

Figure 1.1: A photo of the Bubble chamber where a positron can be seen crossing the lead bar in the centre of the chamber [6].

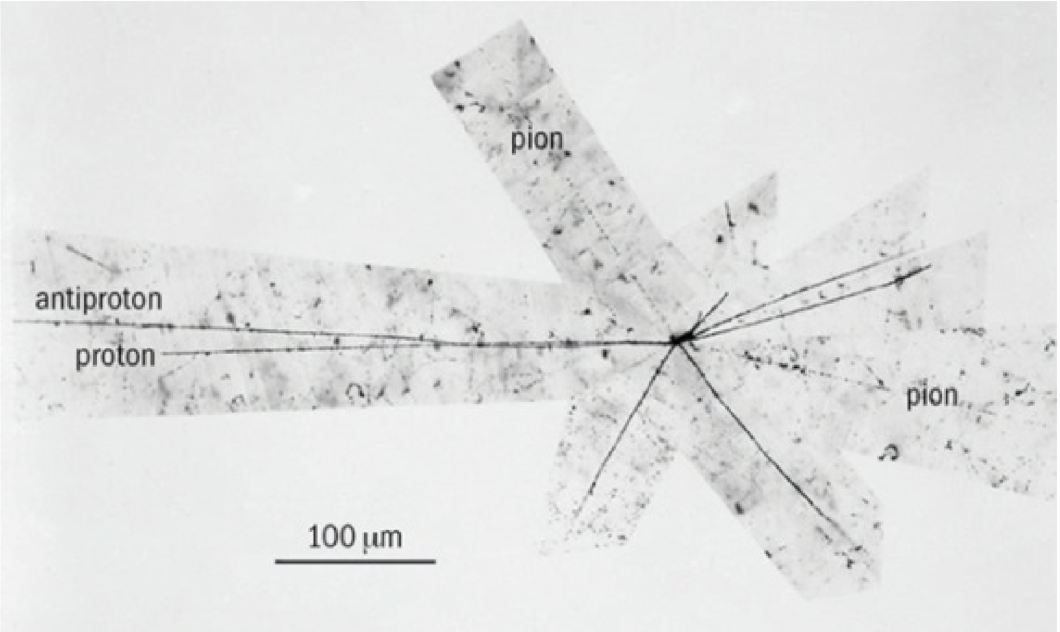

Figure 1.2: A photographic-emulsion exposure where the scattering between a proton and an antiproton and the generation of annihilation products can be seen [8].

first created only in the late 1990s, while the field of antimatter research arose much earlier, just after the discovery of antiprotons.

Following the discovery of the antiproton in 1955 , beams of high energy $\bar{p}$ were rapidly developed, and a first survey of antiproton annihilation on protons or neutrons was possible as early as in the 1960s, by stopping antiprotons in hydrogen- and deuterium-filled bubble chambers. These experiments demonstrated that $\bar{p}p$ annihilation is a powerful tool to discover meson resonances, even though only limited statistics were achieved. Two main experiments were carried out at that time: the first one at Brookhaven by a group from Columbia University and the other at CERN, the European Organization for Nuclear Research. After these two experiments, the physics of antipronts concentrated on the study of $\bar{p}p$ collision at high energy. Several colliding experiments were performed at CERN in the SPS accelerator, where center of mass energy can reach up to 400 GeV. An entire complex called the $\bar{p}$-Complex was developed. Here techniques for accumulation and stacking of large numbers of antiprotons were developed.

In this same complex, the study of antipron at lower energies were developed during the 1980, thanks to the availability of cooled antiproton beams, which were provided thanks to the construction and operation of the LEAR (Low Energy Antiproton Ring) facility. The LEAR facility was constructed at CERN to handle pure antiproton beams in the momentum range from 105 to 2000 $\frac{\text{MeV}}{\text{c}}$ with small physical size and a typical momentum spread of $\Delta p/p \approx 0.1\%$. The LEAR project was approved by CERN in 1980, and in July 1983, the first antiproton beams were delivered to users. After a break in 1987 to construct a new antiproton collector (ACOL) which resulted in a flux gain of a factor of 10, the facility was operated until the end of 1996, when it was closed for financial reasons. Among the numerous experiments held at LEAR, some of the most notable ones were Asterix, Obelix, and Crystal Barrel (CBAR).

With the successor of LEAR, the Antiproton Decelerator (AD) at CERN, we reach the present day. This facility is the unique facility in the world involving antiprotons at low energies nowadays. The AD is a particle decelerator that slows down antiprotons so that they can be trapped and studied in detail or to be used to create more complex antimatter systems. I will give some details about this facility in the next chapter. Several experiments were and are carried out here, including ATHENA [9], ACE [10], ATRAP [11], ASACUSA [1], ALPHA[2] [12], AEgIS[3] [13], GBAR[4] [14], BASE[5] [15], and PUMA[6] [16]. Some of them are already completed (ATHENA, ACE, ATRAP), PUMA is almost ready to start, and the others are still ongoing. All these experiments explore, or explored, different aspects and properties of antiproton and antimatter systems at MeV and keV energies, including possible uses of

---

[1] https://home.cern/science/experiments/asacusa

[2] https://home.cern/science/experiments/alpha

[3] https://home.cern/science/experiments/aegis

[4] https://home.cern/science/experiments/gbar

[5] https://home.cern/science/experiments/base

[6] https://home.cern/science/experiments/puma

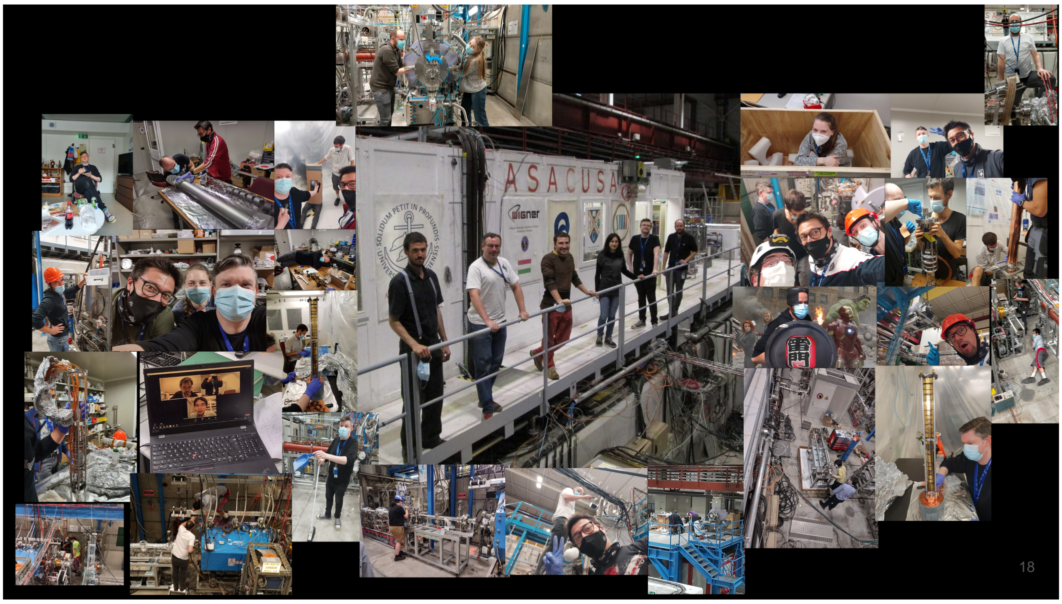

Figure 1.3: Collage of photos of some members of the ASACUSA collaboration. Due to the Covid-19 pandemic period, it was not possible to take a group photo with all members of the collaboration in recent years.

antimatter, such as medical applications.

Nowadays almost every experiment aims to confine and trap antiparticles in order to create antiatoms and study their properties. As we will see, one of the main goals of studying antimatter nowadays is to understand why our universe is made almost entirely of matte: since the laws of physics suggest that matter and antimatter should have been created in equal amounts during the Big Bang and since matter and antimatter annihilate one with each other, there shouldn't be an excess of one type over the other. Moreover the asymmetric properties observed between matter and antimatter do not explain the predominance of the matter on antimatter. Another reason is related to the quantization of gravity and the testing of possible variations of antimatter behavior in a gravitational field. We will not explore these latter lines of research since they are not related to the ASACUSA scientific program.

1.2.2 ASACUSA

ASACUSA, which stands for Antimatter Spectroscopy And Coherent Upward-going Scattering, is a collaboration among several institutions, including CERN, INFN, the universities of Tokyo and Hiroshima, RIKEN laboratory, the Stefan Meyer Institute in Vienna, and the universities of Milano and Brescia. In Figure 1.3, I have included a picture of some of the members of the collaboration.

The main goal of ASACUSA is to compare the spectra of antihydrogen and ordinary hydrogen atoms to determine whether there are any differences in their spectra. This could help us understand whether antimatter systems behave in the same way as ordinary matter, or if there are fundamental differences between the two that would result in a violation of CPT symmetry. In addition to studying the spectrum of antihydrogen atoms, ASACUSA is also conducting other experiments on different antiparticle systems or antiparticles.

In summary, the scientific program of ASACUSA consists of:

- The aforementioned experiment on the production and hyperfine spectroscopy of the ground state (GS-HfS) of the antihydrogen atom, aiming to test for CPT symmetry.
- Laser spectroscopy of antiprotonic helium, which also tests CPT symmetry and precisely measures the mass ratio between $\bar{p}$ and the electron [17].
- Study of antiproton annihilation cross-sections. Measurements of atomic and nuclear collision cross-sections of antiprotons at low energies ($5.3\,\mathrm{MeV}$) [18].
- Fragmentation studies in antiproton-nucleus annihilations.

ASACUSA is not the only experiment that conducts $\bar{H}$ spectroscopy measurements; recently, the GS-HfS frequency of $\bar{H}$ was measured with a relative precision of $\approx 4 \times 10^{-4}$ in a magnetic trap [19]. However, what sets ASACUSA measurement apart is the creation of an antihydrogen beam. The presence of a strong magnetic field can indeed limits the experimental precision of a GS-HfS measurement. In ASACUSA, the interaction region with microwave is a low magnetic field environment, where external magnetic fields can be reduced to $1\,\mu$T [19] with sufficient uniformity for the spectroscopy experiment. This is achieved thanks both to the $\bar{H}$ beam used to bring the antiatoms away from the strong magnetic field needed for the confinement and also to an adequate shielding of the spectroscopy region.

Chapter 2

ASACUSA-CUSP measurements: $\bar{H}$ spectroscopy and $\bar{p}$ annihilation at rest

In this chapter, I will focus on presenting and describing two out of the three primary areas of research that are currently being pursued by the ASACUSA collaboration. I will first explain the theoretical bases behind each of these investigations, and then describe how these measurements are carried on.

2.1 Antihydrogen and the CPT theorem

This section is devoted to explaining the theoretical justification for measuring the hyperfine structure of antihydrogen. I will introduce the concept of CPT symmetry, provide a brief review of the hyperfine structure of hydrogen, and then explain how these two topics are related and why measuring the hyperfine structure of antihydrogen can serve as a test for CPT violation.

2.1.1 About the CPT theorem

For every particle, there is a corresponding antiparticle with identical properties (such as mass and lifetime) and opposite charges sign. Moreover, when a particle interact with its corresponding antiparticle, they annihilate producing other particles. When instead, particle and antiparticle are created from a reaction, there is always a symmetry between the created particle and the corresponding antiparticles, so that the quantum numbers are conserved.

The complete symmetry between particles and antiparticles, both in their properties[1]

---

[1] in saying properties I am omitting the well known CP violation, which is indeed an asymmetry between matter and antimatter. Here I am referring to charges and masses.

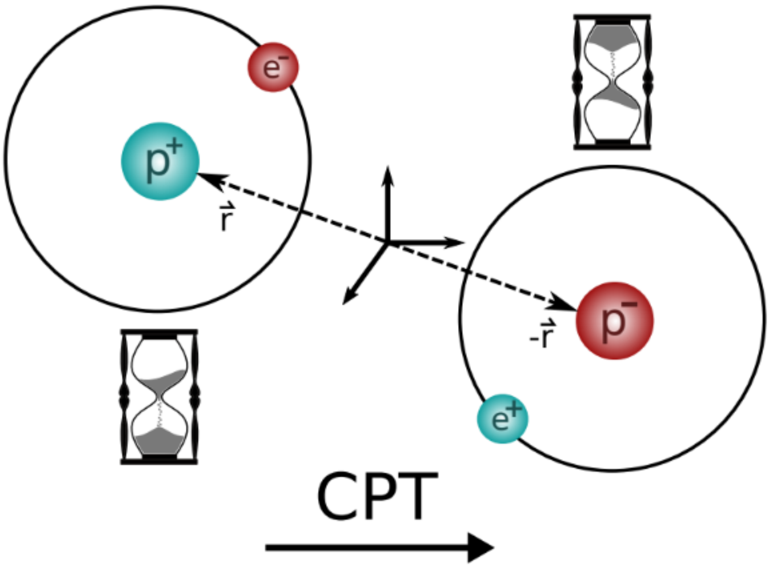

Figure 2.1: Illustration of the CPT transformation on the hydrogen system. C exchanges the charges of the particles, thus particles become their antiparticles, P reflects all spatial coordinates $\vec{r} \to -\vec{r}$ and T reverses time $t \to -t$. Image from [21]

and in the creation and annihilation processes, appears in stark contrast with a well-known astronomical fact: the excess of matter and the lack of large amounts of antimatter in the visible Universe. This is also known as the baryon asymmetry [20]. Initially, it was thought that the reason for this asymmetry was the result of the Universe initial conditions. However, as the Big Bang theory became more widely accepted, it became clear that matter and antimatter should have been produced in equal amounts at the beginning of the Universe.

This raised the question of whether there might be a difference between particles and antiparticles that could explain the baryon asymmetry. In 1967, the physicists Andrej Dmitrievič Sakharov stated that there are three necessary conditions that a theory has to have in order to explain this imbalance [22]:

- C and CP violation,
- violation of baryon number,
- interactions outside of thermal equilibrium.

C and CP violations refer to the violation of discrete symmetries in particle physics. A theory can have several discrete symmetries, including parity (P) symmetry, which means a process is invariant under space inversion, and charge (C) symmetry, which means a process is invariant under charge change (or particle-to-antiparticle swapping). CP symmetry refers to the symmetry of a process under both P and C inversions. Time symmetry (T) refers to the symmetry of the process under time reversal. CPT is the combination of all these three symmetries. Figure 2.1 illustrates the CPT symmetry transformation applied to hydrogen. Although violations of C, P, and CP have been observed, their magnitudes are not sufficient to explain the baryon asymmetry [23]. The violation of the baryon number in microscopic processes has never been observed so far [24].

The Sakharov hypothesis was based on the fact that the CPT symmetry was not violated, and indeed, the Standard Model does not allow for such a violation. No violation of the combination of C, P, and T symmetries all together has ever been observed so far. However, if observed, a CPT violation could be a possible explanation for the baryonic asymmetry by itself without requiring the Sakharov hypothesis. Since the Standard Model does not allow

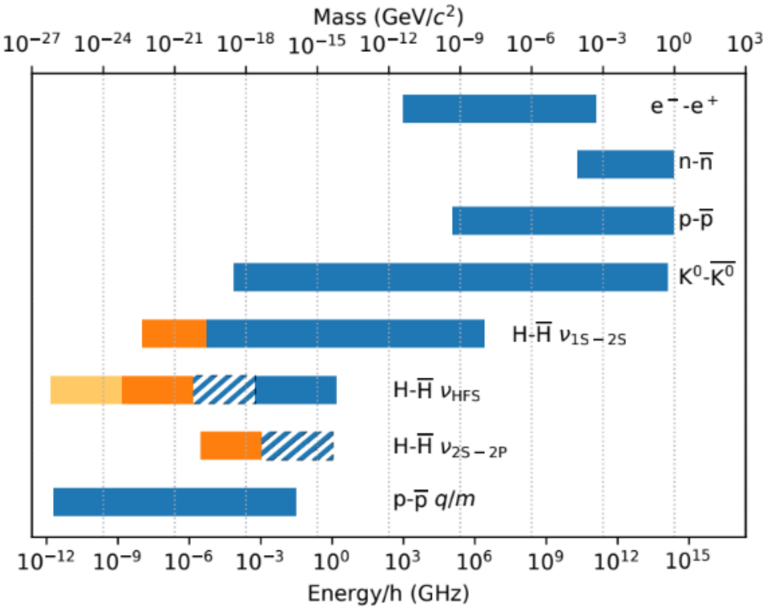

Figure 2.2: List of some of CPT testing experiments. Plot from [25]. Blue bars show existing tests, on the right side of each bar the systems used for the test. The length of the bar indicates the relative precision of the CPT test, the left hand side is the sensitivity on an absolute energy scale. For the $H{-}\bar{H}\nu_{1S\text{-}2S}$ measure, orange indicates the precision achieved for the matter system and therefore the potential sensitivity currently reachable. For hyperfine transition frequencies ν_{HFS} of H/H: striped, blue extended bar symbolises the initial goal of ASACUSA. Orange marks the precision due to the line width for an atomic fountain and the light orange the precision reached by the hydrogen maser experiment. For the Lamb shift ($H{-}\bar{H}\nu_{2S\text{-}2P}$): estimated achievable accuracy (striped, blue extension).

for CPT symmetry violation, a theory that includes such violation is needed. There is a fervent field of research studying extensions of the Standard Model to include what cannot yet be described with the SM. One of these theories that will eventually replace the SMis likely to include new physics and associated phenomena in the low energy region [26]. These phenomena are highly suppressed due to the large energy difference between low energies and the Planck scale [27]. A CPT observation would be extremely interesting to shed light on possible SME.

Since CPT violation needs a theory that goes beyond the SM, tests measuring different quantities can be compared within theories that go beyond the SM, acting as a common theoretical framework [28, 29]. In particular I will discuss about the class of theories known as Standard Model Extension (SME) Lagrangian that incorporate CPT and Lorentz violating terms. The coefficients of this Lagragian have the dimension of energy and need to be determined experimentally. Due to the dimensionality of coefficients the absolute precision of experiments becomes important.

This motivates the experimental testing of CPT symmetry.

High-precision experiments may offer a promising avenue to search for potential violations of CPT symmetry. The CPT theorem predicts that atoms and their antiatoms possess identical spectra, and any discrepancy between the two would indicate physics beyond the Standard Model. The simplest atom, hydrogen, has played a pivotal role in advancing our understanding of atomic spectra and verifying physical theories. In particular, the hyperfine transition frequency, ν_{HFS}, of hydrogen has been measured with exceptional precision, with a relative accuracy of 10^{-12}. As a result, comparing this transition frequency in hydrogen (H) and antihydrogen $(\bar{H})$ offers a highly sensitive test of CPT symmetry.

In Figure 2.2 [25], a set of CPT testing experiments and their respective precisions are presented. Each bar in the figure represents the measured quantity on the right edge, the absolute precision on the left edge, and the relative precision by the length of the bar. As shown in the figure, the most precise CPT testing experiment to date, in relative terms, is the comparison of neutral kaon masses $(K_0 - \bar{K_0})$ with a relative precision of $\Delta m/m \approx 10^{-18}$ [30]. Relative precision however is not the only important quantities when CPT is tested. The absolute precision is also of great importance. Moreover, testing different systems even at lower precision with respect to the one of kaon masses is also important, since CPT violations could occur only in some of these systems. Regarding the tests related to antiprotons and antihydrogen, the measurement comparing the charge-to-mass ratio of proton and antiproton via their cyclotron frequencies in a trap [31] has the largest absolute precision.

The hyperfine transition of H has recently been measured with a relative precision of $\frac{\Delta\nu_{\text{HFS}}}{\nu_{\text{HFS}}} = 3.5 \times 10^{-4}$ in a trap by the ALPHA collaboration [19]. In figure 2.2, the blue bar including the striped extension marked $H{-}H_{\nu HFS}$ indicates the first sensitivity goal of the ASACUSA collaboration of 10^{-6} [25]. Comparing the absolute precisions of the different CPT tests, one can see that a relative precision of 10^{-6} already competes with the mass comparison of neutral kaons.

2.1.2 Antihydrogen and the hyperfine structure

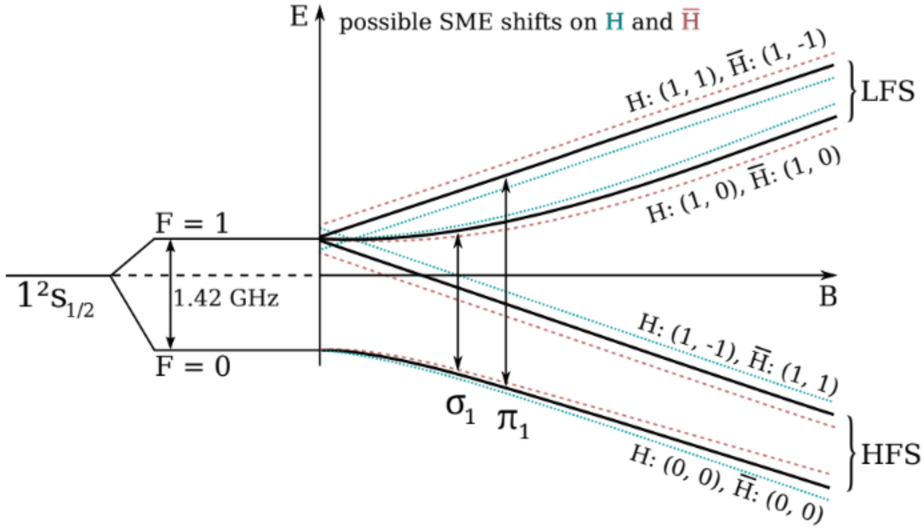

Figure 2.3: Schematic drawing of the hyperfine splitting and Breit-Rabi diagram of $\bar{H}$ and H (black lines). The states with quantum numbers (F, m_F) are indicated for $\bar{H}$ and H. The blue (H) and red ($\bar{H}$) dashed lines show the spectra in the presence of Lorentz and CPT violation in the framework of the SME. The size and sign of the shifts are not predicted by the SME theory, they have to be determined experimentally and can differ in magnitude for hydrogen and antihydrogen. The two transitions measurable within the current ASACUSA setup (σ_1 and π_1) are also reported.

In order to explain the theory under the CPT symmetry test that ASACUSA is aiming to perform, we need to first illustrate hydrogen spectroscopy. A details discussion of the theory presented in this paragraph can be found in [32] for example.

The hydrogen atom is made up of an electron bound to a proton. Both particles have an intrinsic angular momentum or spin with a value of $\frac{1}{2}$. The spin can take two possible values defined here just as up (↑) or down (↓). This means that, there are 4 possible configurations for the proton and electron spin and any state of the hydrogen atom can be written as a linear combination of these states:

$$|\psi\rangle = a\,|\uparrow\uparrow\rangle + b\,|\downarrow\uparrow\rangle + c\,|\uparrow\downarrow\rangle + d\,|\downarrow\downarrow\rangle$$

In the ground state where the coupling of the two total angular momenta (angular momentum plus spin) I and J of the proton and electron respectively is driven only by the spin component, the total angular momentum F of the atom can have only 4 different states. One may compute the values of a, b, c and d for these 4 states. This results in the ground state of hydrogen being split into a singlet state with $F = 0$ and a triplet state with $F = 1$. The transition frequency between these two states in hydrogen has been measured most precisely using a maser experiment, which yielded $\nu_{\mathrm{HFS}} = 1420, 405, 751.768 \pm 0.002$ Hz [33, 34].

The hyperfine transition frequency of hydrogen was also measured using beam spectroscopy in the 1950s with a relative precision of 5×10^{-8} [35, 36]. This result has recently been surpassed by the ASACUSA collaboration, which measured the hyperfine transition frequency of hydrogen using the same beamline designed for antihydrogen experiments with a relative precision of 2.7×10^{-9} [37].

When a magnetic field B is present, the degenerate triplet state splits, and the resulting four energy states shift due to the interaction $-\mu B$ of the magnetic moment μ of the atom with the magnetic field. The behavior of these energy states is described by the Breit-Rabi formulae [38], and the splitting is depicted in Figure 2.3 (black lines). Note that the energy levels of hydrogen and antihydrogen are ordered differently due to the opposite signs of their magnetic moments. The four states can be classified as low-field seeking (LFS) or high-field seeking (HFS) states based on their behavior in an external inhomogeneous field. LFS atoms drift towards lower field regions to minimize their energy, while HFS atoms behave oppositely. This behavior is exploited in antihydrogen experiments to achieve beam polarization, as discussed in Section 2.3.

2.1.3 Testing the Standard Model with antihydrogen

In this section, I will explore the relationship between the Standard Model Extension which involves a Lorentz Invariant Violation (LIV) and the hyperfine splitting of hydrogen and antihydrogen. It is important to note that LIV is not a necessary framework for describing CPT violation, nor does an observation of CPT violation necessarily imply the validity of the LIV. However, the SME can provide insights into what can be expected from spectroscopy measurements of antihydrogen in cases where there is symmetry violation that breaks the Lorentz invariance [39]. The approach presented here is based on the detailed derivation presented in [28].

The Standard Model Extension involving LIV is a general theoretical test framework for studying Lorentz and CPT symmetry violation developed by Alan Kostelecky and colleagues, constructed from three requirements:

- It has to be an effective field theory comprising all established physics *i.e.* the Standard Model and General Relativity.

- LIV has to be implemented via preferred directions, which are modelled by non-dynamical background fields.

- It has to incorporate observer invariance *i.e.* the choice of the coordinate system must not affect physics.

Lorentz violation in the SME can therefore be visualised as an anisotropy of space. Effectively what we want to do is to add all possible coordinate independent, Lorentz-violating terms to the Lagrange density:

$$\mathcal{L}_{SME} = \mathcal{L}_{SM} + \mathcal{L}_{GR} + \delta\mathcal{L} \tag{2.1}$$

Those terms are summarised by δL. For a single fermion ψ, the conventional Dirac Lagrangian is extended [40]:

$$\mathcal{L}_{Dirac,SME} = \frac{1}{2}\psi(\gamma_\mu i\partial_\mu - m_\mu + \hat{Q})\psi \tag{2.2}$$

where $\hat{Q}$ is the sum of all possible terms formed by contracting conventional tensor operators with LIV coefficients, whereas γ_μ denotes the γ-matrices, ∂_μ the four-gradient, m_μ the mass of the fermion. In principle there exists an infinite number of such terms. It is important to note that these coefficients are not parameters of the SME, they need to be measured by appropriate experiments. If all of them are zero, one gets the conventional Lagrangian.

With the inclusion of these extra Lorentz violating terms CPT invariance is no longer ensured since half of the coefficients are CPT odd. In a CPT invariant theory, when we use the Dirac equation to compute the energy levels of hydrogen and antihydrogen (E_i^H and $E_i^{\overline{H}}$) result identical in a CPT invariant theory. However the extra CPT -odd terms shift the energy levels of both atoms deviate resulting in a shift of transition frequencies, depending on the LIV elements we added in $\hat{Q}$. This difference can be seen as a deviation of the frequencies transition:

$$\nu = \nu_0 + \delta\nu, \text{ with } \nu_0 = E_i - E_j \text{ and } \delta\nu = \delta E_i - \delta E_j \tag{2.3}$$

Here, ν_0 denotes the transition frequency without any SME effects and $\delta\nu$ a possible deviation due to a shift of the energy level E_i by δE_i. Something to notice is that the size and sign of δE_i are not predicted by the SME, they need to be determined experimentally and can differ for hydrogen and antihydrogen.

In any case, the SME contributions are expected to be small. The resulting energy shifts caused by these contributions can be calculated using perturbation theory [28]. Rephrased in a hamiltonian formalism, having a SME hamiltonian density $h_{SME}^H = h_H + \delta h_H$ for hydrogen, what we want to compute is the leading order δh_H corrections to the Dirac hamiltonian h_H, given by the possible LIV contributions. Where δh_H has both the contribution from electron and proton $\delta h_H = \delta h_e + \delta h_p$, for hydrogen or positron and antiproton for antihydrogen.

The ground state correction can be derived by the following matrix elements [28], computed with the Clebsh-Gordan coefficients:

$$\langle nFJLm'_F|\delta h_H|nFJLm_F\rangle = \sum_{jm} A_{jm} \langle Fm_F jm|Fm'_F\rangle \tag{2.4}$$

where $|nFJLm_F\rangle$ are the corresponding eigenstates with principal quantum number n, the total angular momentum quantum number of the electron J, the orbital angular momentum quantum number L, the total angular momentum of the atom F and the magnetic quantum number m_F. The weights A_{jm} summarise the relevant (non-relativistic) LIV and CPT odd coefficients of the SME. The expression of A_{jm} can be found in [28]. The effect on the ground state hyperfine levels results to be:

$$\begin{aligned} F = 0: &\qquad \delta E(n, L) = A^H_{00} \\ F = 1: &\qquad \delta E(n, L, \frac{1}{2}, m_F) = A^H_{00} + \frac{m_F}{\sqrt{2}}|\vec{A}^H| \end{aligned} \tag{2.5}$$

The weight A_{00} $(j = m = 0)$ depends only on the quantum numbers n and L and is therefore isotropic. Consequently, isotropic SME coefficients can only be determined by measuring transition frequencies with $\Delta n \neq 0$ or $\Delta L \neq 0$. Those coefficients can therefore not be constrained with hyperfine transitions. For the degenerated state with $F = 1$, the energy shift is a sum of the isotropic and an anisotropic contribution where $\vec{A}$ is a vector formed by anisotropic SME coefficients. $\vec{A}^H$ can be thought of as a background field which couples to the total angular momentum $\vec{F}$ and lifts the conventional degeneracy of the state, therefore resulting in a splitting similar to the Zeeman splitting. The procedure for a hamiltonian density of antihydrogen is analogous. The vector $\vec{A}^{\bar{H}}$ will have a similar composition with respect to $\vec{A}^H$, only that the CPT odd coefficients contained in $\vec{A}^{\bar{H}}$ have opposite sign. The hyperfine transitions with $\Delta m_F = 0$ are insensitive to SME coefficients, that is because those shifts are proportional to Δm_F :

$$\nu = \nu_0 + \Delta m_F|\vec{A}| \tag{2.6}$$

A possible scenario in case of an additional magnetic field B is shown in Figure 2.3. The black lines in the Breit-Rabi diagram show the conventional case whereas the dashed lines show a possible scenario in case of CPT violating LIV contribution for hydrogen (blue) and antihydrogen (red). It should be pointed out again, that the figure shows only one possible example of SME shifts since their magnitude and sign are not predicted by the SME.

Summarising, the main test of CPT within the framework of the SME that the ASACUSA experiment is aiming to exploit using hydrogen and antihydrogen is to measure a possible lift of degeneracy of the $F = 1$ state via a direct comparisons of the transition frequencies of antihydrogen and hydrogen. I have to point out that other paths can be followed to measure such a degeneracy, as it is pointed out in [28]. In parallel to the main measurement, the ASACUSA collaboration is carrying on also other projects. In particular a degeneracy as described above can be observed also exploiting the effect of the earth motion and the magnetic field of the solar system which give rise to annual variations of transition frequencies in hydrogen and/or antihydrogen. Finally, another possible measure consists of a comparison of the π_1 transition at the same absolute magnetic field, but with different orientation with respect to the background fields. Also this measurement is among ASACUSA goals. Details on the accessible SME coefficients within the ASACUSA hydrogen and antihydrogen programme are discussed in [41].

2.2 The spectroscopy antihydrogen experiment

Referring to the hydrogen and antihydrogen spectra discussed in section 2.1.2, the Breit-Rabi formula governs the energy transitions between hyperfine states at different magnetic fields. The ground state hyperfine splitting of antihydrogen can be determined through two methods. The first method involves extrapolating several measurements of the σ_1 transition (for H: $(F, m_F) = (1, 0) \rightarrow (0, 0)$) at different magnetic field strengths to zero magnetic field using the Breit-Rabi formula. The second method involves simultaneously measuring the σ_1 and π_1 transitions (for H: $(1, -1) \rightarrow (0, 0)$) at the same magnetic field strength to determine ν_{HFS} using the Breit-Rabi formulae. To measure such transition frequencies, three things are needed:

1. a spin-polarized source,
2. a spin-flip inducing resonator,
3. a spin selector,
4. a dector to count the number of antiparticles.

This experimental setup employs a standard method to measure the hyperfine splitting of hydrogen and antihydrogen. The process involves directing a polarized beam of hydrogen or antihydrogen through a region containing an oscillating magnetic field (B_{osc}) superimposed with a small, homogeneous magnetic field (B_{hom}). As the atom spin aligns with B_{hom}, a spin-flip is induced when the resonance frequency is met by the oscillating magnetic field. In the third step of the experiment, the atoms are either focused on the detector or deflected by another inhomogeneous magnetic field, depending on whether they are in the

LFS or HFS. By scanning the frequency of B_{osc} and simultaneously monitoring the count rate on the detector, the transition frequency can be determined when the resonance is met. This experimental approach was first used by I. Rabi in 1938 [42] to measure the hydrogen spectrum with an apparatus made of the same basic components.

In the ASACUSA experiment, the antiproton coming from ELENA at 100 keV are accelerated to 120 keV by the drift tube (see section 3.3). Then they are trapped in the Monoenergetic Ultra-Slow Antiproton Source for High-Precision Investigation (MUSASHI) trap. The spin-polarized source of antihydrogen is the CUSP trap, which has a unique magnetic field with a double cusp configuration. This trap will be presented in section 3.4. This trap serves not only to create antihydrogen, but also as a polarization source by focusing and deflecting atoms depending on their spin state, thanks to its cusp shaped magnetic field. ASACUSA then uses a microwave cavity as a spin flip resonator and a sextupole magnet as a spin selector, both of which are described in section 3.5. Once the antihydrogen beam has been exited and polirized, it finally arrive in the detecotr region, where a hodoscope detector used for the tracking, in combination with BGO detector for a better estimation of the annihilation position are used as the detector setup for monitoring the count rate of antihydrogen atoms annihilating. These will be described in section 3.6. A whole scheme of the ASACUSA line can be see in section 3.1 in figure 3.3.

To date, several efforts have been made towards achieving the goal of measuring antihydrogen spectroscopy. ASACUSA has already succeeded in creating a polarized antihydrogen beam and measuring its principal quantum number distribution [43]. As mentioned in the previous chapter, various upgrades have been made to the entire experimental apparatus in recent years [44, 45], and ongoing work is focused on optimizing the new set-up for the final spectroscopy measurement. In particular my contribution to the upgrade of the DANTE detector reported in 5 is part of this optimization phase. DANTE will be used to monitor the plasma used for the creation of the antihydrogen beam and to help the calibration of the new apparatus. To achieve maximum efficiency during the mixing phase, we require as much information as possible about the quantity and position of the particles cloud in the CUSP trap.

2.3 The antiproton annihilation process

The ASACUSA experiment carries on multiple research projects, including the hyperfine splitting measurement of the antihydrogen spectrum and a measurement of the products of antiproton annihilation at rest. In fact, a new line dedicated to this measurement was proposed last year and is currently under development. The depiction of the theory in this section is based on the work in [46].

2.3.1 Overview of the process

Annihilation is a process that occurs at the level of elementary particles when a particle interacts with its antiparticle. The process results in the creation of new particles, and during this process, energy, momentum, electric charges and other quantum numbers of the system must be conserved. It has to be clear that we do not have yet a satisfying theory that models correctly all the type of channels and multiplicities of hadron annihilations and that we can consider as a final explanation of the annihilation process.

Nevertheless a lot of theoretical efforts have been made during the years and a quick survey of the available models can be made. In order to delve into the models and phenomenology of this process, it is important to make some distinctions. An annihilation process can occur either in flight or at rest, and the particles involved can be either fundamental particles (such as a positron and electron) or composite particles (such as a proton and antiproton).

Let us, for example, consider the annihilation of two fundamental particles, such as in an electron-positron annihilation. If this process occurs at rest the total mass of the particles is converted into two photons, each with an energy of $511\,\mathrm{keV}$, emitted in opposite directions. Any other outcome of this scenario would violate energy-momentum conservation. However, if the same annihilation occurs in collisions with sufficient energy, other heavier particles may be produced, such as W^+W^- pairs, $\mu^-\mu^+$ pairs, neutrinos, and D-mesons [47]. These processes are well-known and have been extensively studied.

In the case of annihilation processes involving composite particles such as nucleons (protons and neutrons), here shorted as N, the mechanisms are still actively being studied, and the rates of the different decay channels are not yet known. In this case, the elementary particles are the quarks that make up the nucleons, and the annihilation process occurs at this level. However, when the annihilation occurs, not all quark-antiquark pairs necessarily annihilate. The complexity of this process is confirmed by the observation of neutron-antiproton and proton-antineutron annihilations [48, 49], in which one of the quarks composing the nucleon has no corresponding antiquark in the antinucleon. At this level the strong interaction is the force which brings the leading contribution. The interaction between quarks is mediated by gluons as force carriers. As in the electron-positron annihilation, in quark annihilation, the total energy of the annihilation is released in the form of gauge bosons, including gluons in addition to photons, which can then give rise to other particles. Quantum Chromodynamics, which is the main theory describing this interaction, cannot be used at the energies at which annihilation at rest occurs. Several models are used instead for describing this process. We will illustrate them in the next sections. It has to be noted that none of these models, however, can be considered as a complete theory that describes the whole process.

Similarly to fundamental particle annihilation, annihilation processes involving composite particles can also occur at rest or in flight. In the latter case, not only inelastic processes such as annihilation ($\bar{N}N \rightarrow$ mesons and hyperons) and charge-exchange ($p\bar{p} \rightarrow \bar{n}n$), but also elastic reactions ($\bar{N}N \rightarrow \bar{N}N$) can take place [50]. It is important to distinguish between the high and low energy regimes, as different reaction channels can occur depending on the energy of the interacting nucleon and anti-nucleon. At high energies, multi-particle production dominates the total cross section, providing insight into the physics of hadronization. At low momentum (below $100\ \frac{\mathrm{MeV}}{\mathrm{c}}$), which is the energy regime of interest for ASACUSA and all the experiments in AD, the annihilation cross section is very large and dominates over the elastic cross section. Since there is no energy threshold, the annihilation process with production of mesons is the most significant at low energies. The theory in this energy regime combines both long-range and short-range physics, where direct interactions between quarks and anti-quarks occur. In general, $\bar{N}N$ annihilation at low energies can be described as a process generating a hot, concentrated quark gas.

Finally, there is also the process of annihilation of $\bar{N}Nu$, where Nu stands for Nucleus. Here, the antinucleon interacts with one or even multiple nucleons that compose the nucleus of the atom. The theory behind this process is discussed in section 2.3.3. This is the most complicated process to model, as it involves several steps besides annihilation.

2.3.2 Annihilation of $\bar{p}$ and $\bar{n}$ on p and n

There are two main ways of describing the hadronic annihilation process: one uses baryons and mesons as degrees of freedom (*baryon exchange model* [51]) and a second that is based on quark models (*quark rearrangement model* [52]).

The *baryon exchange model* explains the annihilation of $N\bar{N}$ particles in a way that is similar to the annihilation of e^+ and e^- particles through electron-positron interactions. According to this model, the $N\bar{N}$ annihilation is a brief interaction governed by baryon exchange that occurs at a distance of approximately 0.1 fm, which is equivalent to $\frac{\hbar}{2m_pc}$, where m_p is the mass of a proton. This model is based on the principles of hadronic behavior and incorporates the same meson-baryon connections found in nucleon-nucleon interactions [53, 54]. The connections are determined by Lagrangians that describe the fundamental dynamics of baryon exchange models. However, because the distance involved is small (0.1 fm), significant form factors must be added to the model to account for the dimensions of the intermediate off-shell mesons and baryons involved in the annihilation process [55]. The latest advancements in the baryon exchange model encompass the connections between the initial and final states of the annihilation [56, 57]. However, a major limitation of these models is that they only explain final states composed of two mesons and cannot depict all annihilation phenomena. Nevertheless, the baryon exchange model can provide accurate annihilation cross sections and a satisfactory explanation of nucleon-antinucleon scattering by introducing a supplementary, energy and state-independent phenomenological optical

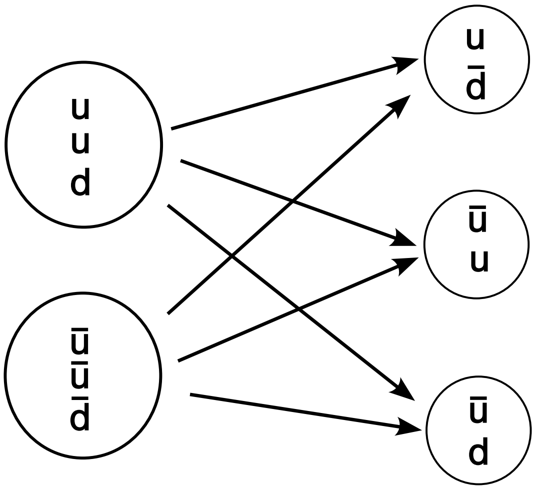

Figure 2.4: Scheme of a possible recombination of quarks in an annihilation event. The rearragement approach is used in the quark based model for the $N\bar{N}$ annihilation in order to predict the MIPs multiplicity of the annihilation.

potential [58].

In contrast to baryon exchange models, *quark models* focus on the constituent quark degrees of freedom, which provide an advantage as they inherently account for the spatial extension of hadrons. This leads to a reduced number of parameters, as no additional form factors or couplings are required. In the quark model, the mutual annihilation of $N\bar{N}$ does not necessarily mean the complete annihilation of all incoming quarks and anti-quarks, but involves various rearrangements into quark-antiquark ($q\bar{q}$) pairs and different mechanisms of annihilation. As a result, some of the incoming quarks and anti-quarks may annihilate, while new $q\bar{q}$ pairs may be created. In the quark rearrangement model [59, 52], the nucleon and anti-nucleon constituents (q and $\bar{q}$) re-couple to form a final state consisting of three mesons composed of π, ρ, ω, and η mesons. Therefore, the total number of quarks remains constant. The reaction can be represented by the equation:

$$qqq + \bar{q}\bar{q}\bar{q} \to q\bar{q} + q\bar{q} + q\bar{q}$$

A diagram illustrating one possible mode of quark rearrangement and their re-coupling into three pions is provided in Figure 2.4. Although this model has successfully explained the existing experimental data for pion multiplicity, it does not account for annihilation into two mesons or mesons other than those mentioned above. The two-meson channels are estimated to represent approximately 10% of the total annihilation events. The original quark rearrangement model was further developed to focus on three-meson decay models for $N\bar{N}$ annihilation at rest, taking into account existing experimental data. Part of the experimental data was used to adjust the parameters to obtain a quantitative fit to the data. The model was then tested by comparing the results with data that were not used in the fitting procedure, showing good agreement in decay rates for different channels between the data and the model [60]. The conclusion was that the quark rearrangement model with the spatial overlap function can provide a good description for approximately 90% of the branching ratios for $N\bar{N}$ annihilation at low energies [61].

In the case of low-energy proton-antiproton annihilation into two mesons, a non-relativistic quark model has been used, where at least one quark-antiquark pair annihilates to form two mesons in the final state [62]. For $p\bar{p}$ annihilation at rest into three mesons, both rearrangement and annihilation models provide similar reliability in explaining the branching ratios of the decay products. However, in the case of a decay into a two-meson final state, the annihilation model provides a better description and yields better agreement with the experiment [63].

Finally, there are also other approaches that can be used to describe $N\bar{N}$ annihilations. These alternative representations follow a phenomenological approach based on geometry and statistics. This is possible because empirical data indicate that some basic features of the annihilation are of a statistical nature. For instance, pion multiplicities are described by a statistical (Gaussian) distribution, while the momentum distribution of charged pions from $p\bar{p} \to \pi \pm X$ can be approximated by a Maxwell-Boltzmann distribution. One of the most successful statistical models is the two-meson doorway model [64]. It assumes that $N\bar{N}$ annihilation occurs through the formation of a two-meson intermediate state, which subsequently decays into the final state consisting of pions and/or kaons. This assumption is supported by the fact that a large, but quantitatively unknown, fraction of all annihilation channels proceed via two-meson intermediate states. This suggests that the energy density resulting from the annihilation process is preferably stored in a minimal number of massive meson resonances, rather than being transformed instantly into the kinetic energy of pions and kaons. The two-meson doorway model provides a better description of the $N\bar{N}$ annihilation in flight and can successfully reproduce many of its features for a wide range of antiproton momenta [55]. The model is also able to predict the rates for the decay channels obtained experimentally in the correct order of magnitude for annihilation at rest.

In conclusion, building a complete theoretical framework for $N\bar{N}$ annihilation at the quark level is challenging due to the complexity of the process, which is likely influenced by both quark dynamics and established hadronic interactions. Precisely determining the rates for all annihilation channels is extremely hard due to the potential interference between primarily formed mesons from $q\bar{q}$ pairs and the mesons resulting from final-state interactions.

2.3.3 Annihilation of $\bar{p}$ on Nucleus

The annihilation between $\bar{p}$ and a nucleus (Nu) can also be differentiated between annihilation in flight or at rest.

At energies of the order of several MeV, antiprotons passing through material lose energy according to the Bethe-Bloch formula (see section 4.1.1 for discussion on particle energy deposition). When they have lower energies, the Bethe-Bloch formula is not valid anymore and it is modified to take into account other effects. The particles lose energy until they are stopped into the material. At this point, they are captured into atomic orbits with a high principal quantum number n, forming a highly excited $\bar{p}$-atom system. The antiproton cascades downward, first by emitting Auger electrons and subsequently by emitting X-rays, reaching orbits that are closer to the nuclear surface. Here, in addition to the long-range Coulomb interaction, there are also short-range, strong nuclear forces that mediate the interaction, making absorption dominant. As a result, the antiproton interacts only with the nuclear surface, at a maximum depth where the density is 10% of the central nuclear density [65]. Annihilation on a nucleon is usually triggered when the quantum number n of the $\bar{p}$ is low enough, which depends on the charges of the nucleus.

For each annihilation between antiproton and a nucleon, there is a total energy of ≈ 1880 MeV available, which on average produces five pions. Different scenarios for the final state of the annihilation process are possible, including: only a portion of the produced pions escape without interacting with the nucleus of the atom, all the produced pions leave the nucleus of the atom via quasi-free scattering without interacting, or the pions go through charge exchange with other nucleons of the nucleus, resulting in a weakly excited compound nucleus. The rate of such channels depends strongly on the size of the nucleus of the atom. The energy of these pions (approximately 230 MeV) falls in the region of Δ resonances and they have a short range, which means that the energy transferred by these pions to the nucleus of the atom where the annihilation occured, is large. The interaction between the pions and the nucleus leads to an intranuclear cascade, during which the nucleus can be heated to very high temperatures (up to several hundred MeV [65]). Exotic states such as fireballs, special quark-gluon plasma, hot nuclear gas, and hyperons may be produced as a result of this interaction. [66].

The intranuclear cascade (INC) model [67] is a theoretical model used to describe the interactions between high energy particles and nuclei. It describes the cascade of particles produced in the interaction, including the production of secondary particles and fragmentation of the nucleus. The model has been successful in reproducing the momentum distribution of pions emerging from antiproton-nucleus annihilation, as mentioned in the previous statement.

In addition to pions and nucleons, the antiproton-nucleus annihilation can also produce other particles such as deuterons, tritons, and alpha particles. In some cases, the annihilation can even lead to the production of a Λ hyperon, which is a type of baryon containing a strange quark. These secondary reactions can occur between the residual nucleus and particles produced in the initial annihilation.

The residual nucleus after the annihilation has a nucleon deficiency and is, in most cases, radioactive. The decay mechanism of the residual nucleus is determined by the excitation energy deposited in it: if this energy is $\leq 2\,\mathrm{MeV/nucleon}$, the decay will most probably occur by successive nucleon evaporation and fission, which can, depending on the mass number, result in a wide spectrum of residual nuclei. If the excitation energy is close to the binding energy per nucleon ($\geq 5\,\mathrm{MeV}$), a phase transition of the nuclear matter into a liquid-gas type can occur, resulting in an explosive decay of the residual nucleus (multi-fragmentation) [68]. The outcome of such a process is the multiple production of nuclear fragments [69]. Both the evaporation and the multifragmentation processes are described by statistical models.

For the evaporation of moderately excited nuclei, the Weisskopf model is used to reproduce the emission of neutrons, protons, deuterons, tritons, ^{3}He and ^{4}He particles [70]. In the statistical model of the multi-fragmentation of hot nuclei, the excitation energy of the fragments is calculated based on the liquid-drop model description of the properties of hot fragments at finite temperatures. The lightest fragments such as deuterons, tritons, ^{3}He, and ^{4}He are assumed to be formed in their ground states [71, 72, 73]. The annihilation of antiprotons on heavy nuclei can result in the emission of a large number of nucleons from the parent nucleus. The energy spectra and multiplicities of the emitted particles provide insight into the intranuclear cascade process.

Non-conventional processes, such as annihilation involving more than one nucleon, can occur in the antiproton-nucleus reaction. The final states of these two-body annihilation channels, the so-called Pontecorvo reactions [74], are not attainable from annihilations with free nucleons. While in the ordinary annihilation of an antiproton with a nucleon at least two mesons are created, when the annihilation takes place in a nucleus, it is possible to create only one meson or possibly none at all. These kinds of events have been observed with a very small rate ($\approx 10^{-5}$) [75, 76]. The theoretical modeling of these processes is not straightforward, as the calculated probability of Pontecorvo reactions is found to be strongly dependent on the choice of wave functions. The rates predicted by the two-step model are two to three orders of magnitude smaller compared to the experimental data [77].

2.3.4 Existing measurement and phenomenology of annihilation processes

The scientific community has collected data from two sources over the years. The first source comprises early studies carried out by several experiments at LEAR (Low Energy Antiproton Ring), which was the antiproton decelerator built at CERN before the advent of AD. The second source includes experiments performed at the Brookhaven National Laboratory (BNL),

Number of pions	Combined percentage abudance
2	0.38± 0.03%
3	7.4± 0.03%
4	18.1± 1.8%
5	35.2± 3.7%
6	23.2± 2.8%
7	3.3± 0.03%

Table 2.1: Left column, number of pions per annihilation. Right column, Percentage of the yields of pions in an annihilation process at rest.

both of which were carried out more than thirty years ago. Both BNL and LEAR provided an antiproton beam of several hundreds MeV/c. In recent years, a few studies were performed within the AEgIS experiment in AD, where topology and energy deposition were studied with $3 - 100\,\text{keV}$ antiprotons. Other measurements in AEgIS [78] investigated the multiplicity of MIPs (Minimum Ionizing Particles) and HIPs (High Ionizing Particles) in aluminum, copper, silver, and gold [78, 79, 80].

Regarding pion yields, the mean multiplicities for charged and neutral pions per annihilation are: 3.05 ± 0.04 for charged pions and 1.93 ± 0.12 for neutral pions, resulting in a total of 4.98 ± 0.35 pions per annihilation. The multiplicity distribution of the total number of pions per annihilation follows a Gaussian distribution. The data from the Crystal Barrel experiment at LEAR were fitted with a Gaussian distribution, yielding a mean number of pions of 5.03 ± 0.05 and a width of 1.13 ± 0.07 [55]. The multiplicities of pions produced by annihilations are reported in Table 2.1, which includes all sources (BNL and LEAR experiments).

Regarding heavy ionizing particles, the measurements from LEAR and BNL detected only light prongs (charged particles), including helium ions, in a limited energy range and narrow solid angle [81, 82, 83]. The residual nuclei were investigated through measurements of their radioactivity after $\bar{p}$ irradiation, specifically their gamma spectra [84, 85, 86, 87, 88]. Although these experiments revealed significant features such as particle yields and momentum spectra of protons and other light particles with energies $> 50\,\text{MeV}$, the characteristics of $\bar{p}Nu$ annihilation at rest, such as hadronization and total product multiplicities, are still not well-described. The measurements and analysis performed in [78] yielded an average multiplicity for HIPs of 1.54 ± 0.07, 1.71 ± 0.07, and 1.60 ± 0.09 for copper, gold, and silver, respectively. These measurements showed that the model used in MC simulation softwares as Geant4 and FLUKA were not able to reproduce the results.

2.3.5 Why measuring products of $\bar{p}$ annihilations at rest

In conclusion of this section, I would like to draw some arguments that motivate the project to which I have contributed. Based on what has been discussed in the previous sections, three main themes emerge, which provide strong motivation for studying the annihilation products of low-energy antiprotons.

The fundamental process for slow-antimatter community
Several measurements have been performed on $N\bar{N}$ annihilations, however, the products of annihilation on a nucleus still remain poorly modeled. This issue has significant implications for the field of low-energy antimatter research, particularly in regards to the detection of antimatter signals. Hence, it is critical to enhance our understanding of this process and the resulting products, which depend on the used target.

The $\bar{p}Nu$ annihilation at rest is the main process of interest in the field of low-energy antimatter physics experiments, as it is crucial for the efficient detection and correct tagging of antihydrogen, regardless of the type of measurement the experiment aims to make. The annihilation of antiprotons on nuclei is the mechanism that produces the signal that has to be detected. Annihilation signals are also used for all types of calibrations, as most experiments in AD work with antiatoms, which require a lot of optimization work. These optimizations rely on the detection of annihilation products. Therefore, improving our understanding of the $\bar{p}Nu$ annihilation process and its products, may improve the optimization and calibration process used in the entire field of low-energy antimatter research.

Improving Monte Carlo simulation
Improving our understanding of annihilation products in different $\bar{p}Nu$ processes would not only benefit experiments aimed at detecting and studying antimatter systems, but would also have a significant impact on the accuracy of the Monte Carlo simulation software used in particle physics. At present, these software programs rely on models designed for processes occurring at higher energies, which were developed for hadronic interactions at high energy or for medical physics applications. However, the simulation of low-energy annihilation processes requires the extrapolation of these models to lower energies, which can be challenging due to the scarcity of data in this energy range. As a result, the accuracy of these simulations is limited, and experiments have shown that Monte Carlo software can provide different descriptions of annihilation products depending on the used physics model. By collecting more data on annihilation products in different $\bar{p}Nu$ processes, we can improve the accuracy of these simulations and better understand the behavior of low-energy annihilation products.

Improving the Monte Carlo simulation software not only would benefit the field of slow-antimatter physics in terms of a better understanding of the annihilation processes but also would have a significant impact on the development and optimization of detectors. The current high-energy detector technologies used in slow-antimatter physics experiments include microstrip modules, scintillating bars and fibers, crystals, and multiwire proportional chambers. The optimization of these detectors for small experimental volumes, high acceptances, and accuracy requires reliable Monte Carlo simulations, which are mainly performed using the physics models included in Geant4 and FLUKA. With better simulations, the accuracy of reconstruction algorithms, signal over background selection algorithms, and any other type of data analysis can be improved, as well as machine learning algorithms that greatly rely on simulations for training. Additionally, improved Monte Carlo simulations can aid in the development and design of entirely new experiments and measurements by providing guidelines for the desired signal and optimizing the detector geometry and materials. Therefore, the impact of improving Monte Carlo simulations extends far beyond understanding the annihilation process and has several benefits for the entire field of slow-antimatter physics.

Insight on the Pontecorvo effects and on nucleus surface structure

Another reason to continue studying antiproton annihilation at rest is the study of three-body Pontecorvo processes. The Pontecorvo process refers to antiproton annihilations on nuclei in which the final states cannot be obtained from annihilations on free nucleons. These rare channels have been studied by several collaborations during the LEAR era, and two-body final states such as $\bar{p}p \to K_0 \bar{K_0}$ have been measured, although the rates are very small, ranging from 10^{-6} to 10^{-5} [89, 90, 76]. Several models have been proposed to describe these processes, but in order to discriminate between them, measurements of even three-body Pontecorvo processes are needed. One promising approach is the fireball model [91], in which the highly excited multiquark bag decays into the observed final state through quark annihilation or rearrangement. The predicted formation probability of the fireball is around 3% [92], and this model can be tested by studying annihilation on three nucleons, such as $\bar{p}$ annihilation on ^{3}He, resulting in colinear proton and neutron (^{3}He$\bar{p} \to np$), for which no data currently exist. Finally annihilations of $\bar{p}$ on nuclei at rest can give insight on the surface structure of the nuclei. In nuclei neutrons tend to be at the surface of the nucleus, but there is not yet a clear understanding of the theory which describes their configurations. Since, if the annihilation is at rest, the antiprotons annihilate at the surface of the nuclei, studying this type of annihilation process can give information about the surface structure of the nuclei.

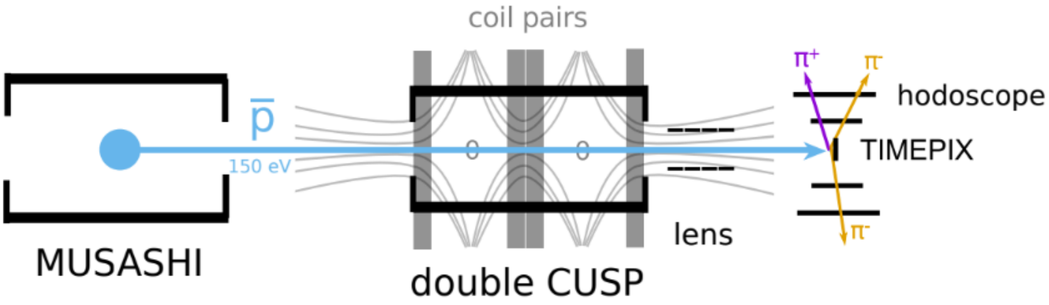

Figure 2.5: Sketch of the experimental set-up used for the measurement of products of antiproton annihilation at rest. The antiproton path is showed in blue. The main line has been modified so that the antiprotons, after the CUSP, pass through the Einzen lenses used for focusing the beam and then they directly impinge on the target used for the measurement. The spectroscopy part of the line has been removed entirely.

2.4 The slow antiproton annihilation experiment

As we saw, the annihilation process involving $\bar{p}$ and $\bar{n}$ on nucleons is not well characterization and on the same time it is of great interest for the entire slow energy antimatter community. Here I will summarize the slow antiproton beam project, mentioning both the part where I was involved and its updated status. The details on my contribution can be found in chapter 4.

The project comprises a first phase that involves a systematic study of the multiplicity and energy distributions of MIPs and Heavily Ionizing Particles (HIPs) in proton-nucleus annihilations using the current apparatus. This initial phase of the project will provide information for tuning the Monte Carlo simulation software: Geant4 and FLUKA in the low-energy region (< 1 keV).

The measurement was carried out in collaboration with NIKHEF (M. van Beuzekom and J. Visser), who provided the Timepix3 detector, described in section 3.6. For this measurement, the line dedicated to ASACUSA antiprotons was slightly modified; a sketch of the main part of the used line can be seen in figure 2.5. The main modification was the removal of the part devoted to spectroscopy (shown in section 3.5), which was unnecessary for the measurement. Additionally, the detector setup was modified, and a more detailed description of this modification is given in section 4.2.1.

Regarding the measurement procedure, a single AD shot was first trapped and cooled in the MUSASHI trap before being extracted slowly[2] with 150 eV of kinetic energy [93]. The antiprotons were then transferred through the double-CUSP trap whose MRE were powered

---

[2] *Slowly* in this case means that the antiprotons were released from MUSASHI over a time period of seconds.

off. The magnetic field of the pair of anti-Helmholtz coils guided the antiprotons towards the exit and the detector. Different targets were placed at the exit where the antiproton annihilated, and the products were detected by the hodoscope and the Timepix3, which replaced the BGO for this measurement.

MC simulations were developed for this work using the Geant4 software to simulate both the hodoscope signal and the Timepix3 signal. For these simulations, two different models were used: CHIPS [94, 95] and Fritiof (FTF) [96, 97, 98]. In order to complete the first part of the project, FLUKA simulations had to be developed. FLUKA uses a different model named PEANUT [99]. Additionally, both FLUKA and Geant4 simulations had to be digitized to enable comparison with the real data. My contribution was to fulfill these two remaining steps.

The project is still ongoing. In this second phase ASACUSA is developing and commissioning a new line entirely devoted to the study of antiproton annihilations at rest. This parasitic line is intended to use the positron transfer line to deliver the antiprotons trapped in MUSASHI to a new detector consisting of a series of Timepix4 (a new and improved version of Timepix3) positioned at the corner where the transfer line meets the STACKER. The new detector will have an acceptance close to 4π. In order to bring the antiprotons up to this new detector, a bender designed to be placed at the exit of MUSASHI. This new line will open up several possibilities regarding antiproton at rest annihilation measurements. More in-depth characterization on more materials will be possible. There are also plans to measure Pontecorvo reactions and even to observe quantum interferometry signals of antiprotons.

Chapter 3

ASACUSA-CUSP apparatus

This chapter aims to introduce the ASACUSA-CUSP experimental apparatus and differentiate it from other collaborations working in the low energy antimatter field. The subsequent two projects that will be presented in the following chapter share many similarities with ASACUSA-CUSP, with some minor differences that will be pointed out later on. The chapter begins with a focus on the AD, which serves as the source of antiprotons at CERN, before moving on to discuss the ASACUSA-CUSP beam line, where antiprotons and positrons are trapped and manipulated.

3.1 The $\bar{p}$ source and overview of the main line

The AD, or Antiproton Decelerator, is the starting point for all antimatter experiments at CERN, including ASACUSA. The AD is the only source in the world for slow antiprotons. To create antihydrogen, which is the only antiatom created nowadays, both positrons and antiprotons at very low kinetic energies (in the eV range) are needed. Positrons can be easily produced with a radioactive source, but antiprotons are much harder to come by. The AD delivers antiprotons through a series of accelerating and decelerating steps. An overview of the accelerator complex used to produce low-energy antiprotons can be seen in Figure 3.1.

The process for creating antiprotons at low energy is as follows: a bunched proton beam is generated using a linear accelerator (LINAC 2). The protons are then accelerated to an energy of $1.4\,\text{GeV}$ by the Proton Synchrotron Booster (PSB) and further accelerated to a kinetic energy of $25\,\text{GeV}$ by the Proton Synchrotron (PS). The PS also serves as a pre-accelerator for the Super Proton Synchrotron (SPS) and ultimately for the Large Hadron Collider (LHC). Subsequently, the protons are directed towards an iridium target to produce antiprotons through the following reaction, with a kinetic energy of 2.7 GeV:

$$p_{beam} + p_{target} \rightarrow p + p + p + \bar{p} \tag{3.1}$$

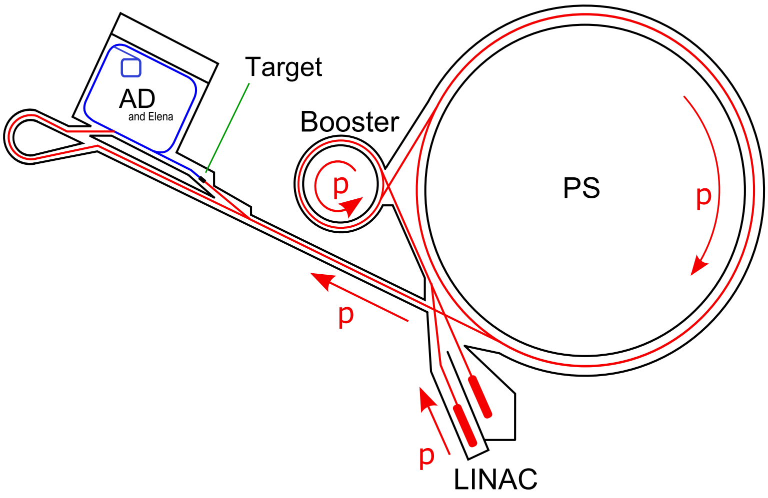

Figure 3.1: Schematic of the proton acceleration pathway for the creation of antiprotons through the various acceleration stages. Lines in red show protons, and lines in blue show antiprotons.

The energy of the antiprotons produced is too high to be trapped in an electromagnetic trap. Therefore, the antiprotons must be slowed down to the chemical energy scale, which

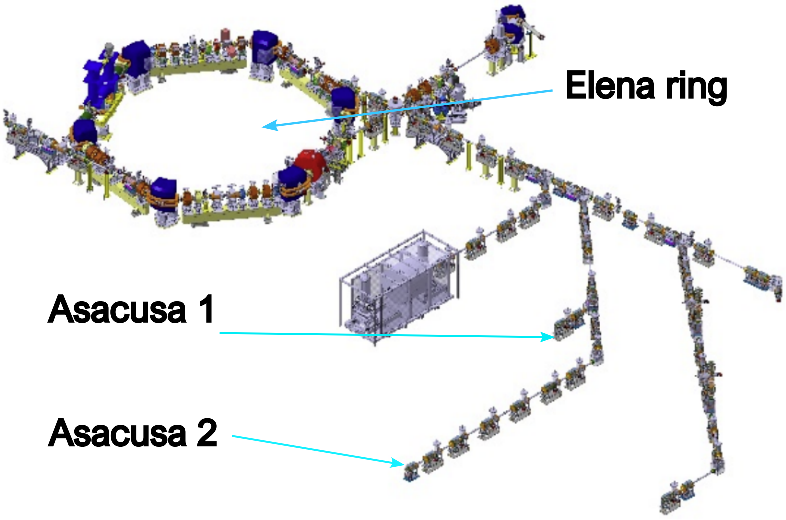

Figure 3.2: Graphic rendering of the ELENA ring. The two lines dedicated to ASACUSA, ASACUSA 1 and ASACUSA 2, are indicated. ASACUSA 1 is the line dedicated to antiprotonic helium, whereas ASACUSA 2 is the one dedicated to ASACUSA-CUSP experiments.

is accomplished using decelerators. The antiprotons are first injected into the Antiproton Decelerator (AD), where they undergo a series of deceleration and cooling steps. Deceleration causes an increase in energy and position spread of the particles in the beam, which is countered by stochastic and electron cooling [100]. At the end of each cycle (approximately every $110\,\mathrm{s}$), a bunch of $\approx 3 \cdot 10^7$ antiprotons with a duration of $\approx 150\,\mathrm{ns}$ and a kinetic energy of $5.3\,\mathrm{MeV}$ is ejected into a second decelerator called ELENA (Extra Low Energy Antiproton). ELENA further decelerates the antiprotons from the AD down to $0.1\,\mathrm{MeV}$, with a cycle duration of $20\,\mathrm{s}$ and a repetition rate limited by the AD to $\approx 100\,\mathrm{s}$. After this second deceleration step, the particles are injected into the individual experimental areas. Figure 3.1 provides an overview of the accelerators and decelerators mentioned above. Additionally, Figure 3.2 depicts an overview of the ELENA ring, with lines going to the two experiments of ASACUSA.

The ASACUSA line begins with a splitting section that provides antiprotons to both the section of the experiment dedicated to the study of antiprotonic helium and the section dedicated to antihydrogen spectroscopy. In the following section, I will focus on the latter. The experiment can be divided into four main parts: an antiproton line, a positron and transfer line, the beam production region and the spectroscopy-dedicated section. It should be noted that this is simply a classification I am using to present the experiment in a more organized manner, and it is not a rigorous definition. As we will see, the configuration of the experiment can change depending on the measurement to be done. Figure 3.3 provides a full view of the antihydrogen spectroscopy experiment with the four sections highlighted.

3.2 Positron line

The positron line of ASACUSA is the line dedicated to the accumulation and delivery of positrons to the rest of the experiment. From 2021 the positron line is composed by four main parts:

- The ^{22}Na radioactive source
- The positron trap, called FPS since it has been produced by the company First Point Scientific.
- The STACKER trap
- The transfer line

The transfer line consists of a series of water-cooled solenoid magnets that guide the positrons to the CUSP mixing trap. A photo of the entire line can be seen in Figure 3.4.

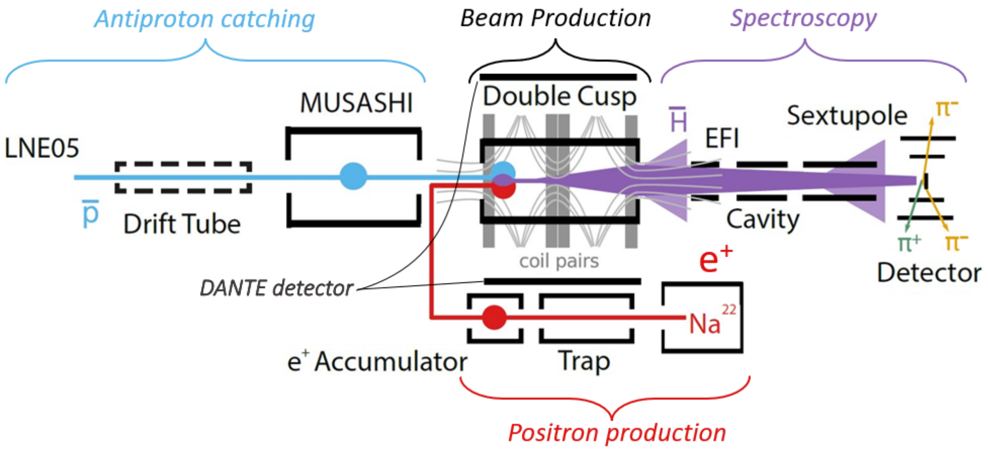

Figure 3.3: Schematic diagram of the experimental apparatus of the ASACUSA-CUSP experiment. In blue the antiprotons delivered by ELENA are shown, in red the positrons produced by the ^{22}Na source and in purple the antihydrogen beam produced in the CUSP trap. The beam polarization phases are indicated with purple triangles to indicate the defocusing of antiatoms in HF states.

The FPS and its accompanying source replaced the previous positron trap and source, and the STACKER was designed and installed this year. The positrons needed for antihydrogen synthesis are provided by a ^{22}Na source which produce them via β^+ decay with an energy spectrum picked approximately at 540 keV. This energy is too high to use the positrons as is, so a moderator consisting of a layer of neon ice on a cone structure located in front of the source is used to slow them down. Approximately 1% of the positrons that enter the iced neon are moderated and form the slow beam, with an peak performance of 10 millions per second and a 2 eV energy spread.

The slow beam then passes through an blocker, which is necessary to eliminate the direct line of sight between the source and the first trap. This process selects only low-energy positrons by using magnets that can guide them through the hole while stopping high-energy positrons from the moderator. This blocker is also needed to exclude the 1.2 MeV gammas produced by the second decay of the ^{22}Na. The selected positrons then enter the trapping region, which, in this case, is a Penning-Malmberg trap [101]. The majority of electromagnetic traps used for slow antimatter physics are Penning-Malmberg traps, and these devices exhibit cylindrical symmetry. They comprise a coil that generates a constant magnetic field parallel to the axis of the trap, and a series of cylindrical rings that function as electrodes to produce an electrostatic field. The magnetic field confines particles in the radial direction, while the electrostatic field confines them longitudinally. In this specific case,

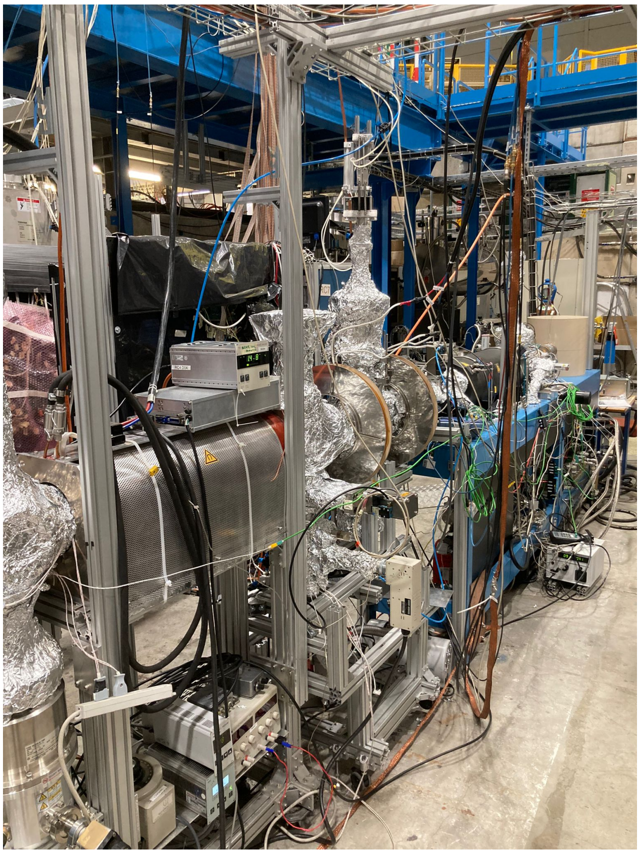

Figure 3.4: Photo of the positron apparatus. Shown from left to right are the STACKER, the FPS trap and the ^{22}Na source.

the magnetic field strength is approximately 500 G. Roughly 30% of the positrons that enter the trap electrodes are confined, while the rest are lost due to the formation of positronium, an exotic antiatom created by a bound state between a positron and an electron. Specifically, this is a buffer gas trap (BGT), which consists of electrodes with different radii where a gas, usually N2, is injected. This results in different gas pressures, the pressure is higher in the early stages and lower in the later stages: from $\approx 10^{-4}$mbar in the first electrode that is 25 cm long and with a inner radius of 10 mm, the pressure passes to $\approx 10^{-6}$mbar in the second electrode, which is ≈ 18 cm and with a radius of ≈ 25 mm, to finally reach $\approx 10^{-8}$mbar in the trapping electrodes, which are 5 cm long and with a radius of 25 mm. The purpose of the gas is to decelerate positrons through inelastic scattering. With this configuration the positrons in the FPS trap have an average lifetime of around 2 s, during which roughly a million positrons can accumulate[1]. Having this short lifetime and also being a small trap[2] filled (10^{-4}mb, ar) with N2 and SF6 gases cause also some drawbacks. Transferring directly to the CUSP would indeed significantly harm the vacuum in this condition.

Hence, the STACKER, another Penning-Malmberg trap, has been added to serve as a new positron accumulation stage between the positron trap and the transfer line. The new accumulator has been installed within an existing water-cooled solenoid magnet, which forms the first part of the transfer line, providing a field of up to 800 G with a central uniform region ($\Delta B_z/B_z \approx 2.5\%$) of approximately 320 mm. The trap is designed to be flexible, allowing for new pulses to be caught while stacked positrons remain under compression, and to enable the bunching of particles before the transfer to the CUSP trap for improved catching efficiency. This stage is designed to store up to 100 million positrons in a single pulse, ready for transfer to the CUSP trap when needed for mixing.

Besides improving vacuum conditions in the CUSP trap due to fewer transfers, another major advantage of this additional accumulation stage is that it can be continuously filled with positrons, which are ready for transfer to the CUSP trap for mixing experiments. Consequently, there is no longer a need to stack positrons in the CUSP trap.

3.3 Antiproton line

What I refer to as the antiproton section of the experiment is the area where antiprotons travel or are trapped. Two primary components of this section are worth highlighting:

1. The drift tube [102].
2. The MUSASHI trap [93].

The drift tube has the goal of tuning the beam coming from ELENA to achieve an optimal functioning of the MUSASHI trap. Prior to the introduction of ELENA , antiprotons were provided with an energy of 5.3 MeV for each experiment. They were decelerated with a radio frequency quadrupole decelerator (RFQD) and two $90\,\mu$gcm^{-2} biaxially-oriented polyethylene terephthalate (BoPET) degrader foils. These foils were covered with printed thin strips of Ag (20 nm thickness), which allowed for beam diagnostics. In particular, they were essential for steering and optimizing the injection in MUSASHI. Since 2021, antiprotons arrive from ELENA with an energy of 100 keV, and it is no longer necessary to slow them down. However, to enable beam diagnostics and its control, a drift tube has been developed and inserted between the LNE05 transfer line and MUSASHI. This tube accelerates antiprotons to 120 keV and is compatible with the existing BoPET foil beam profile monitor.

---

[1] This is a couple of order of magnitude more positron accumulated than the positrons accumulated in the same time by the trap previously used in ASACUSA

[2] In comparison with other type of trap such as the one previously used by ASACUSA.

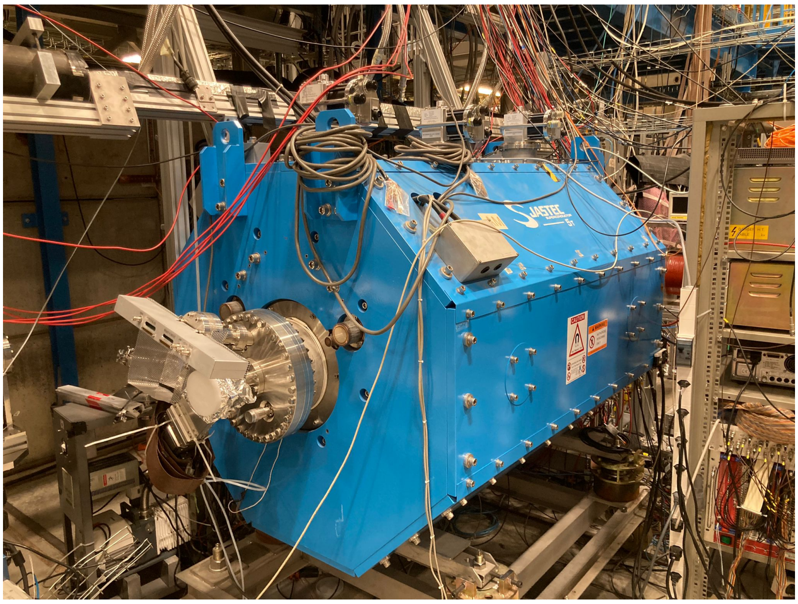

Figure 3.5: Photo of the MUSASHI trap. In this photo the trap is disconnected from the main line, in the foreground you can see the trap entrance to which the drift-tube was then connected.

Once the antiprotons pass through the drift tube, they are captured, cooled, and compressed in the so-called MUSASHI trap. Figure 3.5 shows a picture of MUSASHI, which is also a Penning-Malmberg trap. Unlike the FPS trap, it has a multi-ring electrode (MRE) configuration consisting of a series of radially equal short electrodes stacked for better manipulation of the plasma. Typically, a few AD shots are stacked in the MUSASHI trap before being transported to the mixing trap for antihydrogen synthesis, accumulating about $3 \cdot 10^6$ antiprotons. They are cooled by pre-loaded electrons, which are lighter enough to self-cool via synchrotron radiation[3]. Afterwards, the electrons are kicked out by lifting the trapping potential for a few hundred nanoseconds, which is short enough to not affect the antiproton cloud. The antiprotons are then radially compressed via the rotating wall technique [103] and finally extracted by dedicated electrodes.

The MUSASHI trap can operate in two extraction modes:

- the pulsed extraction mode is used to produce short-bunched beams, which are preferred for subsequent trapping in the mixing trap.
- the slow extraction mode is used for antihydrogen formation runs and studies of antiproton annihilation.

---

[3] The power emitted by synchroton radiation is proportional to B^2 and goes as $\frac{1}{m^4}$, where m is the mass of the charged particle in the B field.

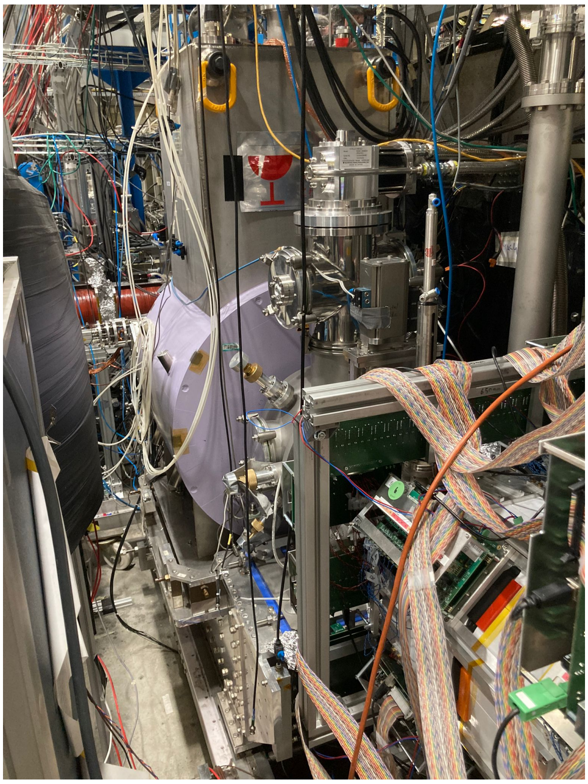

Figure 3.6: Photo of the CUSP trap (center, in pink). The structure above the CUSP trap is the compressor needed to cool the magnet, around the trap one can glimpse the already installed DANTE panels and in the foreground the hodoscope.

In both modes, antiprotons are released from the trap by ramping up the confining potential well until they spill over the potential barrier. The kinetic energy of $\bar{p}$ is determined by the potential difference between the potential barrier and the ground[4]. For testing the DANTE detector reconstruction software discussed in 5, the $\bar{p}$ were extracted with a kinetic energy of 15 eV. After extraction, the $\bar{p}$ are adiabatically transported using pulsed transport coils over a distance of approximately 2.5 m along the beamline [104] to the mixing trap.

3.4 The beam production region

The mixing trap used in the ASACUSA experiment, also known as the double-CUSP trap or simply the CUSP trap [105], is a critical component of the experiment. It is used for both the creation and polarization of antihydrogen, as well as the cooling and trapping of antiprotons

---

[4] A termal equilibrium is reached before the temperature measurement is made with this procedure, in contrast with other type of measurement such as ballistic method.

if antihydrogen is produced, or for directing antiprotons towards thin target layers. This trap

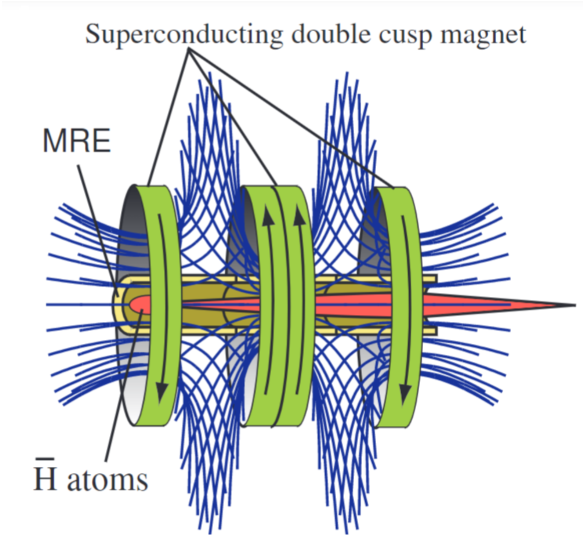

Figure 3.7: Scheme of the coils configuration of the CUSP trap and the magnetic field resulting from the currents flow configuration.

differs in configuration from the other electromagnetic traps used in the experiment, as it does not have the usual PMtrap configuration. Instead, it uses a MRE configuration for the electrostatic potential for axial confinement, and a superconducting pair of anti-Helmholtz coils for radial confinement. This configuration results in the magnetic field having two points of zero field and diverging field lines, which gives rise to its name, see figure 3.7 for a scheme of the magnetic field. The current flow of the two central coils is oriented parallel, while the current of the side coils is anti-parallel to the central ones. This choice allows for the polarization of the beam, since a force is applied to the produced antihydrogen due to the magnetic field gradient. A photograph of the CUSP trap is shown in Figure 3.6. The relevant processes for antihydrogen creation in ASACUSA are radiative recombination and three-body recombination [106], with the latter being dominant [107]. Due to energy and momentum conservation, a third body is required for the formation of a bound state of antiproton and positron. In the case of three-body recombination, a second positron assumes this role, as shown below:

$$\bar{p} + e^{+} + e^{+} \rightarrow \bar{H} + e^{+}$$

Additional information regarding the processes involved in antihydrogen production can be found in [108, 109]. A typical electric potential configuration for the antihydrogen synthesis, used in the last beam time, is illustrated in the center of Figure 3.8. The beam production region has a nested well shape for the confinement and manipulation of both the

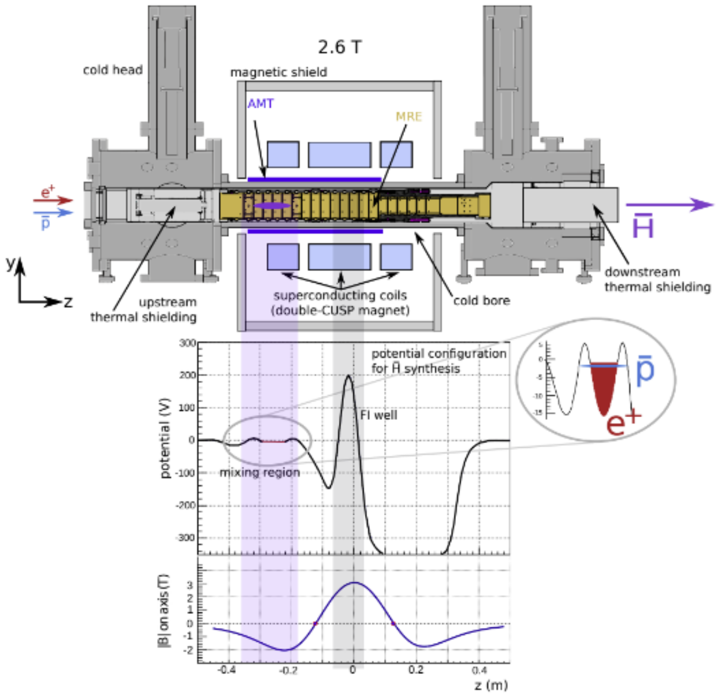

Figure 3.8: On the top, scheme of the CUSP trap geometry. In yellow the MRE trap. In purple the AMT. In light blue the supercoducting magnet. The mixing stage happens in the left part of the MRE (indicated by light purple). At the end of the MRE there are electrodes used as an internal field ionizer (indicated by light black). Bottom, a scheme of the potential confinement at the center of the trap used for trapping and ionizing the $\bar{H}$. and the profile of the B field on axis. Image from [21].

constituents, and a close-up of it is shown to the right of the plot [110].

3.5 Spectroscopy line

This portion of the beamline is dedicated to the manipulation of the antihydrogen hyperfine splitting (see Section 2.1.2). Downstream of the antihydrogen production region, the spectrometer beamline includes:

- a field ionizer
- a spin-flip inducing microwave cavity
- a spin state selecting superconducting sextupole magnet.

A photos of the three components can be seen in Figure 3.9. The field ionizer is positioned immediately downstream of the CUSP trap exit and its purpose is to determine the principal quantum number, n, of the exiting antihydrogen atoms. Based on the strength of the electric field, atoms with $n > n_{min}$ will undergo ionization, and the resulting antiprotons will be deflected. The electric field required to dissociate an atom with a principal quantum number n is given by [111, 112]:

$$|\vec{E}| = \frac{1}{16}n^4$$

The field ionizer consists of two parallel copper mesh electrodes arranged perpendicular to the beam direction with a distance of 1 cm between them. The meshes have high permeability, allowing the majority of antihydrogens or antiprotons to pass through freely.

The system for spin-flip induction consists of two pairs of Helmholtz coils surrounding the microwave cavity. These provide a small, homogeneous magnetic field B_{hom} resulting in the Zeeman splitting of the atoms energy levels. The whole structure is encased in a 3 layers cylindrical shielding in order to achieve a high homogeneity of B_{hom}. The cavity has a large bandwidth of 12 MHz around the resonance frequency of 1420 Hz. [5]. The orientation of B_{hom} to B_{osc} can be changed by rotating the cavity with respect to the Helmholtz coils. This is necessary, since the magnetic fields need to be parallel to measure σ_1, and perpendicular to measure the π_1 transition.

The magnetic sextupole magnet is a device that applies a magnetic field gradient along the axis of the beam pipe. This gradient causes a focusing effect on the antihydrogen atoms, which have different hyperfine states. By adjusting the strength of the magnetic field gradient, it is possible to selectively focus or deflect antihydrogen atoms based on their hyperfine state. imilarly to the cavity, the sextupole magnet has a large opening diameter. The cryogenic cooling of the sextupole magnet is necessary to maintain the required magnetic field strength of 3.5 T and gradient.

3.6 Detectors

The ASACUSA experiment makes use of several detectors and diagnostic devices along the beamline. In this section, I will introduce the main ones: the hodoscope, the bismuth germanate (BGO), the ASACUSA Micromegas Tracker (AMT), the Timepix3, and the Detector for Annihilation Tracking Experiment (DANTE). Figures 3.10, 3.11, and 3.12 show pictures of the first three detectors, while pictures of the last two can be found in Chapters 4 and 5. Additionally, several diagnostics for plasma manipulation, such as multi-cathode plates, Faraday cups, and phosphor screens, are used daily, but I will omit their description here for brevity. The primary detector used for Several measurements in different projects of the ASACUSA collaboration is the hodoscope tracker, which is used in combination with other detectors for the tracking of annihilation products: for spectroscopy measurements,

---

[5] This ensures that the two transitions of interest, σ_1 and π_1, can be measured, see section 2.1.2

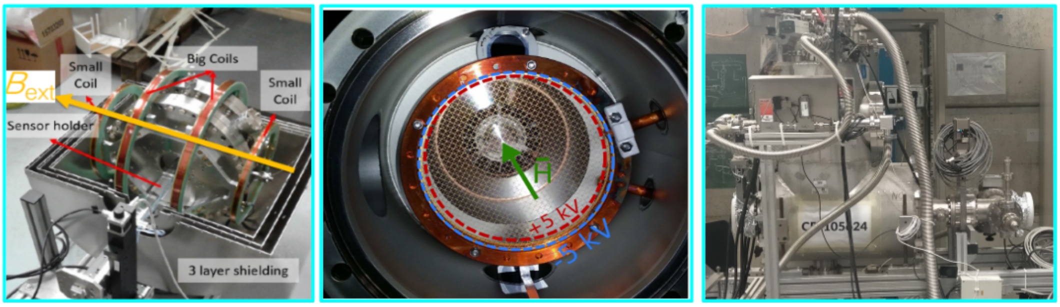

Figure 3.9: Photo of the three main components of the spectroscopy part of the line. On the left the microwave cavity, surrounded by the Helmotz coils and inside the three layers of the shields (half open in the photo). Center, the field ionizer at the exit of the CUSP. On the right the sextupole magnet disconnected from the line. The right side of the sextupole will be connected to the hodoscope, the left side to the cavity.

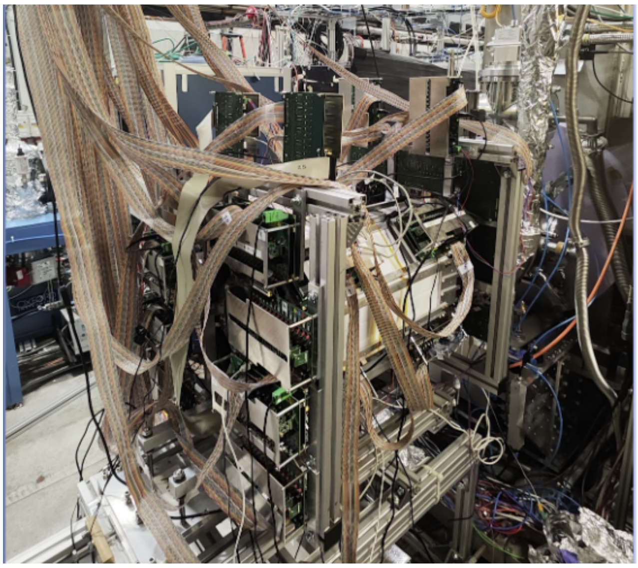

Figure 3.10: Photo of the hodoscope detector connected directly to the CUSP trap.

it was used in combination with a pixeled BGO detector. For slow antiproton annihilation measurements it was used in combination with four Timepix3 detectors.

The hodoscope [113] is a two-layered octagonal barrel-type detector consisting of 32 EJ 200 scintillator bars per layer. The outer bars have dimensions of $450 \times 35 \times 5\,\text{mm}^3$, while the inner bars are $300 \times 20 \times 5\,\text{mm}^3$. Trapezoidal prism-shaped light guides with lengths of $40\,\text{mm}$ (inner layer) and $75\,\text{mm}$ (outer layer) are attached to both ends of the bars, reducing their cross section to $8 \times 5\,\text{mm}^2$ to match the active area of the used silicon photomultipliers (SiPMss). The position resolution in the beam direction is provided by 240

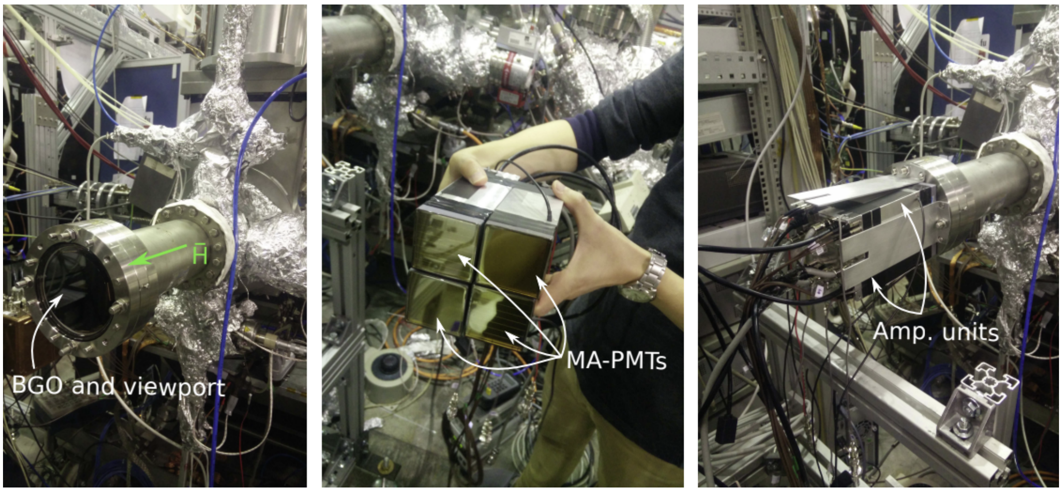

Figure 3.11: Photos of the BGO detector. On the left the BGO inside the pipe which is inserted in the Hodoscope detector. Center, the four Hamamatsu MA-PMTss for the readout of the emitted light by the BGO. Right the MA-PMTss unit mounted in the final configuration. Photos borrowed from [21]

EJ 200 scintillator tiles (15 per octagon side and layer). On the outer layer, $129 \times 30 \times 5\,\mathrm{mm}^3$ tiles have been placed perpendicularly onto each section of four bars. For the inner layer, the tiles have dimensions of $84 \times 20 \times 5\,\mathrm{mm}^3$. The bars are readout using two KETEK PM3350-TS SiPMss (3×3) on each end, whereas the tile readout is done with two serially connected Broadcom AFBR-S4N33C013 SiPMss (3×3) on one side.

The BGO scintillating crystal disc [114] is a detector used for the direct detection of annihilations. It is positioned at the center of the hodoscope and serves as a central calorimeter. The BGO crystal has a diameter of 90 mm and a thickness of 5 mm [115]. It is enclosed in a vacuum vessel maintained at ultra-high vacuum (UHV) pressure and secured with springs to the viewport at the end of the stainless steel CF-100 beampipe. When particles pass through the crystal and deposit energy, scintillation photons are generated and detected by four Hamamatsu H8500C multi-anode photomultipliers (MA-PMTss) mounted on the opposite side of the viewport. Each MA-PMTs has an effective area of $49 \times 49\,\mathrm{mm}^2$ and 8×8 channels (256 channels in total). Amplifier units (Clear Pulse CP80190) are connected and directly attached to the MA-PMTss.

The Timepix3 [116] is another detector used for the detection of annihilation products. It is a type of detector composed of a segmented silicon sensor and an ASIC readout system. The silicon sensor can have a thickness ranging from $675\,\mu$m to $300\,\mu$m and is bump bonded to the ASIC. The detector has a size of $1.4 \times 1.4\,\mathrm{cm}^2$ with 256×256 pixels and a pixel pitch of $55\,\mu$m. Each pixel is self-triggering and able to simultaneously measure the Time of Arrival (ToA) and the amount of charge collected in each electrode. To measure the ToA, the

Timepix readout system has a general clock running at 40 MHz. When a pixel is triggered, a faster clock of 640 MHz starts running until the next time stamp from the general clock. Combining these two internal clocks gives a time resolution of 1 ns to 2 ns. The dead time of the pixels is given as the Time over Threshold (ToT) pulse time plus 475 ns. The setup using Timepix3 instead of BGO for the measurement of the annihilation of resting antiprotons is presented in chapter 4.

The AMT [117] detector is positioned around the beam production region between the magnet and the cold bore of the trap. It comprises two layers of Micromegas and a layer of scintillators sandwiched between them for triggering. The AMT is designed to detect annihilations inside the trap and to reconstruct their vertices to distinguish between annihilations on the walls of the MRE (most likely by antihydrogen atoms) and annihilations of antiprotons in the rest of the trap [118]. However, the AMT will not be used in the current beam-time due to hardware issues that were discovered during the last accelerator long shutdown and have not yet been resolved.

Finally, another detector for tracking the annihilation products is DANTE (Detector for ANnhilations Tracking Experiment) [119]. The Brescia group designed and built a scintillating bar detector for monitoring the annihilation of particles along the apparatus. The main purpose of DANTE is to track the particles emitted by annihilations along the line to

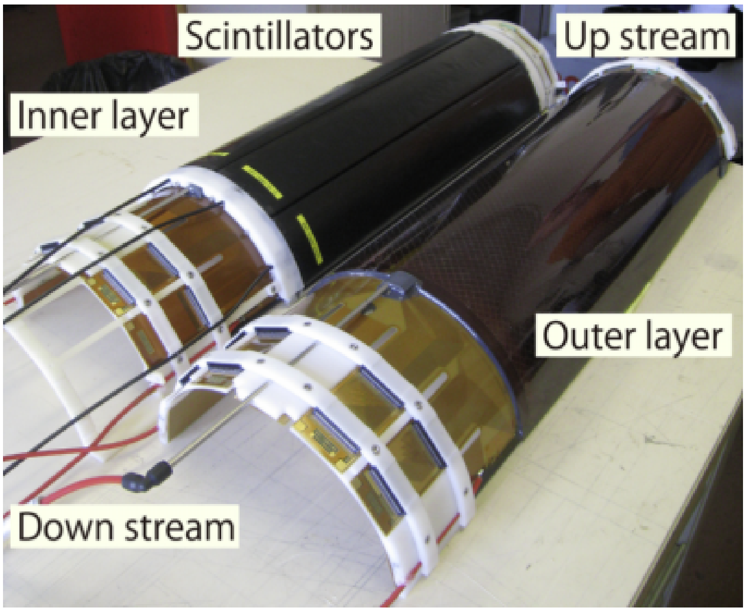

Figure 3.12: Photo of the AMT disassembled. The two half cylinders are the two layers of the AMT, when the AMT is installed they are sandwiched together. The AMT covers indeed only half the cylinder around the MRE in the CUSP trap.

monitor the plasma manipulation or transferring process. The installation took place in the summer of 2022, and the first tests were performed between October and November 2022. Below, we provide some details about the current detector hardware. A more complete description, including its previous uses and the upgrades made to the detector, can be found in chapter 5.

Figure 3.13: Photos of DANTE detector. Left, one of the 8 panel opened. In this photo the old configuration is shown, 30 bars trough WLS to an adaptor for the MA-PMTs. A photo of the new configuration is shown in chapter 5. Right, photo of two panels forming a module ready to be setup in the experimental area.

DANTE consists of eight panels, with each two panels aligned next to each other forming a module. Each panel is composed of a variable number of extruded scintillating bars, ranging from 54 to 60 bars, which were provided by FNAL. The scintillator part of the bar is made of Polystyrene Dow Styron $663W + 1\%, PPO + 0.03, POPOP$, and each bar is coated with a white Ti^2O layer. The left part of Figure 3.13 shows the composition of a single plane, and on the right an image of a complete module is presented. Each bar has a cross-section of 1.5×1.9 cm^2 and a length of 96 cm. A hole with a diameter of 2.5 mm has been grooved along the axis of each bar, which is used to host a Y-11 type wavelength-shifting (WLS) fiber with a diameter of 1 mm, provided by Kuraray and glued with E30 epoxy. The choice of WLS fibers was dictated by their absorption peak at 420 nm, which complements the 430 nm emission peak of the scintillator material used in the bars.

The front end of the detector has undergone a significant upgrade in the past two years, which will be discussed in more detail in Chapter 5. The main change has been the replacement of the device used to read the light from the WLS fibers. The signal is now read out using a series of SiPMss, one for each channel, whereas previously a 64-channel MA-PMTs

H7546-B by Hamamatsu was used. Figure 3.13 shows, on the left, a photo of an open panel with the readout configuration of the bars before the detector upgrade, and on the right, a photo of a completed module composed of two panels with perpendicular bars.

Chapter 4

Simulation and digitization of slow $\bar{p}$ annihilation products

In this chapter, I will present the simulation I developed as part of a project aimed at studying and characterizing antiproton annihilations on nuclei at rest. One of the primary goals of this project is to compare the results obtained from Geant4 and FLUKA simulations with data to evaluate the accuracy of the models used in these softwares. My primary contribution is the development of FLUKA simulations of the experiment and the digitization of both Geant4 and FLUKA simulations by means of another MC simulation software called $Allpix^2$. Additionally, I will address the effect of detector acceptance on real data to present an unfolded version of the data.

The chapter will begin with a review of the physics and principles of semiconductor detectors. This review is based on [120], where a more complete discussion of the theory can be found. Next, I will provide an overview of the experimental setup and previous work done on the project. Finally, I will present the simulation work and its results."

4.1 Semiconductor detectors

In particle physics several types of detectors are used to measure and record the properties of subatomic particles, such as their energy, momentum, charge, and position. In this section I will do a short digression about the physics and the operating principles of semiconductor detectors, which are devices that use a semiconducting material as the sensitive area to generate the signal due to the passage of a particle.

4.1.1 Particle energy loss in material

Different types of detection mechanisms correspond to different detectors. A semiconductor detector is characterized by having its sensitive parts, which are the parts of the detector where the signal is produced by the energy loss by a particle passing through, made of a semiconductor material. When charged particles cross matter, they interact with the atoms of the material, and there are mainly two processes involved: inelastic collisions with the atomic electrons (referred to as electronic) and elastic scattering from the nuclei (referred to as nuclear). Other processes with a much smaller rate can occur, but I will neglect them here for simplicity.

The transfer of energy from an incident particle to the target material is dominated by collisions with the atomic electron cloud. This is because the energy of the crossing particle is typically much smaller than the mass of the nuclei in most materials. The maximum kinetic energy that a particle of mass M can transfer to an electron is given by:

$$W_{max} = \frac{2m_e c^2 \beta^2 \gamma^2}{1 + 2\gamma m_e/M + (m_e/M)^2} \tag{4.1}$$

The primary quantity of interest in describing signal creation via ionization is the mean energy loss per length ($\frac{dE}{dx}$), which is given by the Bethe-Bloch formula:

$$-\frac{dE}{dx} = 2\pi N_A r_e^2 m_e c^2 \rho \frac{Z}{A}\frac{z^2}{\beta^2}\left[\ln\left(\frac{2m_e \gamma^2 v^2 W_{max}}{I^2}\right) - 2\beta^2 - \delta - 2\frac{C}{Z}\right] \tag{4.2}$$

Here, N_A is Avogadro's number, r_e is the classical atomic radius, m_e is the mass of an electron, $K = 4\pi N_A r_e^2 e m_e c^2$, Z is the atomic number of the absorber material, A is the atomic mass of the absorber material in g/mol, z is the charge of the incident particle, c is the speed of light in vacuum, v is the velocity of the impacting particle, $\beta = \frac{v}{c}$, $\gamma^2 = 1 - \frac{1}{\beta^2}$, W_{max} is the maximum energy transfer in a single collision as given by Equation 4.1, and δ is the density of the material. As seen from this equation, the energy loss varies with β, which is given by the velocity of the particle. The Bethe-Bloch formula is valid for velocities corresponding to $0.1 < \beta\gamma < 1000$. Several corrections have been made to the formula depending on the conditions of the incoming particle. The C factor has been added to account for the shell correction, which becomes important at low energies. The density correction term, δ, contributes to the polarization effect, as the electric field of the incoming particle can polarize the atoms along its path. For very low energies, higher-order corrections need to be included, such as the Bloch correction (proportional to Z^4) and the Barkas correction (proportional to Z^3).

Figure 4.1 shows the mass stopping power for a muon in copper. This quantity is defined as the stopping power (the negative of the energy loss per length) divided by the density of the material. The mass stopping power is large for low energies before reaching a minimum and then slowly increasing again. When a particle is in this minimum plateau, it is called a minimum ionizing particle (MIP). This minimum is found around $\beta\gamma = 3.0 - 3.5$, depending on the material. A pion is a MIP at around 350 MeV in silicon, while a proton is a MIP at around 2350 MeV. In addition to MIPs, we can also define highly ionizing particles (HIPs), which are particles that are heavier and slower than MIPs and release more energy into the material.

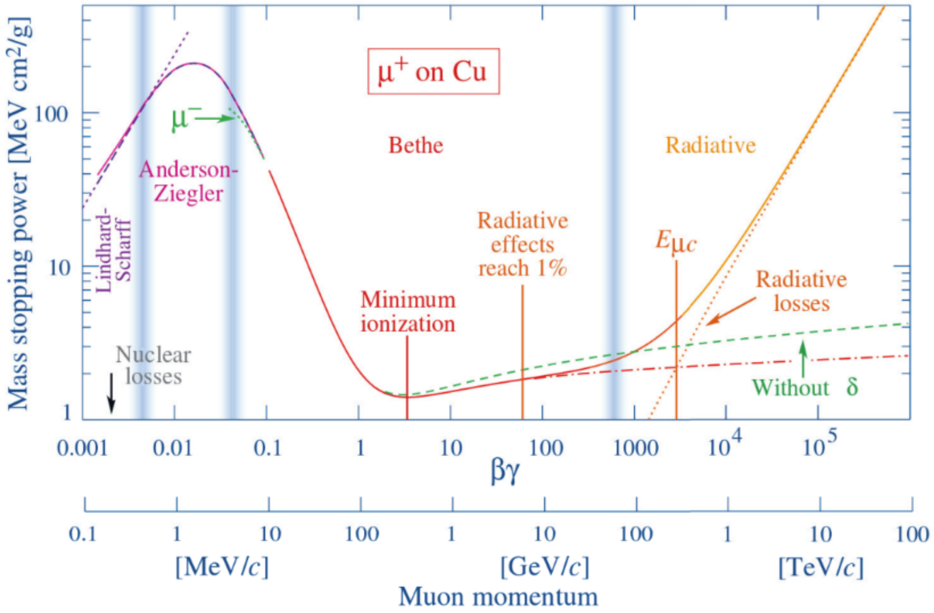

Figure 4.1: Mass stopping power ($\frac{dE}{dx}$) for positive muons in copper as a function of $\beta\gamma = \frac{p}{Mc}$ over nine orders of magnitude in momentum.

Energy loss is a stochastic process, and the Bethe-Bloch formula gives the mean energy loss. The variation around the mean is given by the Landau distribution. When a certain amount of energy is deposited via energy loss, a certain number of charge carriers are freed, depending on the material. In a semiconductor for instance, the charge carriers are electrons and holes[1]. These carriers will diffuse due to the random thermal motion in the material. After a time t_d, a point-like charge carrier concentration will be spread out as a Gaussian

---

[1] Holes are defined as an absence of an electron in an atom of the material, or otherwise in the *valence band*, that I will define in the next paragraph.

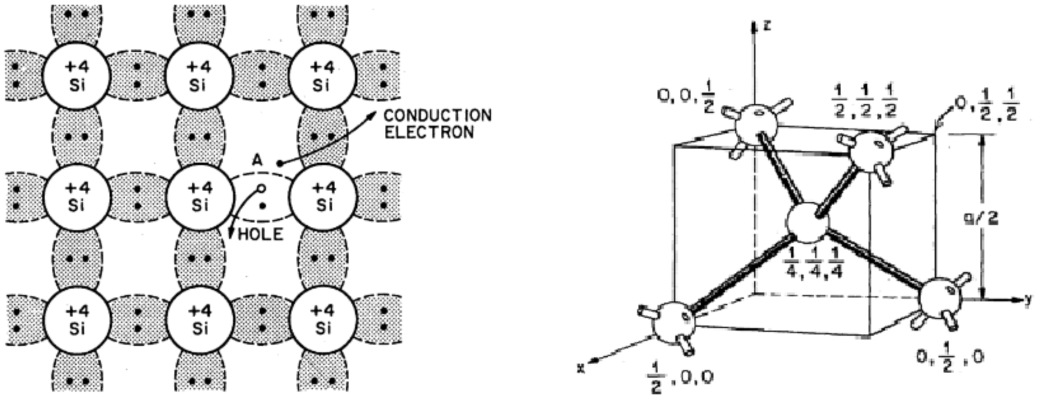

Figure 4.2: Crystalline structure of Silica. Left side, 2D representation, a creation of an electron-hole pair is represented. Right side, unit of the 3D structure of the crystalline lattice of Silica. The label for each atom indicates the 3D coordinates in unit of the lattice dimension g. Images from [120]

distribution with a standard deviation given by [121]:

$$\sigma = \sqrt{2Dt_d}$$

where D is the diffusion coefficient that depends on the material and the type of carrier (electrons or holes). For example, D for holes in silicon is $12\ \frac{\mathrm{cm}^2}{\mathrm{s}}$, while for electrons, it is $36\ \frac{\mathrm{cm}^2}{\mathrm{s}}$ at room temperature [122]

4.1.2 Semiconductor and the depletion region

Solid-state materials can have an amorphous or a crystalline structure. In the latter case, the material atoms are arranged in a three-dimensional periodic lattice. Figure 4.2 shows a three- and two-dimensional representation of the silicon lattice structure.

Materials can be classified into three main groups based on their conductivity, which is a fundamental property of the material defined as the reciprocal of electrical resistivity *i.e.* the property of the material that measures how strongly it resists electric current. Going from more conductive to less conductive materials one can define: conductors, semiconductors or insulators. In the case of solid-state materials with lattice structure, this classification can be explained using the theory of the *energy band structure.*

When two atoms are brought very close to each other, the superposition of the wave functions of the electrons in the atoms can create new energy levels that differ from the well-known bound states (s, p, etc.). When this superposition process is extended to consider all atoms in the large periodic lattice, the result is the creation of *energy bands.* The electronic

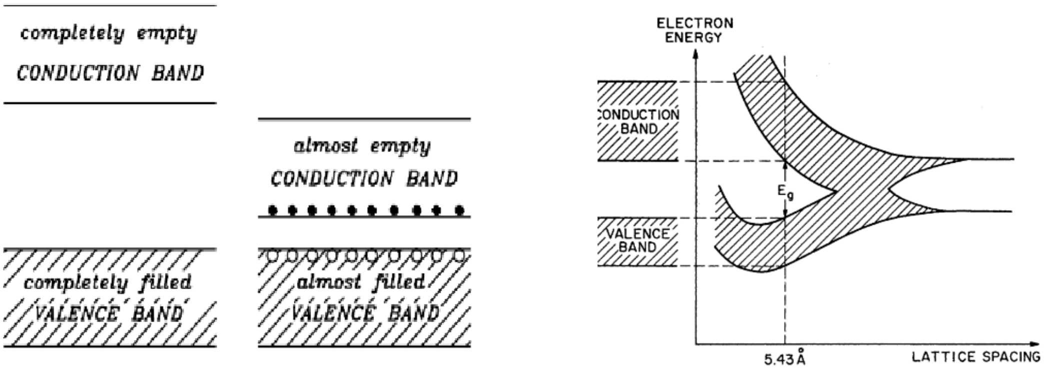

Figure 4.3: Representation of the conduction band structure. Left, difference between insulator (left) and semiconductor (right) with respect to the energy gap between the valence band and the conduction band. Right side, electron energy distribution depending on the lattice space.

occupancy distribution of these bands defines the material's conductivity.

We define a *conduction band* as a band that is either completely empty or only partially filled with electrons. In this energy band electrons are free and can contribute to current flow. Conversely, a *valence band* is a band that is completely filled with electrons. These electrons are responsible for forming the bonds between atoms in the lattice. Depending on the material, this two energy bands can be divided by a forbidden energy gap or potential barrier. This is a minimum energy that the electrons bounded to the atoms have to have in order to pass from the *valence band* to the *conduction band*. Figure 4.3 displays an example of a band structure and electron density distribution.

A conductor does not have a forbidden energy gap, allowing electrons to freely move into the conducting band. In contrast, an insulator has a large band gap, making it difficult for electrons to move to the conducting band. A semiconductor has a small band gap, which allows electrons to be thermally excited into the conducting band.
The probability of an allowed state i with energy ϵ_i being occupied is given by

$$n_i = \frac{1}{e^{(\epsilon_i - \mu)/k_b T} + 1}. \tag{4.3}$$

Here, T represents the absolute temperature in Kelvin, k_b is the Boltzmann constant, and μ is the Fermi level that defines the valence band. As temperature approaches the absolute zero, the occupancy n_i approaches a step function such that

$$\lim_{T \to 0} n_i = \begin{cases} 1, & \epsilon_i \leq \mu \\ 0, & \epsilon_i \geq \mu. \end{cases} \tag{4.4}$$

This demonstrates that a semiconductor behaves like an insulator at the absolute zero, and its conductivity increases increasing the temperature.

A detector that is based on semiconductor material takes advantage of the small energy gap between the valence and conduction band to create a zone that is sensitive to energy deposition from a particle passing through the material, as mentioned in the previous section. This sensitive area is also known as the depletion region. If we were to remove all electrons populating the conduction band, then no current would flow through the semiconductor. However, when a ionizing particle passes through the material, it can generate electron-hole pairs via a ionization process. If these pairs are energetic enough to traverse the forbidden energy gap, then they can create a current by populating the conduction band.

This process can be achieved by creating a *p-n junction*, which involves placing *p-doped* material (material with presence of negative ions) next to *n-doped* material (material with presence of positive ions). These materials contain impurities that give the former extra holes (compensated by the negative ions) in the valence band and the latter extra electrons (compensated by the positive ions) in the conducting band. In the p-n junction region, electrons and holes diffuse into the oppositely doped area and recombine, creating a non-conducting region around the physical contact of the two materials, without free carriers. This carriers displacement is given by two different effects which give rise to two currents: the *diffusion current* that is given by the carriers attracted from the opposite doped part of the material and the *drift current* that is given by the carriers be repulsed by the ions. When the two effects balance, the system is in thermal equilibrium and the ions in the region free of carries produce an electric field across the region, usually referred to as the built-in or equilibrium field. The field in the detector can be described by Gauss's law:

$$\vec{\nabla} \cdot \vec{E} = \frac{\rho}{\epsilon_0}, \tag{4.5}$$

where ρ is the charge density and ϵ_0 is the dielectric constant. This field keeps the depletion region free of charge carriers. Applying an external electric field in the same direction[2] as the built-in field will increase the width of the depletion region as more electrons and holes are removed. The voltage required to extend the depletion region across the entire detector is called the depletion voltage (V_d).

Known the depletion voltage, one can also model the time t_d defined in the previous paragraph. With the assumption that there are no interactions between the carriers, the time t_d can be written [123]:

$$t_d = \frac{\omega}{2\mu V_d} \ln \left(1 - \frac{2zV_d}{\omega(v + V_d)} \right)$$

---

[2] This is called the *forward bias*, a *reverse bias* where the depletion field has opposite direction with respect to the build in field is also possible.

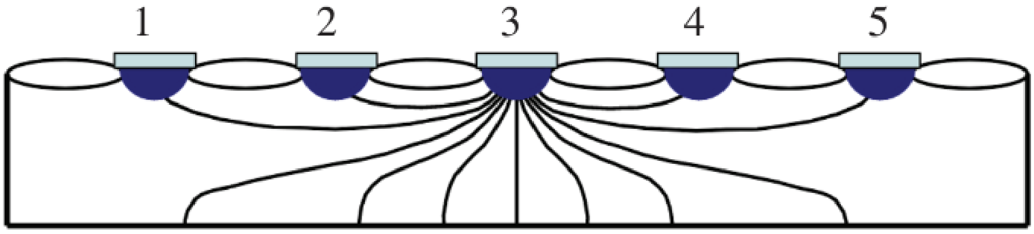

Figure 4.4: Illustration of the weighting electric field in a semiconductor pixel detector as seen as a slice trough the detector. Figure from [124].

Here, z is the depth of the energy deposition, w is the thickness of the detector, V_d is the depletion voltage, μ is the carrier mobility, and V is the applied voltage. This shows that a higher bias voltage on the detector leads to a shorter collection time, resulting in less diffusion and, subsequently, less charge sharing between pixels.

4.1.3 Collecting the charge

Once we have covered the basic concepts of particle energy loss in a material and also semiconductor principles, we need to discuss the process of collecting the charge carriers generated by the particle in the active area of the detector.

Since the Timepix3 is a pixel detector, let's focus on this typology. In this case, there is usually one electrode connected to each pixel. The electric signal in an electrode is caused by the induction current due to the movement of the carries and not the actual free charges reaching the electrode. The Ramo theorem [125] describes this behavior and states that the instantaneous current in an electrode i is given by

$$I_i = -q_p \vec{v}_p \cdot \vec{E}_{W_i} \tag{4.6}$$

where q_p is the charge moving in the detector, v_p is its velocity and E_{We} is the weighting field from electrode i. The weighting field for electrode i is defined as the field present if that electrode is at unit potential, while all other electrodes are at zero potential. Figure 4.4 shows the weighting field for electrode number 3.

The charge collected in an electrode is equal to the integrated current. As seen, the weighting field is stronger if closer to the electrode under consideration, hence the current flowing in an electrode is higher as the charge is collected in that electrode. However, the weighting field from one electrode extends in the whole detector. Therefore current is also flowing in pixels where no charge is collected, however the integral will be zero. So charge collected in, for instance electrode 3 will cause current to also flow in all the other electrodes, even those so far away that no charge is collected there. This is important to understand why hits not caused by actual charge collection are seen in the Timepix3 data. These so called halo hits will be discussed in detail in section 4.4.

4.2 Antiproton-nucleus annihilation measurements

In this section, I will provide a description of the measurement set-up that was commissioned, along with the data that will be compared with the simulations. The findings of this work, along with my contribution, will be reported in an upcoming publication.

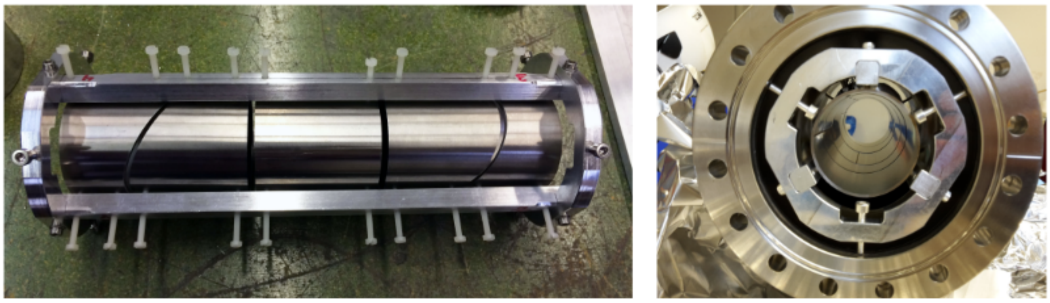

Figure 4.5: Photos of the Einzel lenses used for the measurement of products of antiproton annihilation at rest. This device is an electrostatic lens needed to focus the antiproton beam. Left photo: lateral side of the lenses, the five electrodes with the two diagonal cut can be seen. Right photo, lenses mounted inside the pipe of the line.

4.2.1 Detector setup

In chapter 3, I explained the scheme of the ASACUSA-CUSP experiment. As previously stated, the setup for measuring slow antiprotons was compatible with the same ASACUSA-CUSP line, with only minor adjustments needed to accommodate the experimental equipment. Compared to the anti-hydrogen spectroscopy experiment the main changes were made downstream the CUSP trap. The microwave cavity and the sextupole magnet have been removed from the line so that the flight path of antiprotons to the foil is shorted. The spectroscopy antihydrogen detector setup was modified, but not totally replaced. The hodoscope has still been used for the tracking of annihilation products while the other components for the detection were designed and built brand new at the Stefan Meyer Institute.

For this measurement a system of Einzel lenses was added to the usual setup of the line. The Einzel lens system is an electrostatic lens that focuses the antiproton beam without changing its energy. It consists of five individual electrodes, but it can be regarded as a

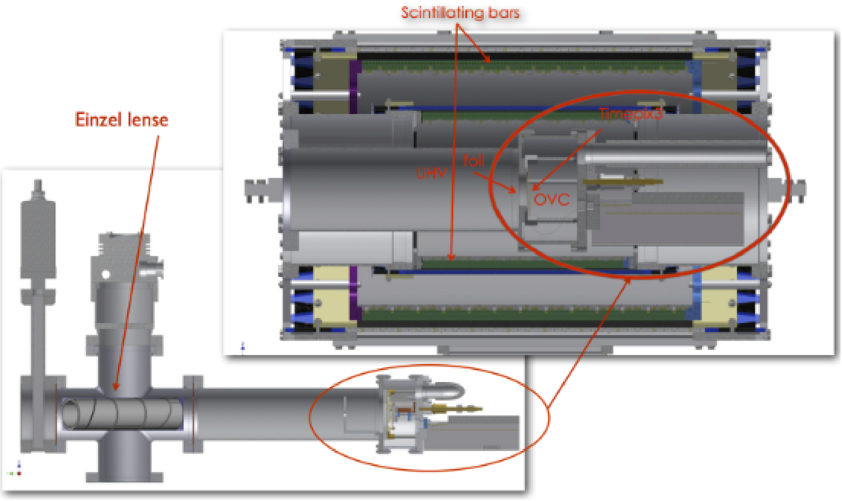

Figure 4.6: 2D rendering of the setup of the antiproton annihilation at rest experiment. In the background the tee junction inserted after the CUSP trap Inside the tee the Einzel lenses are placed. After the tee a long nipple which goes inside the hodoscope, not drawn in the background. In the foreground lateral view of the hodoscope and the Timepix3 holder at the center of it.

conventional three elements Einzel lens, where both the entrance and exit elements have an additional diagonal cut, see photos in figure 4.5. The orientation of the cuts was chosen such that two-dimensional steering has been possible by applying voltage differences between the two sections of the entrance and exit element. This Einzel lens system was installed just after the CUSP trap, in a four-way cross that hosts it. The purpose of this device is to focus and center the antiprotons, so that they hit the active area of the Timepix3 detector. The voltages applied to these devices is of the order of hundreds of volts, when dealing with antiprotons with energy of the order of hundreds of eV. In particular the best focusing effect was observed when applying about 170 V to the central electrode. The remaining four electrodes received voltages between 40 V and 83 V in order to steer the beam to the center.

The setup for the experiment involved positioning the target foil at the center of the hodoscope and placing the Timepix3 detector sensor, the pixel semiconductor detector presented in section 3.6, 1 cm downstream of the foil. In particular the Timepix3 detector used in the experiment was a quad array of 2×2 Timepix3 ASICs, which consisted of 256×256 square pixels with a pitch of $55\,\mu$m and a total active area of $28 \times 28\,\text{mm}^2$. The readout module was an ASIC readout module provided by the Medipix collaboration at CERN, while the SPIDR Compact was based on the FMC connector standard and a Xilinx 7-series FPGA, and was provided by NIKHEF. The silicon sensor had a thickness of $500\,\mu$m and was manufactured with p-readout n-bulk technology. It was purchased from ADVACAM and bump-bonded to the quad. The bias voltage used for depleting the sensor was 150 V

The hodoscope described in Section 3.5 has undergone significant changes compared to the one used in this measurement and the one I simulated. In the past year, it has undergone a major upgrade, which is described in detail in [21]. The only change that is worth to mention, since it impacts the simulation I am presenting in the following, concerns the structure of the layers between the layers parallel to the beam. In these measurements, these two layers were made up of scintillating fibers perpendicular to the beam, running around two cylinders with radii of 1 cm each.

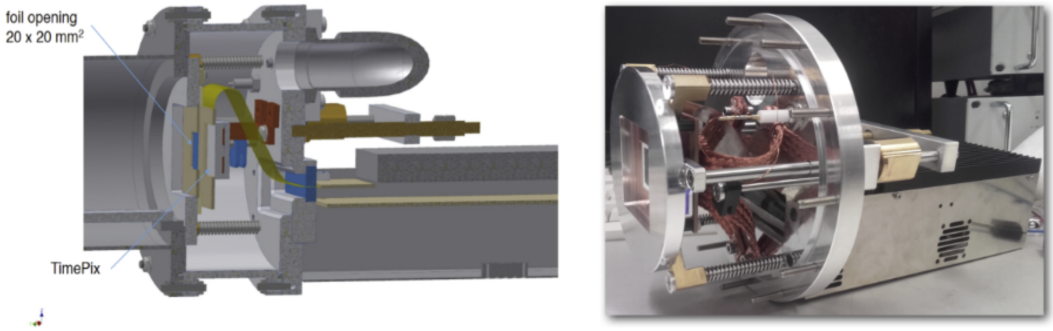

Figure 4.7: Left side, 2D rendering of the Timepix3 and foil setup. The chips is right behind the foild, both are indicated with arrows. Right side, photo of the same setup. Images from [126]

Finally the $20 \times 20\,\mathrm{mm}^2$, $2\,\mu$m thick target foils were made: one of gold, one of carbon and one of molybdenum. Each foil was positioned 1 cm in front of the Timepix3 quad detector, which was mounted on an aluminum support. The heat was conducted to the back flange via copper braids. The foils were necessary to separate the UHV ($\approx 10^{-9}$mbar) in the CUSP trap from the vacuum in the Timepix3 chamber ($\approx 10^{-6}$mbar). The vessel on both sides of the foil was first evacuated to $\approx 10^{-5}$mbar and then the foil was pressed with springs against the opening between the UHV and outer vacuum chamber regions before the upstream part was evacuated to UHV pressures. Figure 4.6 shows a sketch of the modified apparatus after the CUSP trap, while figure 4.7 displays a 3D drawing of the Timepix3 layout along with a photograph of the actual system.

4.2.2 Data overview

The data were acquired towards the end of the beam-time prior to a long shut down. They comprise of annihilations of 150 eV antiprotons from the MUSASHI trap on thin foils of

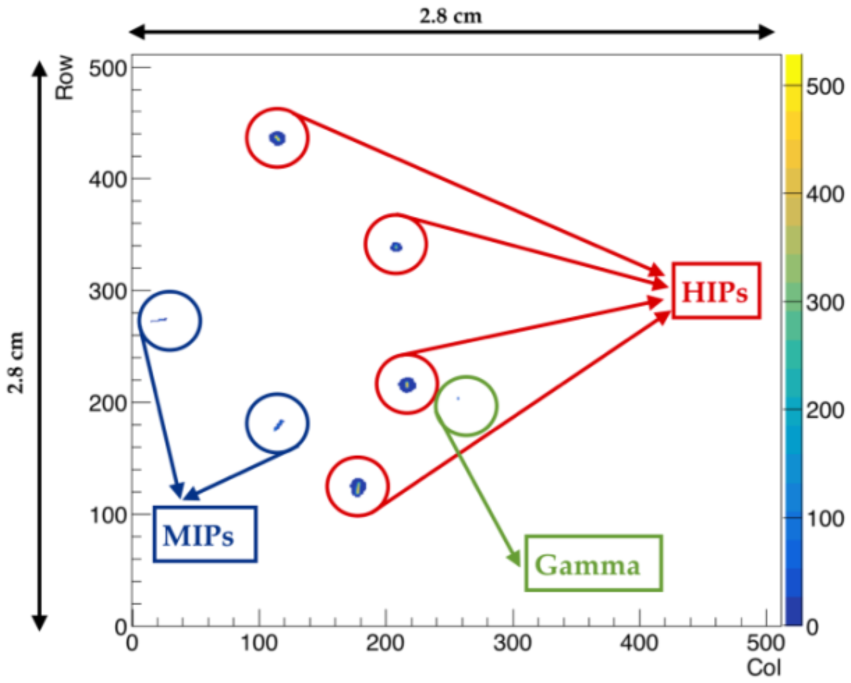

Figure 4.8: Typical event registered by the Timepix3 quad detector. In this plot the whole sensor, composed by the 4, $1.4 \times 1.4\,\text{cm}^2$, Timepix3 sensors is shown. On the axis the number of rows (Y axis) and columns (X axis) is reported and the total length ($2.8\,\text{cm}$) of two Timepix3 sensor is shown. In this particular event HIPs (red), MIPs (blue) and gamma (green) signal are indicated.

various materials. The annihilation prongs were detected using both the hodoscope and Timepix3 detectors, which shared a common run control for synchronization purposes. Events detected by the hodoscope triggered the SPIDR R/O and the event was time-stamped in the continuous Timepix3 data stream. A voltage within the range of $500 - 1000\,\text{V}$ was applied to the foil to further focus the antiprotons. The slow extraction of the antiprotons lasted for approximately $20\,\text{s}$ and a data collection run for around $70\,\text{s}$. The hodoscope recorded about 1000 triggers/run, and the Timepix3 which has an acquisition frequency of $40\,\text{MHz}$, recorded more events. However, only the events that were recorded by both detectors will be used for the study. There are approximately $9 \cdot 10^4$ annihilations at rest available for analysis, which were collected during 380 extraction cycles.

Generally, the Timepix3 data are extremely clean with a negligible background. Most events exhibit MIPs and HIPs. Figure 4.8 shows a typical Timepix3 signal event. The heavy fragments can be distinguished from the light particles based on the energy deposited per cluster and pixel, as well as the shape of the clusters. Tracks from heavy charged particles, including α particles, are much wider than MIP tracks and also deposit more energy. Additionally, photons are detected, but they are not of interest for this project at this level.

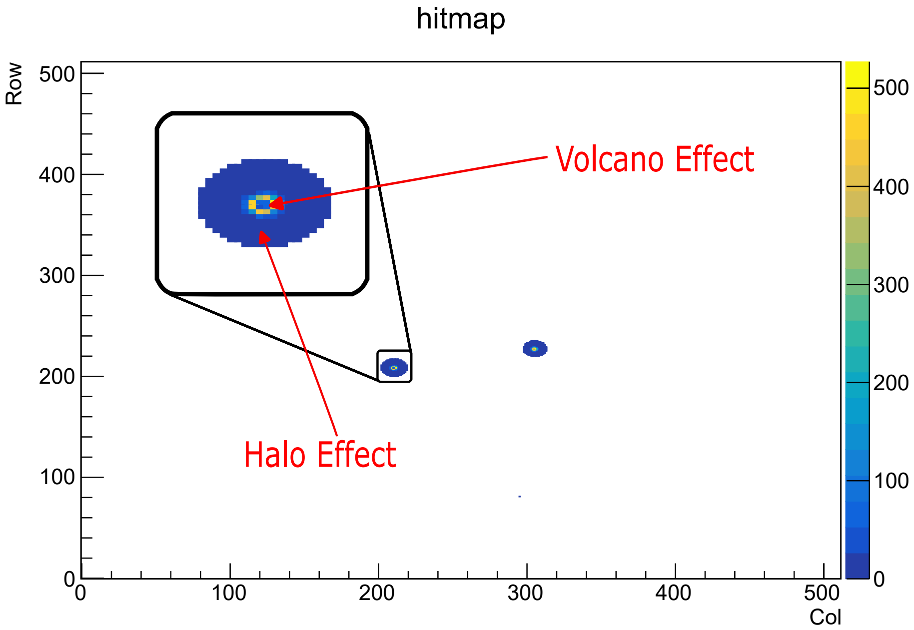

Figure 4.9: Example of event registered by Timepix3. HIPs signal is zoomed so to show the two main effect of Timepix3 sensor: Halo effect and Volcano effect. The former results in the large halo of pixels with a low deposition around the pixels of high energy depositions. The latter results in pixels with low energy depositions at the center of the pixels with high energy deposition. See text for discussion of these two effects.

It is worth mentioning that two behaviors of the Timepix3 sensor were taken into consideration during this project. The read-out system of this detector has imperfections that must be taken into account when analyzing the data. Referring to Figure 4.9, two characteristics can be noticed that distinguish the signals left by HIPs. The first is the halo of pixels registering a low deposited energy, around what is the true signal of the particle. This is called the halo effect, which I have already mentioned in Section 4.1.2. To further highlight how this read-out behavior affects the data, Figure 4.10 shows the energy deposited in all the pixels for all runs for the gold target. A peak can be seen at around $400 - 500$ eV. Around 40% of the pixels have a measured energy below 6 keV, and this excess of low energy hits are the halo hits. The halo hits cannot be caused by real particles since, on average, MIPs generate a much larger energy deposit traveling the 55 μm wide pixel. The number of pixels with a measured energy below 6 keV is therefore unnaturally large.

The exact reason why the halo hits occur is not fully understood. However, the current explanation relies on the non-uniformity over time of the current integration of the front-end. As discussed in Section 4.1.3, a charge moving in the Ramo field of a pixel will cause an induced current in that pixel, and for a large energy deposition, a significant current will flow also in pixels far away from where the charge is collected. The integrated current for those far pixels should be 0 since no charge is actually collected in that pixel. Defects in the front-end operational electronics could lead to non-uniform time integration of the signal over time. Since the current flows over a long time period due to the high amount of charges created by the deposition, this integration non-uniformity results in a small integrated net current. This small integrated current is probably what causes the halo hits[3]. This effect was addressed by manipulating the data. In fact, a cut was applied to the deposited energy in which the minimum energy deposited in a single pixel per MIP was taken into account.

The second effect, on the other hand, appears as a cluster of pixels registering low deposited energy values in the center of what should be the signal left by the HIPs. Recalling

---

[3] There are also other type of effect that can cause a halo, such as the charge sharing effect and the capacitive coupling. The halo effect, however, involves pixels at longer distances from the effective energy deposition than the one mentioned, making it a predominant effect when looking at the number of pixel with deposited energy.

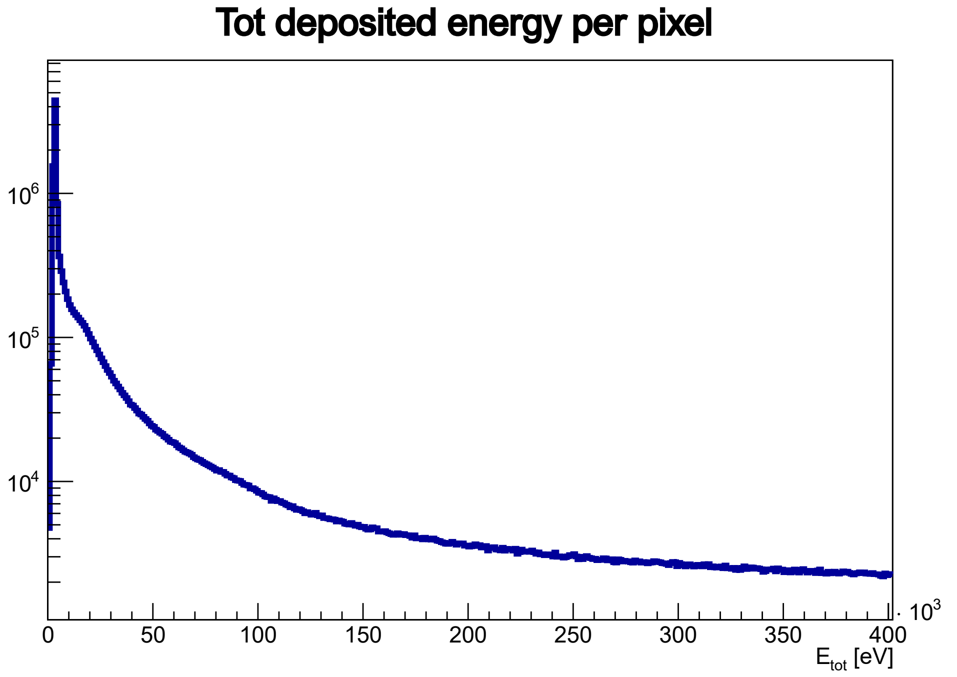

Figure 4.10: Distribution of energy deposited in a pixel for all the events registered during data taking. The first pick around 6 keV is caused by the Halo effect (see text).

the image of a crater seen from above, this effect is called the Volcano effect. The volcano effect is a disturbance in the readout when a pixel experiences a large energy deposition, causing a single pixel to read out a random lower energy deposition instead of the amount actually collected at the electrode. This effect has been observed in several experiments [127, 128, 129]. Although the exact explanation is not completely understood, recent studies suggest that the volcano effect is consistent with the Timepix readout chip having an internal protection circuit for very high input charges [129]. One of the previous studies on the volcano effect contained quantitative information about the pixels in each cluster that had the highest read energy depositions [127]. This study, carried out at the Heavy-Ion Medical Accelerator (HIMAC) in Chiba, Japan, exposed a $300\,\mu$m thick Timepix3 detector to high energy heavy ions of type O, Ne, Ar, and Fe with energies between 230 MeV and 526 MeV. The comparison between the data and theoretical predictions showed that between 40% and 93% of the energy was not read out, with the exact fraction depending upon the particle type and its energy. In a single pixel, the read-out energy never exceeded 600 keV.

4.3 Geant4 simulations and $Allpix^2$ digitizations

In this section, I present my first contribution to the project. At the beginning of my PhD, simulations of the measurement using Geant4 were already developed. A key step to be able to compare them with the collected data is to digitize the simulated deposited energy. Here, I will briefly discuss the simulations carried out in Geant4, which have been developed in [21]. Then, I will discuss the digitization work. In this section, I will report various plots to show the results of digitization. As the process was repeated for the simulations with the different targets, only a few plots have been chosen for the main body of the thesis. The plots that will not be reported below are included in appendix A.

4.3.1 Geant4 simulations

Geant4 simulations have been developed by the Vienna group of the collaboration for several parts of the apparatus of the experiment. In particular, the geometry of the entire antihydrogen annihilation detector system at the end of the line, described in section 3.6, has been implemented with great detail. This includes the geometries of the hodoscope, the BGO detector, and finally also the Timepix3 detector.

I used these simulations as a reference to implement the FLUKA simulations, both for the geometry and the simulation output. In particular, the output needs to satisfy the requirements of the analysis phase, which requires a specific format.

For the simulations used in this work, 50,000 antiprotons were generated for each of the three targets, so to replicate the statistics of the data taken during beam time. Each run was repeated with two physics lists based on the two models mentioned before: CHIPS and

FTF. The former is no longer maintained or used in the current version of Geant4 [4], but it was nevertheless included in the study to allow comparison with previous work. As an example to demonstrate these two models in action, in the plots of Figure 4.11, I present integrated deposited energies in carbon along the path within the Timepix3 detector for different particle types. Specifically, in Figure 4.11d and 4.11b, I report the deposited energy of pions and kaons, which are defined as MIPs, and the combined contribution of the two distributions is shown in Figure 4.11f. In Figures 4.11c and 4.11a, the deposited energy distributions of protons and heavy ions (tritium, deuterium, and alpha particles) are shown, which form HIPs, and the combined distribution is presented in Figure 4.11e. It is evident that there is a clear difference between these two models in reproducing the products of the annihilations of antiprotons at rest, at least with respect to the deposited energy. The most significant differences are observed in the reproduction of HIPs. The difference is not only in the total energy distribution for HIPs but also in their composition. The deposited energy for HIPs simulated with the FTF model is equally contributed by protons and heavy ions, whereas in CHIPS, proton production predominates. These differences between the two models are given by the different approaches at the base of the models and the fact that there are limited data for antiproton annihilations at rest[5].

The deposited energies are the starting point for digitizing the signal. In the following section, where I will report on the work for digitization and beyond, I will refer to these quantities as raw energies (i.e., not digitized). In the subsequent sections, I will characterize the digitization and show the effects of this procedure on Geant4 simulations made with the FTF model. However, the digitization has been applied to all simulations, including FLUKA, Geant4 with CHIPS model, and Geant4 with FTF model. Additionally, in order to assess the output of the FLUKA simulations, I will compare their output with that of Geant4 simulations. As the data used for this work have not been published yet and they were taken previously this thesis work, for rules of the collaboration a direct comparison with experimental data cannot be reported.

4.3.2 $Allpix^2$ implementation

The digitization process of the deposited energy is ultimately a stochastic process that needs to be simulated. Allpix2, [130, 131], a software program specialized in digitizing signals from semiconductor sensors, has been selected for use in this project.

$Allpix^2$ is a generic simulation framework for silicon tracker and vertex detectors written in modern C++, following the C++17 standard. As stated by the authors of the software, the goal of the $Allpix^2$ framework is to provide an easy-to-use package for simulating the

---

[4] https://geant4.web.cern.ch/download/release-notes/notes-v10.0.0.html

[5] This has not to be related with the maintenance of CHIPS to be interrupted, which has been a choice made as part of a bigger project of renewvation of the entire code.

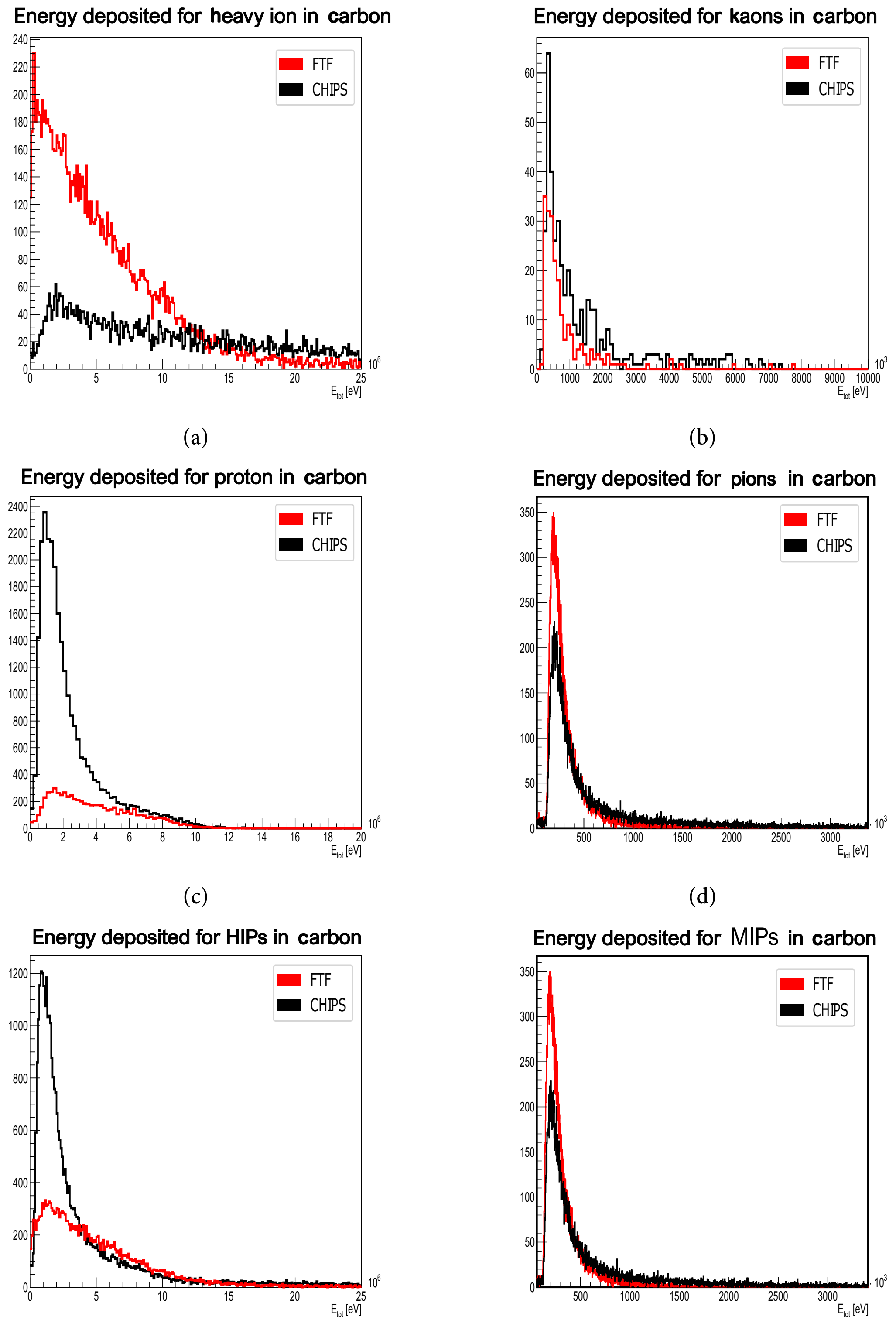

(a) (b)

(c) (d)

(e) (f)

Figure 4.11: Energy distribution for all the events simulated with two physics model (CHIPS in black, FTF in red) used in the Geant4 software. (a) Energy deposited by heavy ions, (b) energy deposited by kaons, (c) energy deposited by protons, (d) energy deposited by pions, (e) energy deposited by HIPs and (f) energy deposited by MIPs. The energy deposited by HIPs is given by the energy of both (a) and (c), while the energy of MIPs is given by (b) and (d).

performance of silicon detectors, from the ionizing radiation through the sensor and to the digitization of hits in the readout chip.

The framework builds upon other packages to perform tasks in the simulation chain, most notably the same Geant4 our collaboration is going to test, for the deposition of charge carriers in the sensor and ROOT for producing histograms and storing the produced data. The core of the framework focuses on the simulation of charge transport in semiconductor detectors and the digitization of hits in the frontend electronics. Although $Allpix^2$ has the capability to reconstruct the detector geometry using Geant4, this step was unnecessary in this case as the energy deposition had already been simulated using Geant4 and FLUKA.

I performed digitization in the following steps:

1. As the first step, the necessary geometry is defined. In our case, only the Timepix3 quad semiconductor sensor at the provided position is defined.

2. A linear depletion electric field is generated inside the semiconductor. This means that the field has a constant slope determined by the bias voltage provided as a hyperparameter.

3. The program retrieves the energy deposition data along with the corresponding 3D positions from the simulation's ROOT file. At this point, the number of electron/hole pairs resulting from the energy deposition is determined by calculating the mean pair creation energy, and modeling fluctuations using a Fano factor based on Gaussian statistics.

4. The generated charges are then projected onto the sensor surface and randomly diffused. The diffusion of the charge carriers is realized by placing sets of a configurable number of electrons in positions drawn from a two-dimensional Gaussian distribution around the projected position at the sensor surface.

5. Once the charges are projected onto the sensor, they are mapped to the nearest pixel using a process that disregards any propagated charges that are too far from the implants or outside the pixel grid.

6. The final step involves translating the collected charges into a digitized signal proportional to the input charge. This process also simulates noise contributions from the readout electronics, modeled as Gaussian noise.

These steps were applied using the standard tools available with $Allpix^2$. In addition, to further improve the simulations, the Volcano discussed in section 4.2.2 was also used.

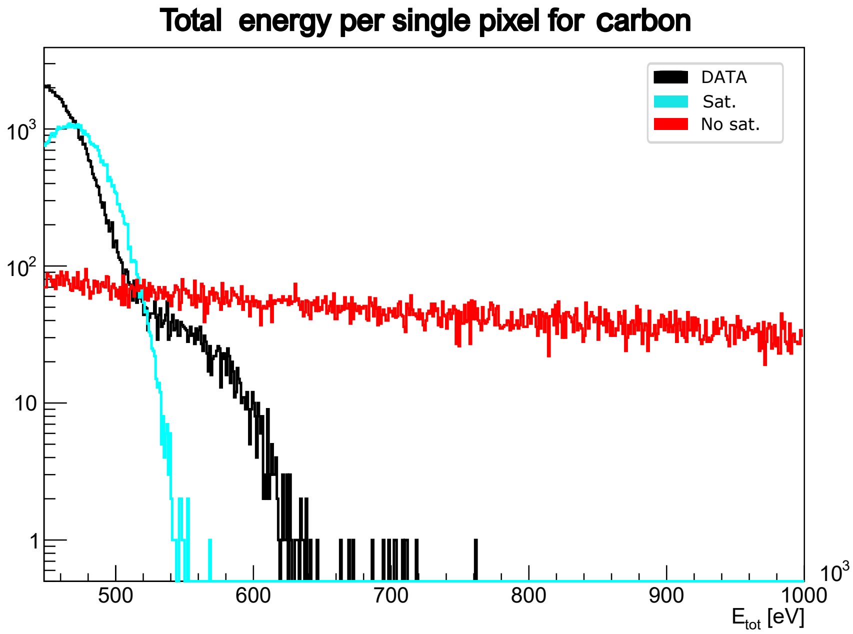

Figure 4.12: Distribution of total energy deposited in single pixel for high energy depositions from products of annihilation on carbon. (black) Energy deposited for real data. (light blue and red) Energy deposited for Geant4 simulation with the FTF model, digitized respectively with and without taking into account the saturation that causes the Volcano effect (see text for discussion).

4.3.3 Digitized Geant4 simulations

As previously discussed in relation to the Geant4 simulations, the Timepix3 detector provides crucial information for identifying HIPs and MIPs, and the signal can be analyzed at the pixel or cluster level. Since MIPs and HIPs are distinguished based on the energy deposited in the sensor, it is important to accurately reproduce the deposited energy distribution at the cluster level after digitization. Thus, it was necessary to consider the Volcano effect described in section 4.2.2 to improve the simulations. Figure 4.12 illustrates the importance of accounting for this effect. The red and black lines show a significant mismatch between the digitized FTF model simulation and the actual data when the standard implementation of $Allpix^2$ was used. This is evidenced by the large difference in the total energy per individual pixel for the C target in the last part of the spectrum. The light blue line shows the same digitized simulation after implementation of the Volcano effect.

As previously mentioned, the Volcano effect is caused by large and dense energy depositions. Notably, there are no energy deposition entries above approximately $\approx 650\,\text{keV}$. Additionally, in real data, the maximum measured energy deposition within each cluster

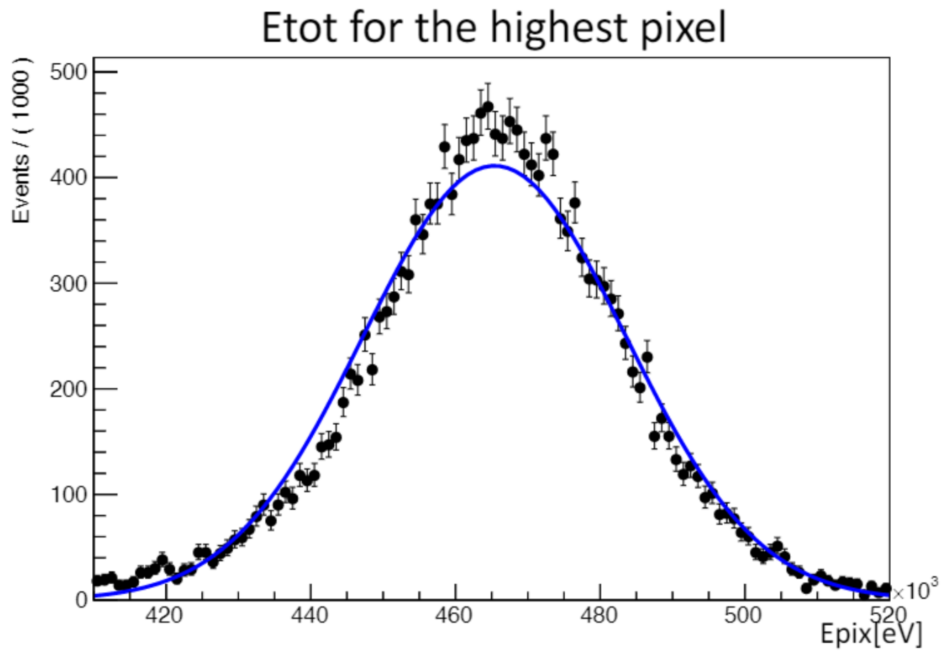

Figure 4.13: Distribution of energy deposited in the pixel with highest energy for each cluster in real data. A Gaussian fit with a mean of 465 keV and a standard deviation of 30 KeVis superimposed to data, blue line.

can be identified by selecting the pixel with the highest energy measurement. A distribution of the maximum energy per cluster can then be plotted. In figure 4.13, this distribution is shown, following a Gaussian distribution centered at 460 keV with a standard deviation of 30 keV. This trend of maximum energy distribution per pixel from heavy ions was also observed in [127]. However, their setup had different parameters, as the distribution appeared to follow a Gaussian with a mean of around 500 keV and a standard deviation of around 50 keV.

I therefore implemented a saturation option in the $Allpix^2$ code in collaboration with the developers. This option sets all pixels with an energy deposition above a certain value to a random value following a Gaussian distribution centered around the saturation value. In our case, the saturation value was set to 460 keV with a standard deviation of 30 keV. The effect of this correction is clearly visible by observing the light-blue line in Figure 4.12. As can been seen, the data (black line) are not replicated exactly, this can be due to the fact that I implemented the Volcano effect so that it is applied to all the pixels above the saturation value. This sharp cut in energy can be too simplistic of a choice, moreover I did not implemented any possible dependence on energy of the random distribution of the effect, which can broader the final energy deposited per pixel distribution. Nevertheless, the main feature of having a defined cut given by a saturation effect has been replicated.

It is important to note that the saturation effect should not be applied indiscriminately to all particles identified as HIPs. In particular, it should be noted that the alpha particles that are categorized as HIPs do not exhibit this Volcano effect, as demonstrated by Figure 4.14. The figure depicts the energy deposition for alpha particles simulated with Geant4, under three different conditions: not digitized, digitized with saturation enabled, and digitized without saturation. The energy distribution deposited by alpha particles was measured using a source for a characterization of our setup, and all of these are overlapped with it. Geant4 accurately simulates the distribution of deposited energy. While $Allpix^2$ reconstructs clusters with the correct energy deposition per cluster even without the saturation option activated, if saturation is activated, digitization fails dramatically. This is apparent when referring to the energy deposited per pixel, as illustrated in Figure 4.15. The figure presents the measured distribution for alpha particles, cosmic rays, and measurements of annihilation of antiprotons in gold and carbon targets. As can be seen, the distribution drops significantly at around 400 keV in the case of alpha particles. This is due to the fact that alpha particles, even if they are HIPs, deposit less energy than bigger products such as

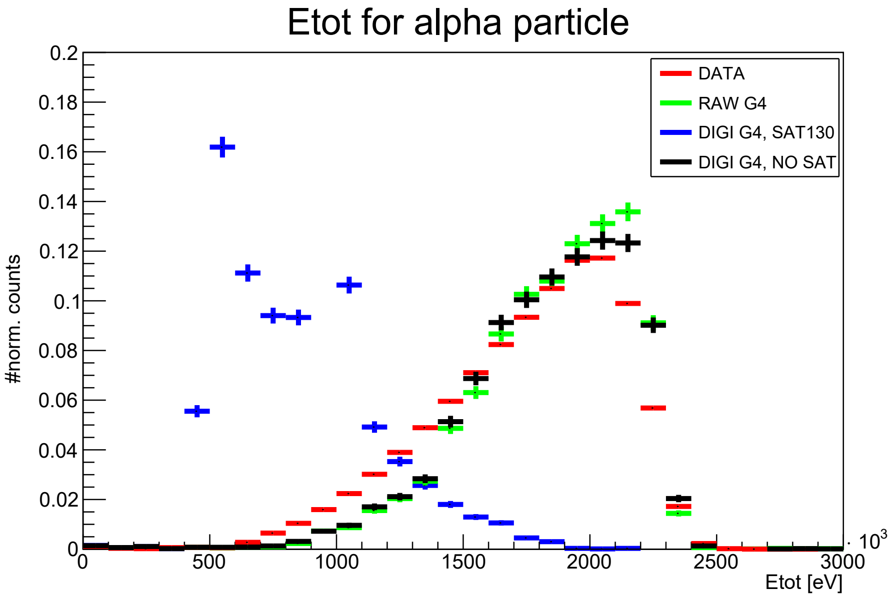

Figure 4.14: Normalized distribution of total energy deposited only from alpha particles for real data (red) taken with an alpha particle source, Geant4 raw simulation (green), Geant4 simulation digitized without using saturation option (black) and Geant4 simulation digitized using the saturation option (blue). As can be seen, we cannot apply saturation indiscriminately to all HIPs, since for alpha particles this effect is not present.

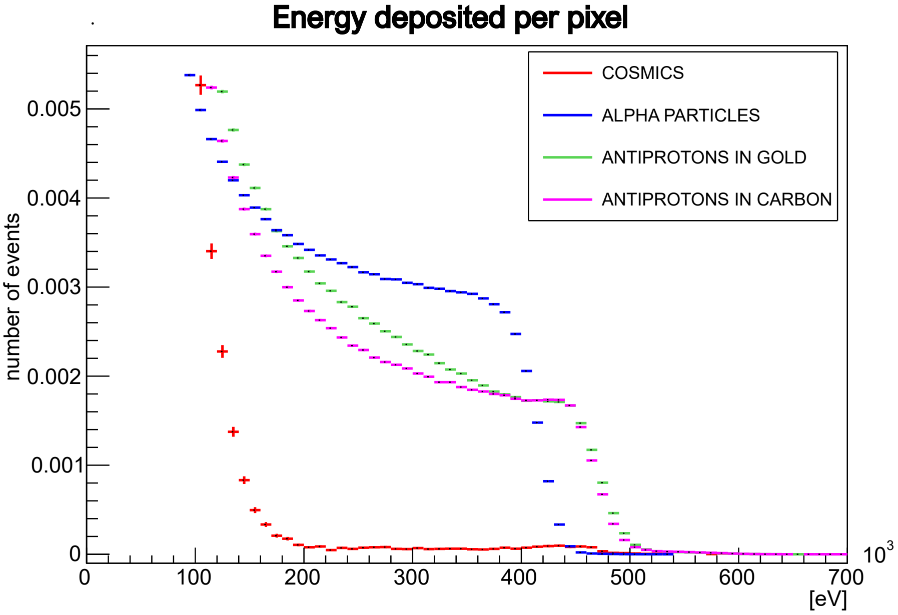

Figure 4.15: Normalized distribution of total energy deposited in a single pixel for alpha particles (blue) measured with a alpha source (Am241), cosmic rays (red), products of annihilations of $\bar{p}$ in gold (green) and products of annihilations of $\bar{p}$ in carbon (pink). As can be seen the alpha particles never reach the saturation threshold of 460 keV. Hence no saturation should be applied to those.

tritium, deuterium. This is because being lighter, they are emittted with higher momenta than other HIPs products and thus, following the Bethe-Bloch law, they release less energy. For this reason, I have excluded the effect of saturation for alpha particles when applying digitization to the simulations. After ensuring that the known effects of the Timepix readout were taken into consideration, some consideration about the energy distribution by cluster can be done. An example of energy distribution for the carbon target is presented in Figure 4.16 for HIPs and in Figure 4.17 for MIPs. For other targets, please refer to Appendix A. Both figures display the integrated energies of the raw simulations, along with the energies associated with the clusters that were reconstructed via digitization. The distributions of total energy depositions per cluster for digitization with and without saturation are also depicted. The saturation effect solely affects HIPs without altering the digitization of MIPs. Otherwise, the energy distribution is accurately reproduced. Given that the identification of MIPs and HIPs is primarily based on energy deposition, this information was crucial for comparing the simulated signal with the data. While cluster size is another factor that could be utilized, for our project, this information will not be employed since $Allpix^2$ could not accurately replicate this factor, as depicted in Figure 4.18. The figure illustrates the number of pixels per cluster for the simulation of digitized carbon, along with both raw data and data following the cut to account for the halo effect. The digitization noticeably underestimates the size of the largest clusters. In fact, the maximum number of pixels per cluster is less than 100, whereas clusters of measured HIPs also exceed several hundred pixels. This underestimation results in clusters for HIPs in simulations having sizes comparable to those of MIPs, making it impossible to use this information for identification purposes. To overcome this problem, a more refined simulation of the propagation step in the digitization should be done, where different models of deposition of the carriers on the sensor should be investigated. For time reasons and also because the reproduction of the cluster sizes was not essential, this step has not be done for this thesis work.

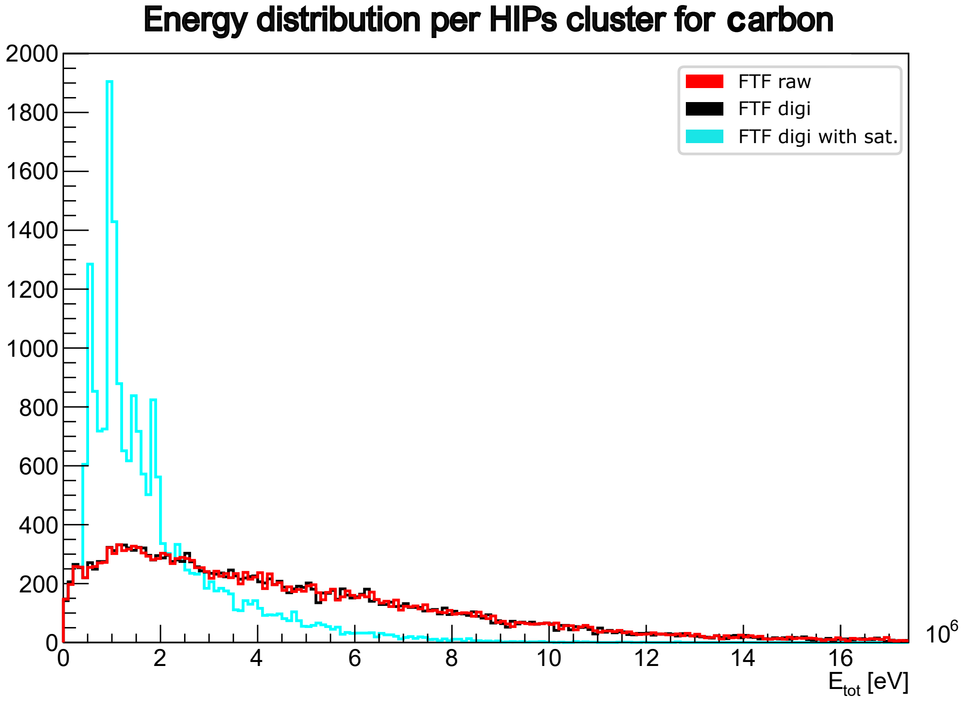

Figure 4.16: Distribution of total energy deposited by HIPs from annihilations on carbon target. (red) Total energy integrated on the path inside the sensor region in raw Geant4 simulation for FTF model. (black) Total energy integrated on the cluster given by digitization, without the saturation effect included. (light blue) Total energy integrated on the cluster given by digitization, with the saturation effect included.

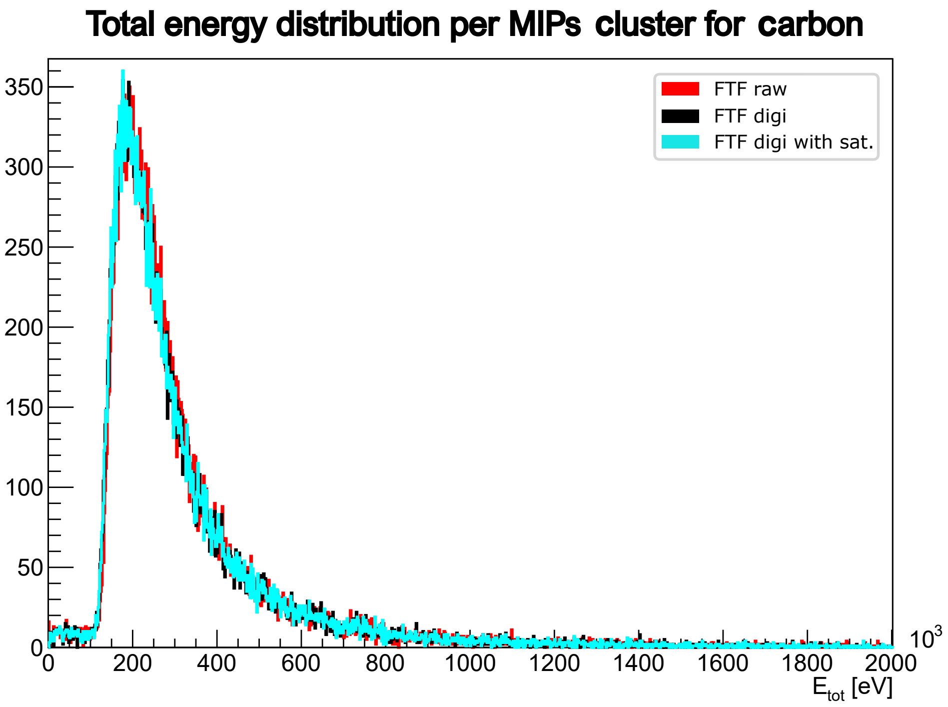

Figure 4.17: Distribution of total energy deposited by MIPs from annihilations on carbon target. (red) Total energy integrated on the path inside the sensor region in raw Geant4 simulation for FTF model. (black) Total energy integrated on the cluster given by digitization, without saturation effect included. (light blue) Total energy integrated on the cluster given by digitization, with saturation effect included.

4.4 Fluka simulations

In this section, I present the FLUKA simulation that I developed. FLUKA simulations were crucial for conducting a comprehensive comparison between the data obtained by ASACUSA and the MC simulation software used by the scientific community in the field of particle physics. FLUKA is one of the leading MC software, alongside with Geant4, used globally for simulating the effect of experimental apparatus in particle physics. As with the section dedicated to digitization, results that are not included in the main body of the dissertation are reported in Appendix A.

4.4.1 FLUKA overview

FLUKA is a versatile tool that can simulate the transport of particles and their interactions with matter, covering a wide range of applications that span from proton and electron accel-

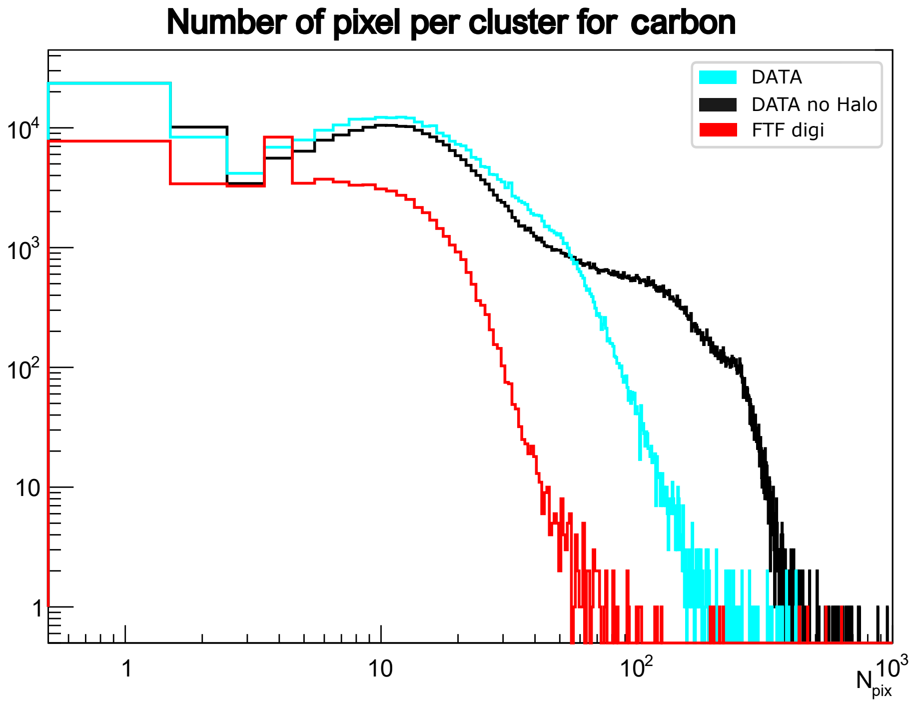

Figure 4.18: Distribution of number of pixels per cluster from annihilation on carbon target. (light blue) Pixels per cluster for real data. (black) Pixel per cluster for real data after deposited energy cutoff so to take into account the halo effect. (red) Pixel per cluster for Geant4 simulation with the FTF model digitized with saturation effect. As can be seen, the digitization fails to reproduce the bigger clusters.

erator shielding to target design, calorimetry, radiotherapy, and more. With high accuracy, FLUKA can simulate the interaction and propagation in matter of approximately 60 different particles, including photons and electrons with energies ranging from 100 eV to 1 keV up to thousands of TeV, neutrinos, muons of any energy, hadrons of energies up to 20 TeV and their corresponding antiparticles, as well as neutrons down to thermal energies and heavy ions.

In particular we are interested in how FLUKA models the annihilation of a $\bar{p}$ with a nucleus. The process occurs in two steps. In the first step, the antiproton-nucleon annihilation produces pions and kaons, with the branching ratios to different pionic multiplicities tuned to experimental data. In the second step, the interaction between the nucleus and the pions that penetrate the nucleus is simulated by the PEANUT model. The model simulates the hadronic interaction between a pion and the nucleus as an intra-nuclear cascade, meaning a successive chain of two-body interactions between the projectile and reaction products.

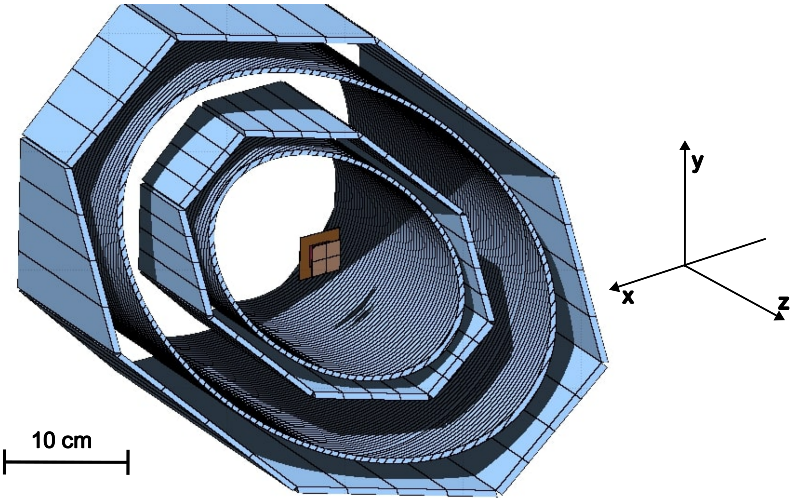

Figure 4.19: 3D rendering of the FLUKA simulation geometry. In light blue plastic scintillator components: bars and light guide of the hodoscope. In yellow at the center the 4 Timepix3 silica sensor and in front of them the foil copper holder can be seen.

This is followed by evaporation and fragmentation due to the excess energy transferred by the pions to the nucleus. As a result of the annihilation, the nucleus is fragmented, and all the fragments travel away from the annihilation point.

4.4.2 Simulations details

When starting the simulation from scratch, the first step was to select and accurately replicate the essential components of the experimental apparatus geometry. Specifically, the focus was on the sensitive parts of the hodoscope, which comprised of two layers of scintillating rods, two layers of optical fibers, the sensitive region of the Timepix3 detector (a $500\,\mu$m thick silicon layer), the copper flange utilized to secure the Timepix3 in the pipe, and the $2\,\mu$m target foil. A rendering of the two detectors is presented in Figure 4.19. To ensure that the background generated by the experimental set-up was accurately reproduced, tests conducted using a more detailed simulation developed in Geant4 indicated that it was necessary to include the copper support in addition to the sensitive components of the detectors. As a result of the antiproton spread, this element was only impacted by a small percentage of particles and contributed to the recorded signal.

Regarding the used simulation parameters, the main ones, including beam characteristics, are listed in table 4.1. To faithfully reproduce the measurement with FLUKA, it was essential to enable the transport of heavy ions and atomic fragments with the option *Iontrans*.

This required compiling FLUKA with libraries using a dedicated protocol (*ldpmqmd*). Additionally, the IONSPLIT and COALESCE options were enabled to permit the coalescence mechanism and the superposition model, respectively, which allowed the ion to split into nucleons. Enabling the PRECISION option enabled the most precise options for particle transport, making the simulation of energy deposition as accurate as possible. More details about the code development can be found in appendix A.

Palet name	Option	Comment
Defaults	PRECISIO	
Beam	Energy	Antiproton beam with 1.15 keV with a gaussian schape with 1.1 cm FWHM on X, Y axis
Part-thr	Energy	Energy threshold set to minimum for the transport of heavy ion: 10 keV
Emfcut	Transport	Energy cut for the transport of electron and photon: 10 keV, 100 eV
Emfcut	Transport	Energy cut for the production of electron and photon: 10 keV, 100 eV
Physics	COALESCE	Active
Physics	IONSPLIT	Active
Physics	EVAPORAT	Active
Iontrans	HEAVYION	Acitve

Table 4.1: FLUKA simulation configuration. The standard implementation for a FLUKA simulation requires a configuration file where commands for implementing the physics, the geometry, the features of the beam and so on are given. Every command (or palet) has different options and a maximum of 6 parameters to implement the various options. Here the main palets of the simulation with some comments are listed. More explanations of the simulation implementation is in the text or in appendix A.

4.4.3 Comparison of hodoscope simulation

The simulations performed with FLUKA were compared with those obtained using Geant4, specifically at the level of information provided by the hodoscope. A track reconstruction software was used to evaluate the accuracy of this aspect of the simulation. To detect antihydrogen annihilations, a tracking algorithm had already been developed, and its workings are elaborated in [21]. Briefly, it uses a combinatorial approach to identify track candidates by combining all hit coordinates, fitting all possible track combinations, retaining the ones with the best fits, and calculating the coordinates of the annihilation vertices. The position

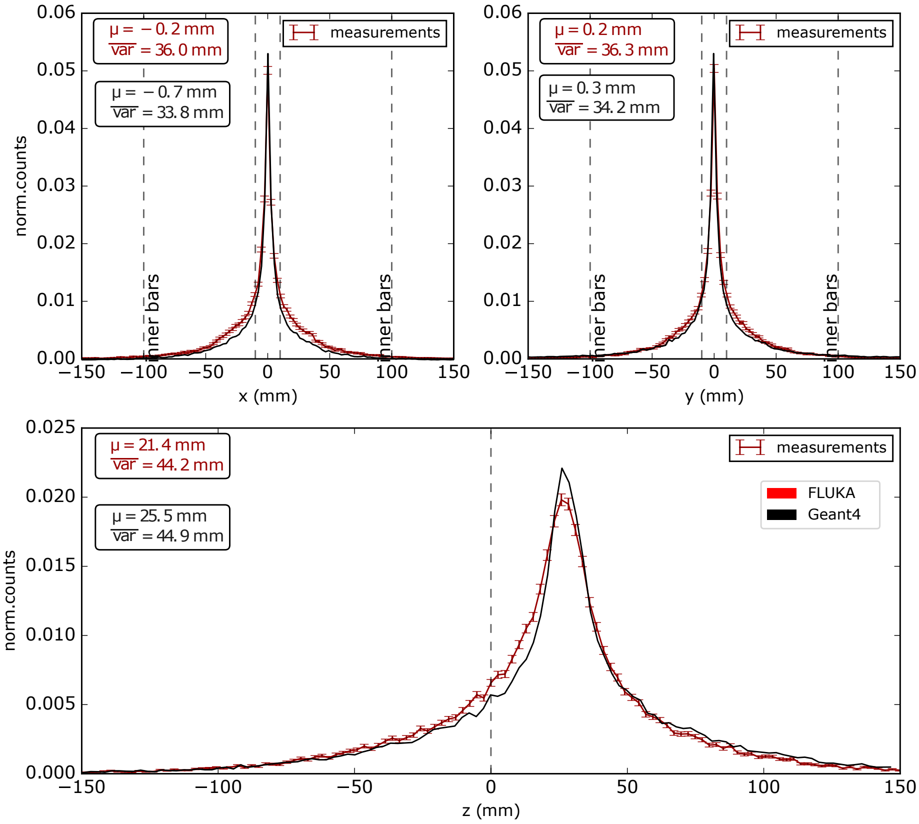

Figure 4.20: The normalised distributions of the x, y and z for simulated hits with Geant4 with FTF model (black) and FLUKA (red) for the carbon target. The histogram for the z distribution of the vertices is not centered in 0 since the center of the system is aligned with the center of the hodoscope and the annihilations occurred on the foil which was upstream the center. The x and y distributions of the two simulations agree and the average reconstructed positions are almost identical. The measured z-distribution is also in good agreement among the two simulations, with a difference between the average reconstructed positions of about 3 mm, which is within the statistical error.

of the annihilation vertices reconstructed with the hits obtained from FLUKA and Geant4 was compared, enabling the verification that the fundamental parts of the hodoscope geometry necessary to reproduce the data analysis had been accurately reproduced. Figure 4.20 displays the comparison between the positions of the annihilation vertices reconstructed with the hits obtained from the two simulations, indicating that the geoemtry and signal on the hodoscope of the FLUKA simulation is in agreement with the one of Geant4 simulation. The positions of the annihilation vertexes in the two directions perpendicular to the beam (X and Y) differ of about ≈ 0.1 mm, while the reconstructed positions on the beam axis differ of about ≈ 3 mm. Overall the differences are within the statistical error. Another important piece of information for comparison is the number of reconstructed tracks. The hodoscope is used in the data analysis to select events to study, since the number of minimum ionizing particles (MIPs) is reflected by the number of tracks detected by the hodoscope. While differences in the channel multiplicities can lead to variations in the distribution, the overall trend of the distributions should be comparable. As shown in Figure 4.21, the distribution of the number of tracks reconstructed for Geant4 with the two different models, as well as FLUKA, indicates that the simulation faithfully reproduces the depositions in the hodoscope. This information will be essential for the final reconstruction of the multiplicities of MIPs and high ionizing particles per annihilation.

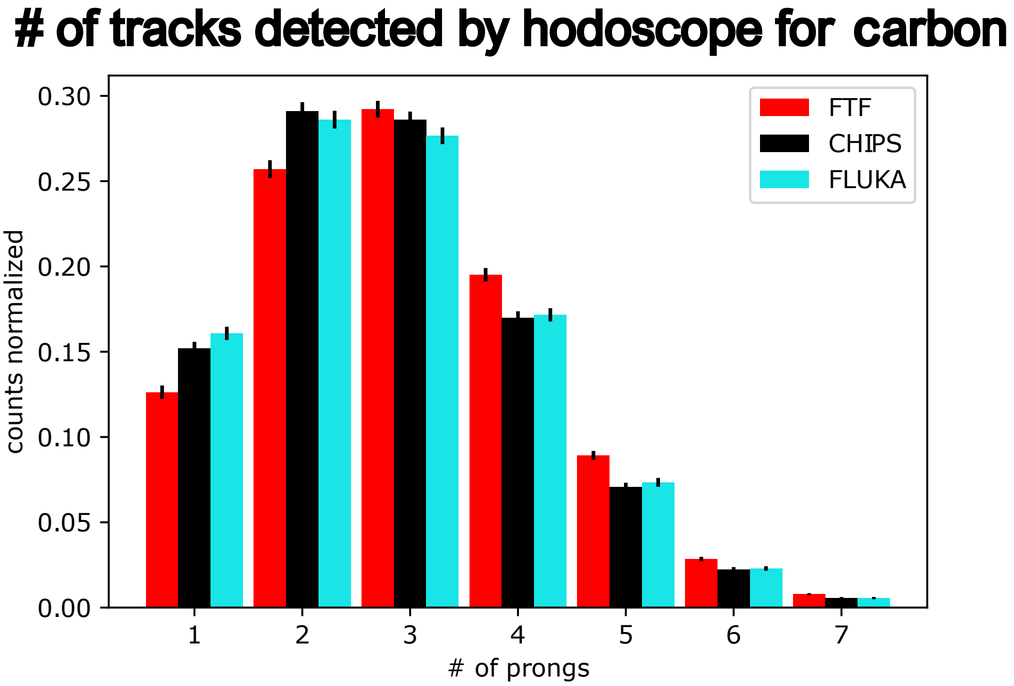

Figure 4.21: Number of tracks of products of annihilations on carbon target, reconstructed per event with the hoodoscope signal for: Geant4 simulation with the FTF model (red), with the CHIPS model (black) and the FLUKA simulation (light blue).

4.4.4 Comparison of timepix3 simulation

Finally, we can examine the results of the FLUKA simulations for the Timepix3 detector. As

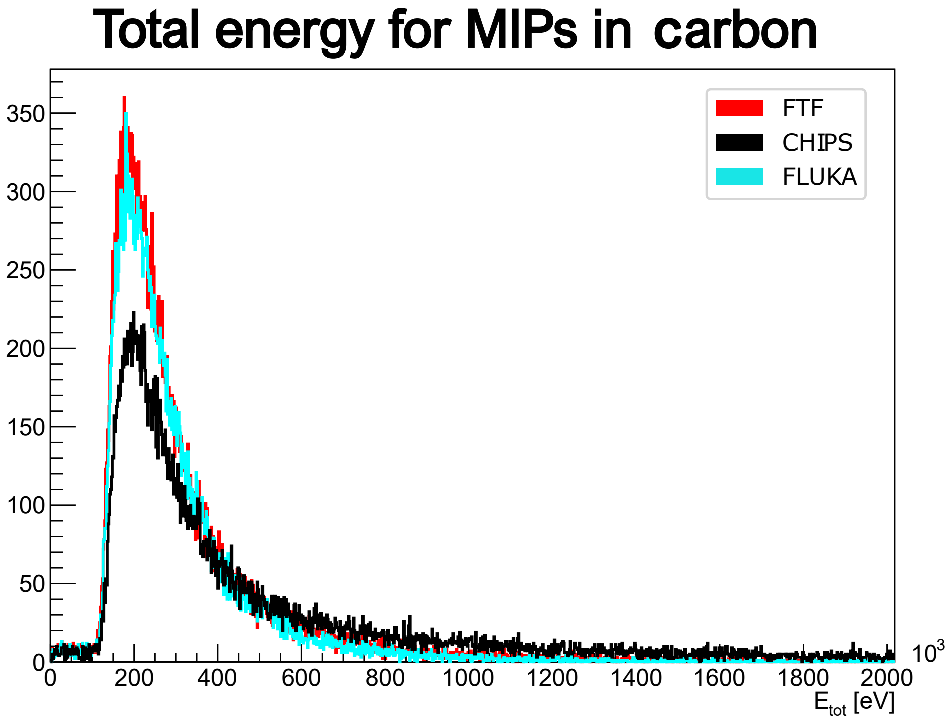

Figure 4.22: Distribution of total energy deposited in MIPs clusters for all the events of annihilations on carbon target, for Geant4 simulation with the FTF model (red), with the CHIPS model (black) and the FLUKA simulation (light blue).

with the other sections, here I present only a few examples that highlight the most prominent differences or similarities between the various models. In appendix A the plots for all the targets can be found. To give a reference for the comments reported below I also listed in table 4.2 the median, the standard deviation and number of entries values for the MIPs deposited energy distributions and for the MIPs multiplicities for all the targets and MC simulations and in table 4.3 the same values for the HIPs deposited energy distributions and HIPs multiplicities. In Figure 4.22, it can be observed that the energy distribution for MIPs is reproduced by FLUKA and the FTF model in a much similar way, while the CHIPS model shows a slightly broader distribution. However, the modes of the distributions are centered at the same energy for all three models. This is the case for carbon; for other targets, the differences between CHIPS and the other two models disappear. The multiplicities exhibit differences between the models, as shown in Figure 4.23. Some of these differences are greater than the statistical error and can be attributed to the specific used model. The

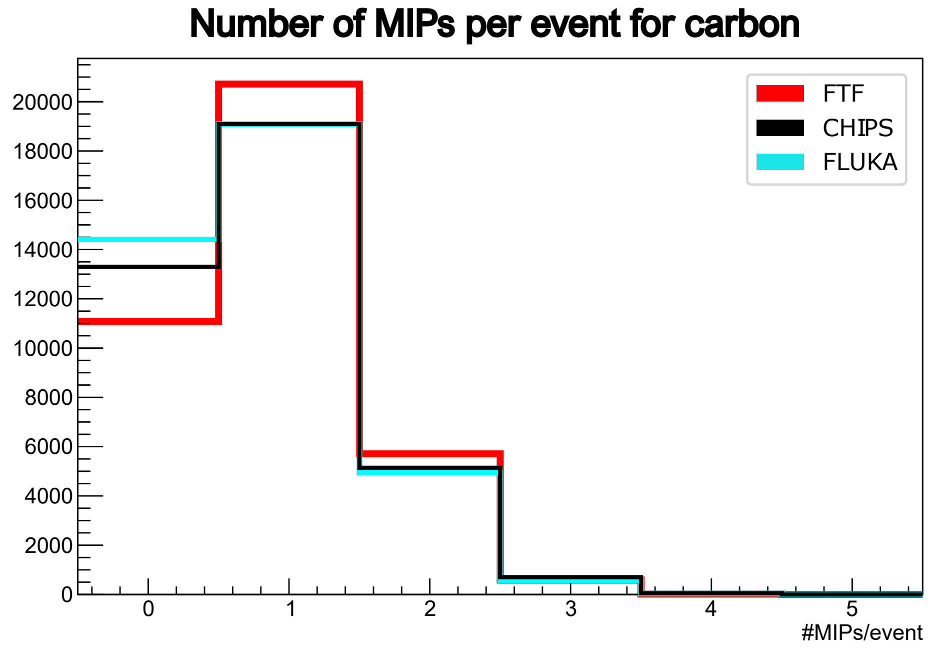

Figure 4.23: Number of MIPs per event for all the events of $\bar{p}$ annihilations on carbon target for Geant4 simulation with the FTF model (red), with the CHIPS model (black) and the FLUKA simulation (light blue).

largest differences, in contrast, occur with the reproduction of HIPs and both for their multiplicities and energy deposited per cluster, depending on the target material, as one can see from figure 4.24, where I report the number of detected HIPs per event for the gold target case. The model currently used in Geant4, FTF, generates very few HIPs compared to the previous CHIPS model. FLUKA is the model that generates more highly ionizing particles, this can be attributed to the model of the nuclear interaction given by the cascade model. This difference is present for the gold and molybdenum targets and it is less pronounced for the carbon target (see appendix A). Overall, the CHIPS and FLUKA model give more similar multiplicities distributions.

Regarding the deposited energy per cluster, the behaviour of the models is highly dependent on the material of the target. As an example I report in figure 4.25 the gold case, where, even if there is a big difference in the multiplicities, it can be seen that the energy distribution per cluster are centered in the same range of energy among the three models. For the molybdenum target case the differences among the deposited energy distributions are big also shape wise, while for the carbon target case the distributions are much more similar, even though they still present some minor differences. This could be related to the fact that for the carbon target much more experimental data are available for tuning of the model. This, too, is an indication that the differences among the various models can be attributed to reaction modeling rather than particle transport.

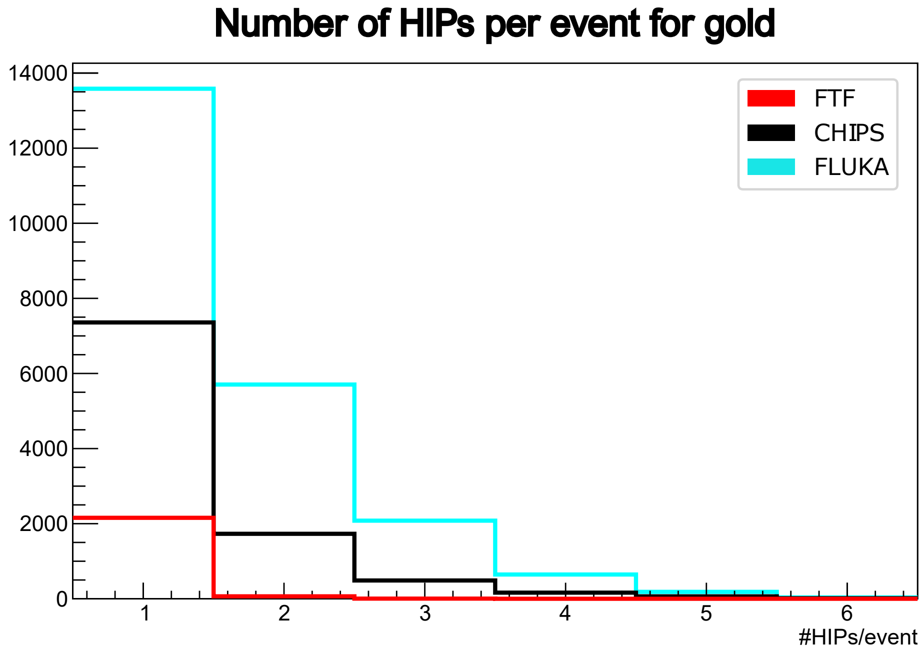

Figure 4.24: Number of HIPs per event for all the events of $\bar{p}$ annihilations on the gold target for the Geant4 simulation with the FTF model (red), with the CHIPS model (black) and the FLUKA simulation (light blue).

To summarize, differences in terms of multiplicity are evident not only between FLUKA and the Geant4 models, but also between the CHIPS and FTF models themselves. These differences are particularly pronounced for the gold and molybdenum targets and are extremely marked for the multiplicities of highly ionizing particles (HIPs). The FTF model in particular seems to complitely fail in reproducing HIPs multiplicities and deposited energy distributions for gold and molybdenum. Moreover, the CHIPS model seems to give always a higher energy depositions and multiplicities for MIPs. Whereas the FTF and FLUKA models seem to reproduce comparable trends regarding deposited energy distributions per cluster and multiplicities for MIPs.

These results represent the final product of my contribution to this project and will be compared with real data for empirical characterization of the models.

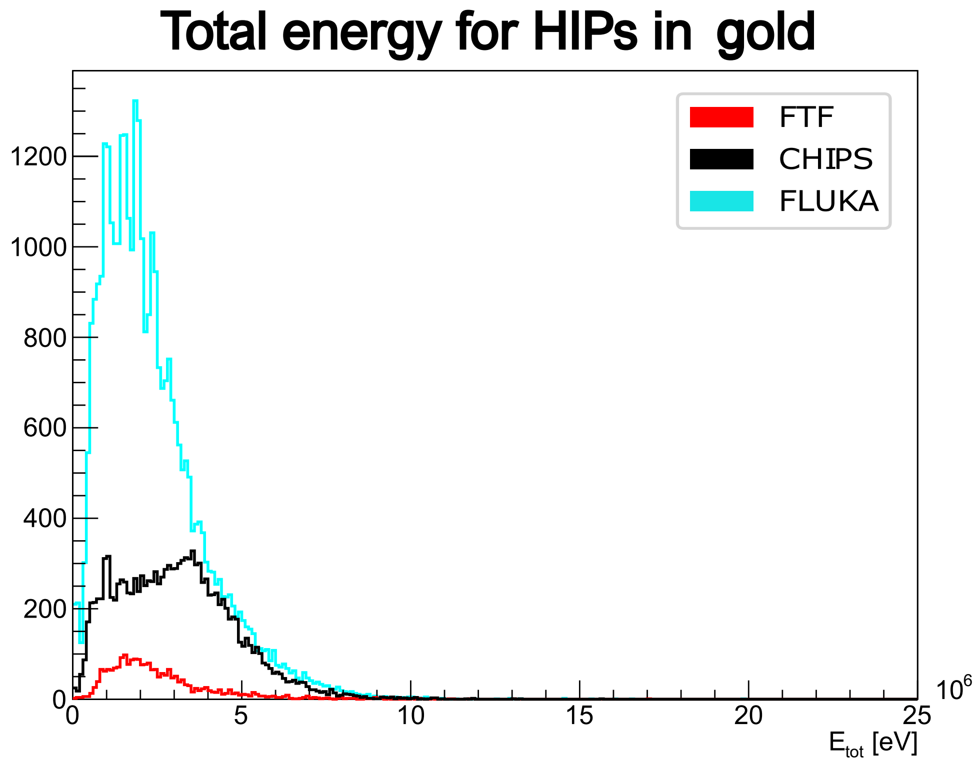

Figure 4.25: Distribution of the total energy deposited in HIPs clusters for all the events of annihilations on the gold target, for the Geant4 simulation with the FTF model (red), with the CHIPS model (black) and the FLUKA simulation (light blue).

4.5 Basic data unfolding

To conclude this chapter, I will discuss a final contribution I made to this project that goes beyond the implementation of simulations. In Section 1.1.1, I briefly mentioned the concept of data unfolding, which is a fundamental step in comparing experiments and is fully in line with the spirit of this project, which aims to improve the models used in simulations. Unfolding the data, i.e. recovering the information from the data, before these have been affected by detector effects such as acceptance or smearing[6], is essential if other research groups wish to compare their results with this measurement or even if the same ASACUSA collaboration needs to compare future measurements carried out with different setups. Unfolding the data will allow this data to be used for future analyses, taking this project beyond this single comparison.

---

[6] For definition of smearing go back to chapter 1.

Target	MC model	Quantity	N. of entries	mean	σ
Carbon	CHIPS	deposited E	31684	720 keV	107 keV
	FTF	deposited E	33946	354 keV	452 keV
	FLUKA	deposited E	30901	323 keV	362 keV
	CHIPS	Multiplicities	38286	0.82 MIP/ev	0.73 MIP/ev
	FTF	Multiplicities	38107	0.89 MIP/ev	0.70 MIP/ev
	FLUKA	Multiplicities	39063	0.79 MIP/ev	0.72 MIP/ev
Gold	CHIPS	deposited E	30099	474keV	746keV
	FTF	deposited E	32822	360keV	480keV
	FLUKA	deposited E	26019	331keV	374keV
	CHIPS	Multiplicities	30395	0.99 MIP/ev	0.65 MIP/ev
	FTF	Multiplicities	34878	0.94 MIP/ev	0.66 MIP/ev
	FLUKA	Multiplicities	40210	0.64 MIP/ev	0.69 MIP/ev
Molybdenum	CHIPS	deposited E	29111	487 keV	764 keV
	FTF	deposited E	33365	354 keV	456 keV
	FLUKA	deposited E	27157	326 keV	328 keV
	CHIPS	Multiplicities	39166	0.74 MIP/ev	0.70 MIP/ev
	FTF	Multiplicities	32691	1.02 MIP/ev	0.64 MIP/ev
	FLUKA	Multiplicities	40938	0.66 MIP/ev	0.70 MIP/ev

Table 4.2: Number of entries, mean and standard deviation for MIPs distributions of multiplicities per events and deposited energy for all the events, for all the target materials.

Based on this premise, I will now present some considerations regarding a simple yet effective correction for the hodoscope acceptance. The geometrical acceptance of a detector is defined as the area covered by the detector in which a particle can be detected. It is typically expressed as a fraction of the solid angle. Considering the limited geometrical acceptance of the hodoscope, it is important to acknowledge that some particles may pass through blind zones of the detector. This effect can cause an underestimation of the yield of some channels for the number of MIPs and an overestimation of the yield of other channels.

To provide a demonstration of this correction, I will refer to the data presented in [132]. Although these data must be considered preliminary, it is possible to show the effects of the hodoscope optimal, yet still partial, efficiency. An analysis of the final data will be presented in a future publication. For this correction, two assumptions will be made: (i) we assume that the annihilation products are emitted isotropically over the entire solid angle[7]. Furthermore, (ii) we assume that the maximum number of products observed is also the

---

[7] A more accurate correction should take into account the phase space of the various products, but this step would require a faithful model of all products, which at present is lacking.

Target	MC model	Quantity	N. of entries	mean	σ
Carbon	CHIPS	deposited E	33972	2161 keV	1655 keV
	FTF	deposited E	20619	1826 keV	1477 keV
	FLUKA	deposited E	28752	1983 keV	1596 keV
	CHIPS	Multiplicities	38286	0.88 HIP/ev	0.75 HIP/ev
	FTF	Multiplicities	38107	0.54 HIP/ev	0.61 HIP/ev
	FLUKA	Multiplicities	39063	0.73 HIP/ev	0.77 HIP/ev
Gold	CHIPS	deposited E	13388	3062 keV	1702 keV
	FTF	deposited E	2298	2554 keV	1631 keV
	FLUKA	deposited E	35048	2350 keV	1547 keV
	CHIPS	Multiplicities	30395	0.44 HIP/ev	0.76 HIP/ev
	FTF	Multiplicities	34878	0.06 HIP/ev	0.25 HIP/ev
	FLUKA	Multiplicities	40210	0.87 HIP/ev	1.02 HIP/ev
Molybdenum	CHIPS	deposited E	64577	3916 keV	1843 keV
	FTF	deposited E	5991	2739 keV	1652 keV
	FLUKA	deposited E	44408	2274 keV	1491 keV
	CHIPS	Multiplicities	39166	1.65 HIP/ev	1.54 HIP/ev
	FTF	Multiplicities	32691	0.18 HIP/ev	0.42 HIP/ev
	FLUKA	Multiplicities	40938	1.08 HIP/ev	1.15 HIP/ev

Table 4.3: Number of entries, mean and standard deviation for HIPs distributions of multiplicities per events and deposited energy for all the events, for all the target materials.

maximum number of products that can be produced by annihilation. The latter assumption should not impact the final result significantly, as the events with higher numbers of prongs have really low multiplicities, so their contribution to the correction should be small. Given these two assumptions, the correction for limited acceptance that I propose is quite simple.

We can consider the acceptance ϵ of the detector, 80% for the hodoscope, as the probability of being detected (*i.e.*, not considering the efficiency of the detector): every prong produced by the annihilation has a ϵ probability of being detected and a $(1 - \epsilon)$ probability of not being detected. If we consider the channel of maximum prongs per event, 6 detected products in the case of the data presented in [132], due to (ii), this channel cannot be populated by events where the annihilation produces a higher number of prongs that are within the acceptance of the detector. We can correct the number of prongs detected for this channel N_6, taking into account the probability of detecting all six prongs, $P_6 = \epsilon^6$:

$$N_6^c = \frac{N_6}{\epsilon^6}. \tag{4.7}$$

Moreover, of the six prongs, only a part can be detected by the hodoscope. These events will eventually be counted in another channel. For example, we can compute the probability of detecting 5 of 6 prongs: $P_{6,5} = 6\epsilon(1-\epsilon)^5$. Since we already computed the corrected number of events for the 6 prongs channel, we can use $P_{6,5}$ and N_6^c to estimate the number of events that we have to subtract from the 5 prongs channel and then correct this number for the probability of detecting 5 prongs, as we did for the 6 prongs channel. In this way, we obtain the correction for the 5 prongs channel:

$$N_5^c = \frac{N_5^*}{\epsilon^5} \quad \text{with} \quad N_5^* = 6N_6^c\epsilon(1-\epsilon)^5. \tag{4.8}$$

This reasoning can be applied to each channel, first taking into account all the contributions of the channels with a greater number of prongs and then correcting for the probability of detecting the number of prongs of that channel. More generally, this correction for the channel i can be written as:

$$N_i^c = \frac{N_i^*}{\epsilon^i} = \frac{1}{\epsilon^i}\left(N_i - \sum_{j=i+1}^{N_{\max}} N_j^c \binom{j}{i} \epsilon^{j-i}(1-\epsilon)^i \right). \tag{4.9}$$

Here, N_i^c is the number of events for channel i corrected by all contributions, N_i^* is the number corrected by the contributions from all channels except channel i, and $N_{\max}$ is the maximum number of prongs per event. In Figure 4.26, I show, for the three different targets, the multiplicities of the number of detected prongs and the multiplicities after correcting for detector acceptance applying Equation 4.9 in descendent order starting from the 6 prongs channel. As can be seen, the channel with the highest number of prongs is the three-prongs channel. This agrees with the average number of charged pions, as discussed in Section 2.3.4. It can also be noticed that the entire distribution for each of the targets shifts toward a higher number of prongs per event after the correction.

4.6 Summary

In this chapter, I have presented my contribution to the project aimed at characterizing the products of antiproton annihilations at rest. The chapter began with an introduction to the operation of semiconductor detectors, followed by a presentation of the measurement on which this project is based. I then described the digitization process I implemented in the simulations, both for those already performed in Geant4 with different models and for those developed by me with FLUKA. I explained the process chosen for digitization within the Allpix framework and how the Volcano effect, which partially distorts the signal of highly ionizing particles in Timepix3 chips, was addressed. This has now become a permanent option in the Allpix software for future analyses using the Timepix3.

Next, I discussed the simulation work carried out to reproduce the same data simulated with Geant4 using FLUKA software. I briefly presented the most significant differences observed in the results of the simulations, which will play a critical role in determining the model that best reproduces the measured data.

In conclusion, I applied a simple, yet essential unfolding procedure on the actual data to account for the effect of tracking detector acceptance. This correction is crucial for using the acquired data in the future to compare with other measurements made with different set-ups.

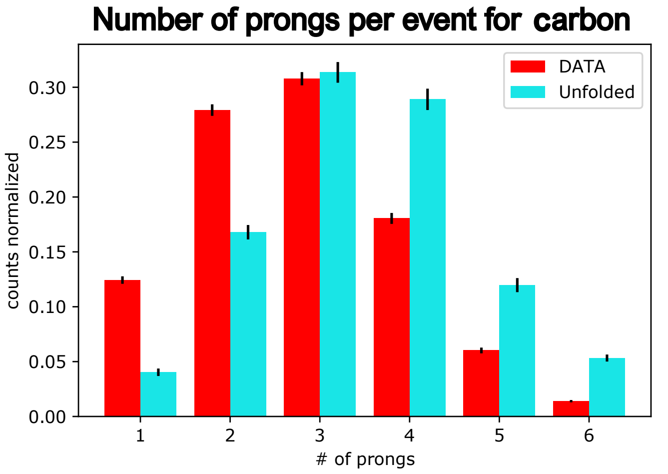

(a)

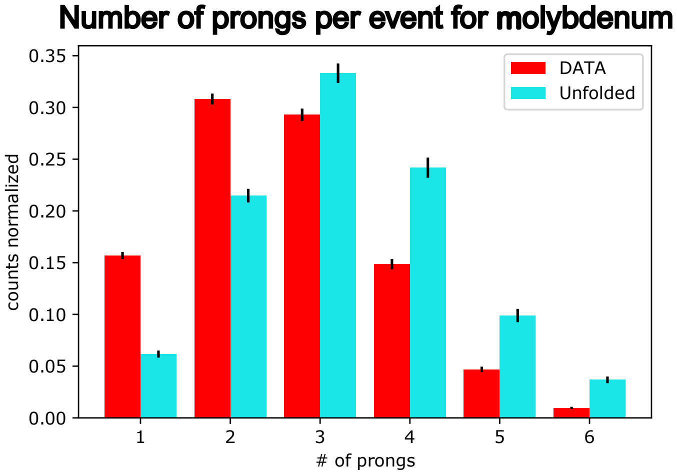

(b)

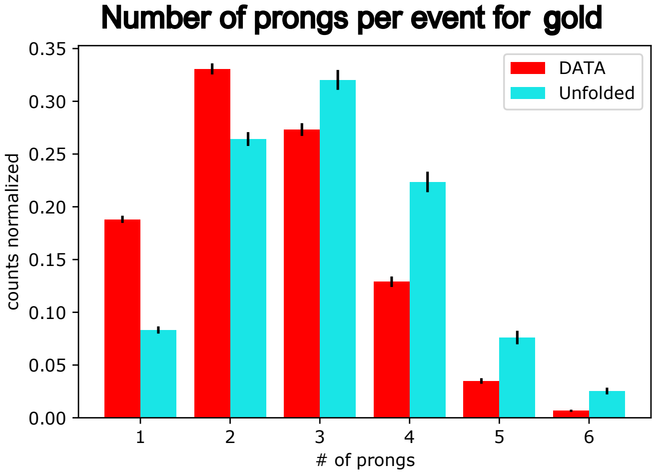

(c)

Figure 4.26: Normalized distribution of number of tracks reconstructed per event from the hodoscope signal (red) compared with the number of tracks reconstructed per event taking into account the effect of the limited acceptance of the hodoscope (light blue). See text for discussion on the unfolding procedure. (a) Number of tracks for $\bar{p}$ annihilations on carbon foil, (b) Number of tracks for $\bar{p}$ annihilations on molybdenum foil, (c) Number of tracks for $\bar{p}$ annihilations on gold foil.

Chapter 5

Annihilation vertex reconstruction with the ASACUSA tracking detector

In this chapter, I will describe the work that I carried out to upgrade the Detector for Annihilation Tracking Experiment (DANTE), which was built by the Fundamental Physics Group of the Information Engineering Department of Università degli Studi di Brescia and the Universtià dell'Insubria group.
This detector has been used in previous measurements made by the ASACUSA collaboration and is still used at present in the current data taking for the monitoring of the antiproton/antihydrogen annihilations in the CUSP trap.
The chapter will begin with an introduction about the detector itself, describing its previous operation and briefly summarizing the hardware and software upgrades that the group has performed in the last two years. This will provide context for my specific contribution to this project. The remainder of the chapter will be dedicated to describing the work I have done on the software for reconstructing the signal of antiproton/antihydrogen annihilation events.

5.1 DANTE detector

I introduced the DANTE detector in Chapter 3. This detector has been used by the ASACUSA collaboration for a long time to track the products of annihilation of antiproton and antihydrogen on different targets for various projects. In this section I describe how DANTE was used in the past and how it is currently used after the recent upgrade.

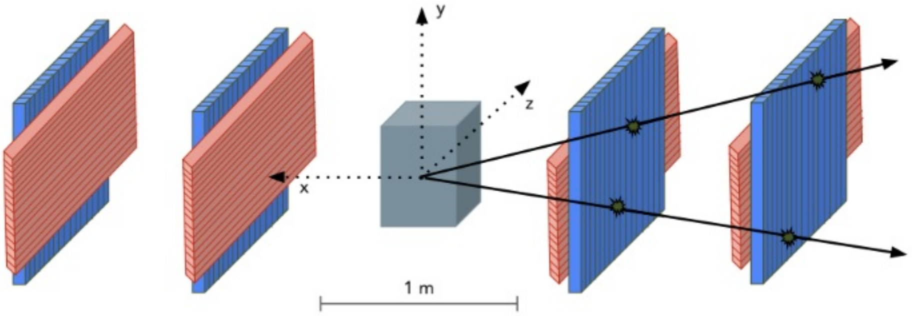

Figure 5.1: Panel configuration chosen for calibrating the plasma manipulations in the CUSP trap. This configuration is the one currently used. The centre of the CUSP trap (rapresented by the grey cube here) is taken as the centre of the reference system. The panels are coupled with the perpendicular bars to form a module (in blue the panels with vertical bars, in orange the panels with horizontal bars).

5.1.1 Old and new configuration

The ASACUSA collaboration has been at the forefront of experiments conducted at the CERN Antiproton Decelerator, studying various aspects of antimatter over the years. In several projects, the DANTE detector has made significant contributions in different ways. Its modular design allows for various configurations, making it an important tool for the ASACUSA collaboration.

A clear example of DANTE versatility is its use in the antihydrogen spectroscopy measurement described in Chapter 2. DANTE was employed to detect the formation of the first antihydrogen atoms in a CUSP trap, and it continued to be used during subsequent beam-time to monitor antiproton annihilations when the CUSP trap was upgraded to have a double cusp magnetic field. It played a crucial role in demonstrating the first $\bar{H}$ production in the cusp trap [93]. For these measurements, the configuration chosen for the panels is shown in Figure 5.1. The modules were positioned around the CUSP trap, with pairs of panels oriented along the X and Y directions (see Section 5.2.1 for details on the coordinate system). The detector operated in analog mode and self-triggered, recording an event every time a desired logic combination occurred (coincidence of hits in the inner planes). The maximum DAQ acquisition rate was approximately 1 kHz. In total, four modules were used: two close to the trap and two externally positioned to provide better coverage of the solid angle around the mixing region. In this setup, the vertex position was determined in 3D space with a resolution of approximately 4 cm in all directions or only for Z reconstruction

Another example was the measurement of the annihilation cross sections of antipro-

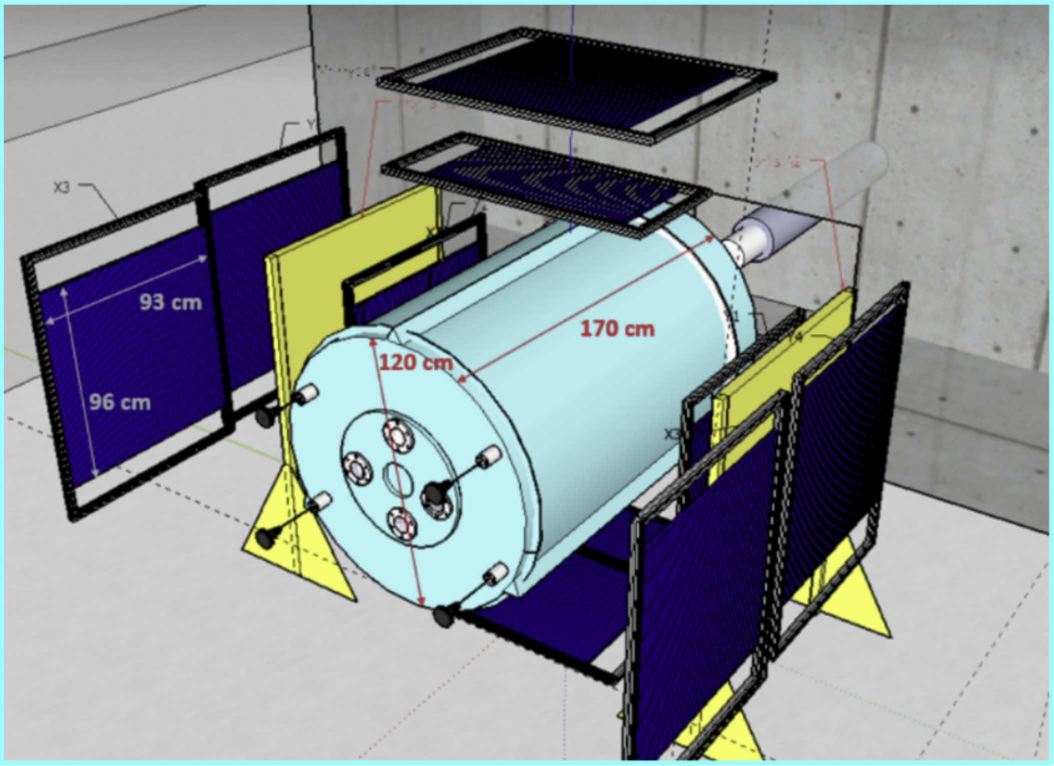

Figure 5.2: Alternative detector configuration used in a previous ASACUSA measurement for antiproton annihilation cross-section. The measurement involved a vessel in which a thin target was placed. The detector in this hodoscope configuration has all the panels that are used separately (*i.e.* not paired in a module configuration) and positioned on all sides to get the maximum coverage of the solid angle possible.

tons on different nuclei at different energies [133, 134]. In this experiment, DANTE also played a fundamental role in counting the annihilations. Ten separate panels were used and positioned around a stainless steel barrel where the targets were placed. The panels were displaced around the barrel to maximize the solid angle covered by the detector. Six panels were placed on the sides of the barrel, and four were placed on the top and bottom. A sketch of the geometry is shown in Figure 5.2. For this measurement, the digital mode was used as the acquisition scheme. Once a trigger was given, the DAQ ran continuously, and the shaped and discriminated PMT signals were sampled by a 300 MHz clock. The result was a 512-bit string of 0/1 corresponding to signals below/above the discriminator threshold. DANTE was used in this measurement to discriminate pions coming from annihilations on the target, from annihilation on other part of the chamber, based on the time of flight without tracking every track. This was a cross-section measurement and thus, only the number of pions was needed. Thanks to DANTE, the first annihilations of 130 keV antiprotons on C, Pd, and Pt thin targets were detected, and the limits of their cross-section were measured [133, 134, 135].

Regarding the current situation, DANTE is presently installed and operational within the ASACUSA experimental area, specifically around the CUSP trap. Following a two-year upgrade during which DANTE was temporarily relocated to Brescia, the detector was returned to CERN and commissioned in July 2022. Currently, various upgrades are being performed on all parts of the apparatus, and a new optimization procedure for the mixing parameters is planned. As a result, it has been decided to reposition DANTE around the CUSP trap, as in previous experiments, in order to help in this optimization process. The configuration of DANTE will remain unchanged, consisting of 8 panels in a 4 module setup, as depicted in the photograph in Figure 5.3.

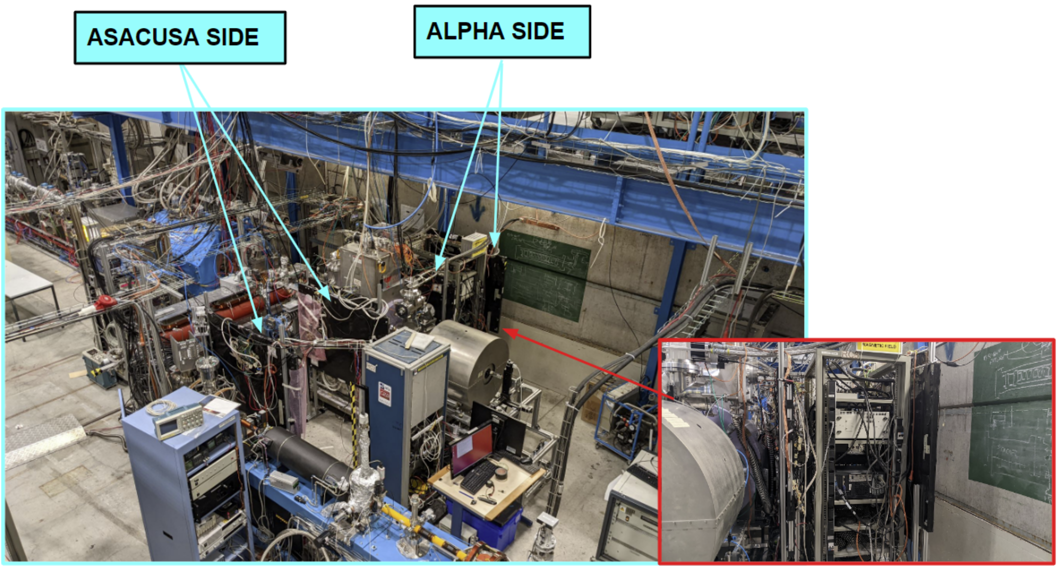

Figure 5.3: Photo of the ASACUSA experimental area. The 4 modules of DANTE detector are highlight with light blue arrows. They are divided in two pairs labeled as the ASACUSA side pairs and the ALPHA side pairs. On the right a detail of the two ALPHA side modules.

5.1.2 DANTE hardware upgrade

During the planned inspections for the last CERN long shutdown several damage and detector malfunctions were found. The major detriments were found on the internal structure of the detector which badly affected the optical coupling and the performance of the light readout.

We noticed that after several years of operations, the mechanical internal structure does not have anymore the required features in terms of precision and a degradation of the optical coupling of the light collection system was observed: several ones were discovered on the fibers were found completely broken or retracted. In several cases the scintillating bars had slid away from the PMTs with the effect of pulling their fiber out of the readout mask, or on the opposite direction pushing them and causing excessive curvature or cracks. The bars have shifted year after year, because during transport the mechanical joints started loosing and the internal adhesive parts started to fail. Because of the mechanical constraints and the limited fiber length, most of the damages could not be recovered keeping the same setup as the detector in terms of the readout part. The main goal of the upgrade was at least to return to the previous performance of the detector and hopefully improve it, yet keeping limited costs. As stated above the major damages of the detector was at the level of the fibers, in the part outside the bars. In order to avoid the replacement of the entire scintillating bar, it became necessary to reuse the same fiber and this was made possible by shortening them and replacing the light readout system. The solution found was to replace the multi-anode PMT used previously for the detection of the scintillating light coming from the fibers, with a series of SiPMss. They are compact and affordable. They can be operated in magnetic fields, which is important since the panels are placed near the superconducting magnet of the CUSP trap, and do not require high voltages. The chosen device is the 1×1 mm^2 active area ASD RGB-SiPMs provided by AdvanSiDc. Each device is covered with a transparent epoxy layer and located into a $2.02 \times 2.48 \times 1.30$ mm^3 SMD plastic package. The cell pitch is $40\,\mu$m for a total of 625 cells. The SiPMss model was chosen both for its good match with the green WLS fibers emission spectrum (the efficiency of the SiPMss is maximum at 550 nm) and for their radiation hardness which was tested for the ENUBET experiment.

Previously the analog signals coming from the multi-anode PMT were handled by a custom front-end board (FEB) based on the MAROC3 ASIC. Each FEB hosts also 2 Altera "Cyclone II" FPGAs and a 12 bit ADC. Each is channel of the MAROC3 ASIC 5.4 is pre-amplified trhough a common based amplifier followed by a set of current mirrors (8-bit resolution), then the output follows 2 different paths: the first one ("analog part") consists of a slow shaper, a sample-and-hold circuit and multiplexed with a 5 MHz clock whose output signal is digitized by the ADC; the second one ("digital part") consists of a fast shaper and a discriminator whose outputs are sampled with a 300 MHz clock by one of the FPGAs and used to obtain the time information of the recorded hits. The DAQ handles all the FEBs output signals by means of a VME based electronics system and can be operated either with an external trigger or in a self-triggering mode, depending on the application. In figure 5.4 a photo of the FEB and the detail of the MAROC3 chip are shown.

The choice of using SiPMs was also driven by the necessity of re-using the MAROC3-base FEB, with great savings in time, work and money. Obviously changing the readout

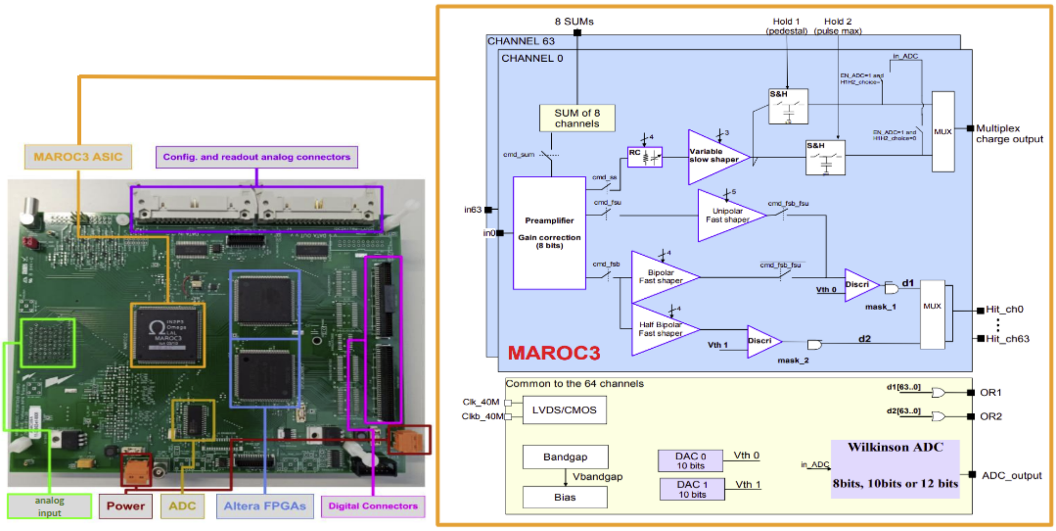

Figure 5.4: On the left photo of the FEB. The main components of the board are shown. On the right is a schematic of the MAROC3 chip. Image readjusted from [136].

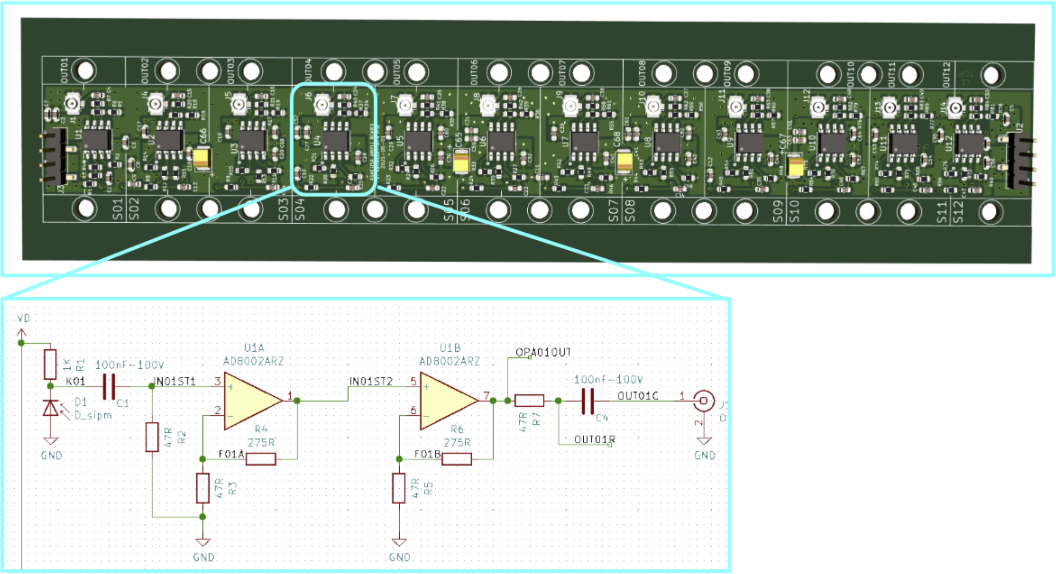

Figure 5.5: Above, photo of one of the 5 frontend tabs used in a panel for SiPMss. Below, a schematic of the signal amplification electronics of a single SiPMs. In white in the photo one can see the input connected to the SiPMs located on the other side of the board. The signal amplification is a two-step amplification. Image readjusted from [136].

scheme from one where many fibers are readout by a single device, to one where each fiber is connected to its own device implies a new read out board to accommodate the SiPMs and to adapt their signal to what is expected on the MAROC3 input stage designed for a multi-anode PMT. A new front-end board and an adaptor have been designed and they are shown in figure 5.5. For each board 12 SiPMs have been mounted on the dedicated pads and 5 boards, necessary to readout the 60[1] SiPMs of each panel , have been installed very close to the scintillating bars on the internal frame. In this way the problem of short fibers due to previous damages can be easily overcome. Each channel is equipped with one dual AD8002 current feedback amplifier and the necessary passive circuitry; moreover its footprint matches the bar cross section. All the parts of WLS fibers coming out from the bars have been shortened down to a $\approx 6 - 8$ cm length, polished and then glued onto a 3D printed connector whose counterpart is directly fixed to the new SiPMs front-end board. The SiPMs signals are brought to the FEB using $\approx$ 50 cm Hirose U.FL series thin coaxial cables and plugged into an adapter board designed to mimic the 8×8 array geometry of the old multi-anode PMT socket.

Several tests were performed to compare the behaviour of the ASIC after this changes of the analog input comparing it with the one described in the datasheet. For each channel two tests have been made:

- A scan of the hold parameter values. This allows to reconstruct the analog signal shape varying the time at which the signal is sampled with respect to the trigger.
- A scan of both the slow and fast shaper capacitors. For each value of the capacitor (the range was between 300 and 2100 fF) a hold parameter scan was made with a fixed gain.

Also the pre-amiplifiers were tested aiming at:

- Verify the linearity behaviour of the signal amplitude as a function of the gain.
- Study the response of the pre-amplifier for different gains and input signal magnitudes.

A final configuration of the MAROC3 parameters for the readout of the scintillating bar detector was chosen as follows:

- Since the SiPMs signals are already pre-amplified on the SiPMs frontend boards and to prevent saturation of the ADC on the MAROC3 board, we chose a low preamplifier gain.

---

[1] 54 for the two panels with 54 bars

Figure 5.6: Photo of the final frontend configuration of a detector panel. On the left a photo showing the frontend board which hosts the SiPMss, the two part of the coupler 3d-printed, one attached to the SWL fiber the other screwed on the board. Top right the back detail of the structural support designed to hold the frontend board and to keep the bars aligned. Bottom right, photo of the whole fronend panel part without the panel enclosure.

- The buffer and the slow shaper were set in the slowest configuration (*i.e.* with the highest capacitance, to have the longest shaping time). This configuration allowed us to hold the signal correctly, since the trigger logic takes time to generate the busy signal for the sample-and-hold circuit.

For what concerns the mechanical upgrade, in order to align the WLS fibers to the SiPMs active surface, an optical coupler was designed and moulded in resin using a Project 2500 Pro machine by 3D System8 that works with material jetting technology thus offering the required resolution. The ink-jet printing process uses piezo print-head technology to deposit photo-curable plastic resin droplets layer by layer and wax is used as support material. At the end the parts are immersed in mineral oil and undergo ultrasonic cleaning. The coupler, shown in figure 5.6 on the left, is composed by two parts: the first has a cylindrical shape with a circular hole to allow the glueing of the WLS fiber end cap, whereas the second one is a counterpart where the cylinder with the fiber has to be housed.

Furthermore, the internal mechanical supports were refurbished in order to keep the new SiPMs front-end boards at a fixed distance and position with respect to the scintillating bars so that the fiber curvature is minimized and no stress is applied when the detector is moved and vibrations propagate to all its parts. In figure 5.6 on the top right, a particular of the new framing system is shown.

5.1.3 DANTE software

A considerable amount of work has been made also for the upgrade and renovation of the software related to DANTE. From the data acquisition software , which was updated in its core, to the offline reconstruction sowftare which has been developed fresh new. Having the opportunity to restructure the entire detector management code, some guidelines were followed:

- first and foremost, the code had to be as transparent and shareable as possible. This was not only to accommodate the entire collaboration, but also because it was developed by several people in parallel.
- second, the code had to reflect DANTE flexibility to adapt to different situations

To meet the first requirement, the Git version control software was used for the offline reconstruction and a CERN GitLab repository maintained to make it. As for flexibility, this guided some general structure choices. A case in point is for example the sharing of detector geometry. Whether it is the code dedicated to data pre-processing, or simulation or signal reconstruction, since these have to refer to the same detector, we decided to dedicate a meta-data file for the description of the geometry. This is a yaml file, a vastly used format for the sharing of meta-data. Each part of the code refers to this file depending on the specific need. For the sake of continuity along the whole code, certain conventions have also been decided. I will use this also in this thesis in order to present the work on the reconstruction software. In particular, the geometry reference system is always taken with the Z axis along the direction of the antiproton beam, with the unit vector pointing down stream, the Y axis pointing up, and the X axis following the right hand rule. The center is taken as the center of the sector that DANTE is analyzing, in our case the CUSP trap. The numbering of the channels or bars always follows a convention, from 0 to 60 following the direction of the reference coordinate, so the panels, which are numbered from 0 to 7 following the direction of the X axis. The detector is divided in two main part that are the four panels for each side of the CUSP trap. An inherited convention used also in the following is to call one of the side the ASACUSA side and the other the ALPHA side[2]. Having these conventions allows us to identify also a common structure between real data

---

[2] This is due to the fact that the four panel on the ALPHA side are closer to the ALPHA experimental area, whereas the other four are in the center of the ASACUSA experimental area.

and simulations for the data to analyse. In this way, the reconstruction code can easily be used on both real and simulated data. Obviously the general amount of information can change from simulation to real data, but the essential features are still the same. The output data are organized in the form of ROOT files using a TTree class object where each entry corresponds to an event triggered by the detector DAQ (an antiproton annihilation in the simulation case). For each event, all the bars are reported and if a hit occurs, the line corresponding to the bar hit will have the energy deposited with that hit. The main features that characterize an event are the number of the panels, the number of the bars of that panel that have been hit and the energy deposited in that hit or ADC signal depending if they are real data or simulated data. A digitization of simulated energy depositions has not been implemented yet. Only after that and once a fine calibration of the detector will be done, it will be possible to convert energy deposited in ADC signal and vice versa. At the moment this is missing and the two values have to be considered separately. The data in the ROOT file include supplementary information about timing (in the case of experimental data) or trackID, momenta, and so on (simulated data).

Below we will give some information regarding the dedicated data pre-processing and simulation software. We will then devote the next section to the tracks reconstruction software, which was my major contribution. In appendix B.1 a sketched structure of the directory and more information about the codes can be found.

Pre-processing

The data pre-processing software is necessary in order to move on to any subsequent data analysis steps. See the figure 5.7 for a diagram of the steps performed during the pre-processing phase. consists in transforming the original raw data format (HBOOK) to the ROOT one. In this step, what has been established as the general structure of the processed data we described above, is created. In order to do this transcription a mapping of the incoming signals is performed. This is needed because each signal coming from the SiPMss, and adapted with the dedicated board is processed by the VME boards. These process two panel each and give an array of the 120 channels of the two panels. In this step also a threshold is applied to the data, based on a pedestal calibration which is made routinely to estimate the background signal of each channel and the corresponding sigma to noise ratio. The remaining steps are needed in order to store the data. Small ROOT files are created to facilitate the reconstruction. After the reconstruction is applied, multiple files are merged in single bigger files for the long term storage. All these steps are performed by a virtual machine in the CERN OpenStack framework so that remote control is always possible and the output data are directly saved in the CERN EOS storage system reserved for the ASACUSA experiment.

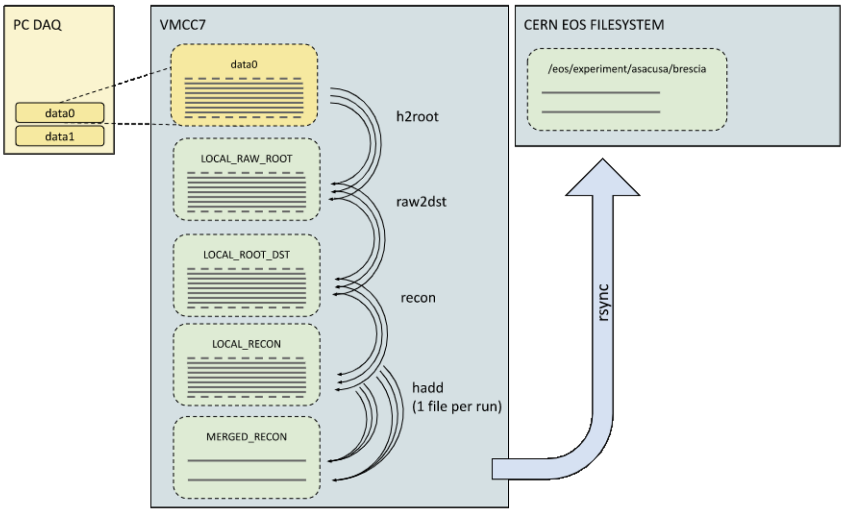

Figure 5.7: Diagram of the steps performed in the pre-processing phase: they consist in grouping and manipulating the raw data to obtain the format used for data analysis (see the text). In addition, pre-processing also takes care of data storage for offline analysis and online signal reconstruction.

Simulation

The simulation software has been developed using the Geant4 toolkit. These are the first simulations in Geant4 for DANTE [3]. It allows a construction of the DANTE geometry in different configuration, using the geometry configuration file as a reference for the panel position. Also a simplified version of the double-CUSP trap has been implemented in the geometry of the simulation. This is needed to simulate the effect of the CUSP material on the detector performance. At the moment only the geometry of the CUSP trap is implemented in the simulation, since as we said, for the next beam time it has be chosen to use DANTE to help in the parameters optimization for the mixing process. If later DANTE is needed in other areas of the experiment, other parts of the line can be added into the simulation geometry. In figure 5.8 a render of the simulation geometry is shown.

Despite the fact that a proper digitization is not yet in place, the output of the simulation has been implemented in such a way to reproduce the DANTE signal in a simplified way. The ROOT file which constitutes the main output of the simulation follows the structure described above. It has been chosen that the particle associated to the hit is the first to enter that bar and all the energy depositions simulated are integrated in order to have a single value per hit. The simulation software as it is, can already be used, however some features that can improve the simulations are still under development. A feature which is

---

[3] Previously Geant3 was used.

still missing in the simulation software is a map of the magnetic field of the CUSP trap. The magnetic field it is fairly localised due to the CUSP shielding, but it could bend the first part of the particle trajectories. This should however be a second order effect, so it can be overlooked in a first approach. Also a detailed implementation of the time information is currently under development.

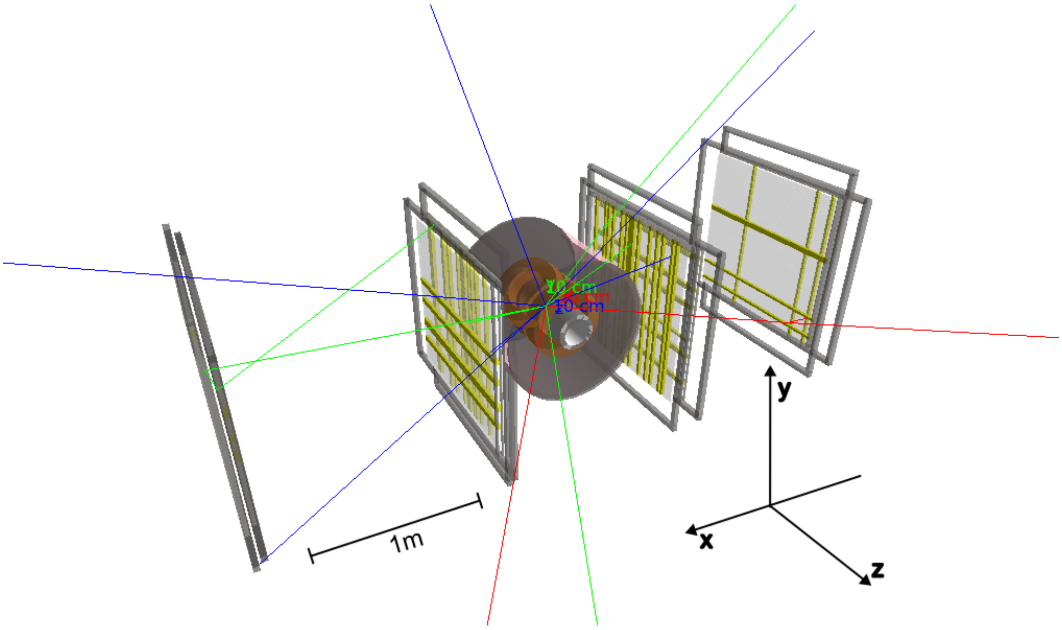

Figure 5.8: 3d rendering of the full geometry implemented in Geant4 simulations. This is the configuration DANTE has at the moment in the experimental area. The distances are the ones measured at the moment of installation of the detector. The materials of the CUSP trap have been reproduced only for the main part around the trap: aluminium for the cold bore, stainless steel for the shield and copper for the magnet. The lines are the product of an annihilation event, green lines are neutral particles, blue lines are negative particles and red lines positive particles.

Thanks to the simulation a first assessment of the reconstruction has been possible.

5.2 Reconstruction of events

Now that a presentation of the whole upgrade project has been made, I will focus on my main contribution, which consists in the development and testing of the signal reconstruction software. I will proceed as follows. I will discuss the choices made in implementing the signal reconstruction. Then I will discuss some features of the detector and I will analyse results achieved with the simulation code in Geant4 presented above. After that I will discuss some tests of the reconstruction made by means of the simulation and I will end showing the reconstruction software in action with real data.

5.2.1 Pattern recognition and vertex reconstruction

General considerations

Lets start the discussion on the signal reconstruction with a few consideration. Firstly, we are mainly interested in pion tracks. This is because most HIPs are expected to stop within the material of the CUSP and therefore we expect most of the signal-forming particles to be MIPs. As reported in section 2.3.4 these charged pions should be generated with an average energy of $\approx\ 236\,\mathrm{MeV}$ of energy each. Secondly, we expect a contribution from neutral pions that convert into two photons almost instantaneously which in turn convert into e+e- pairs in the high Z material (magnet, electrodes) surrounding the beam pipe.

Also, since the magnetic field has not been added to the simulation yet, I am going to consider the tracks as straight lines. This is a good approximation, since, as I said, I expect the magnetic field to be a second order correction, due to the fact that shielding and its configuration limit its effect to a small area. The main effect should be in fact the scattering inside the cusp material that can change the trajectory of particles by a considerable angle.

The goal of the reconstruction is to give insight into the location of the plasma and the amount of trapped antiprotons in the CUSP trap. These two pieces of information can greatly aid the optimization of the procedure for trapping the various plasmas in the CUSP and the mixing procedure that will be used to create the antihydrogen.

The procedure

The process of reconstructing a signal has to follow three main steps: the pattern recognition, the track reconstruction and finally the vertex reconstruction. For each of these steps the approach, depends on the geometry of the detector.

One important consideration pertains to the differences between the current DANTE configuration and other possible configurations that may be chosen in the future. Presently, the set of coordinates for each hit is determined by the position in space of the vertical and horizontal bars through which a particle passes. As a result, for each hit, we obtain both Z and Y coordinates in the reference system described in the preceding section. Moreover, the position of the panel determines a fixed X position for each hit. Since we have a total of eight panels, each track is identified by two hits for each direction, which amounts to, at most, a pair of three-dimensional points for every track. However, if, for instance, we dispense with the information pertaining to the Y direction by positioning all panels with vertical bars, a single track could lead to up to four hits. Such a configuration, in turn, would impact not only the approach to track reconstruction, but also the final vertex reconstruction.

In such conditions we have no information that allows us to choose one track over another. On the other hand, we do not need a sophisticated algorithm in order to identify a pattern among the several hits that compose a track, since two point define only one straight line. Therefore, the choice I made was to opt for a reconstruction that forgoes looking for the true traces that produce the configuration of hits per observed event. Instead the procedure will reconstruct all possible tracks. In this way I am keeping all the information contained in the configuration of hits, *i.e.* also the one given by secondaries which does not come directly from the annihilation event. These translates in a procedure that does not distinguish between pattern recognition and fitting track. As consequence, the distinction between the first step and the vertex finding step becomes less marked. This choice will be clear in a moment.

For what concerns the track reconstruction, the first thing one can think of is to reconstruct all the possible tracks given by the three-dimensional points. Since we start from one-dimensional[4] information, operationally the most logical procedure to follow is to associate each position $X - Z$ and $X - Y$ of the same module, then associate each of these points with points of the other module in the same side, so as to obtain the pairs of points that define the tracks. However, I want to point out, although it goes fairly obvious, how this procedure is entirely commutative and the same combination can be obtained by first associating the positions along one direction, $X - Z$ for example, of the two respective modules and then associating all pairs of positions with those reconstructed for the Y direction. In the development of the software, I chose this second path, since, as I show below, the information obtained already from the first of the two associations is sufficient for the goal of reconstruction.

If one wants to reconstruct all possible tracks, a factor to be taken into account is that of ghost tracks. Tracks produced by the pattern recognition algorithm that do not reconstruct any true particle are called ghosts. A simple example to give an idea of what can happen with DANTE is to think of two tracks interacting with the first 2 panels on the same side with respect to the CUSP trap. For each track we will have 2 bars (a horizontal one and a vertical one) identifying 2 Y, Z points. However, these 4 bars will intersect at two other points, giving two other positions, the so-called ghost hits, which do not belong to any trace. This can happen on both modules, causing 4 more Y, Z hits and resulting in a total of 16 tracks for a 2 tracks event.

For what concerns the vertex reconstruction procedure, the configuration chosen for the DANTE geometry for this beam time allows theoretically for a 3D reconstruction. However,

---

[4] The information is two-dimensional, but since the X position is fixed and determined by the location of the panels I am referring only on the two directions we are interested.

without an information on the X axis given by panels positioned on top and bottom of the CUSP trap, the resolutions of the reconstruction on this direction is way lower in comparison with the dimensions of the geometry MRE of the CUSP trap. Once the tracks were reconstructed, I therefore chose to estimate the Z and Y positions on the beam axis, thus imposing $X = 0$ as the X position of the vertices. We can make this estimate in several ways. For example, (i) we can directly consider all intercepts with the plane $\hat{z}\hat{y}$. (ii) We can take the midpoint of these points, to find a single vertex per event. (iii) Or finally we can group the various intercepts into groups of neighboring intercepts and then find a midpoint for each subgroup of intercepts, but as we will see, this last approach is useful only if the number of ghost is high, otherwise it is equivalent to approach (ii).

To set the reconstruction procedure, we need to identify the set of parameters that we want to use to describe our tracks so to associate them to the set of coordinates that our detector is providing. The simplest and most straightforward choice as for the parameters to characterize the track in the feature space is to stick with an Euclidean choice of the parameters. A straight line in the Euclidean space needs at least 6 parameters to be fully identified. The most common choice is to take a three-dimensional point and a unit vector. In our case, since we are interested in reconstructing the intercepts of the tracks on the $\hat{z}\hat{y}$ plane, I chose these intercepts as the point, so as to facilitate computational procedures. In particular, the combinatorial problem of computing all possibile tracks was divided on the two planes $\hat{x}\hat{y}$ and $\hat{x}\hat{z}$. For each plane, a two-dimensional line identified by the slope with respect to the X axis ϕ_i and the intercept i_0, with $i = z, y$.

Before moving on to the analysis of the reconstruction, I must point out two things. The first is that although I have presented the problem by always evaluating it as it occurs, thus as a problem in 3 dimensions, this can be addressed separately on each of them. As I mentioned earlier, the combinatorial part of selecting the various tracks is commutative, and so we can first select the combinations for single directions between the two panels. For these we can find the intercepts to evaluate the vertices. Then we can choose one of the three approaches (i), (ii), (iii). In doing so we lose no information except the false information given by the ghost hits that are formed by combining hits from one direction with the other. We could say indeed that the information for the Y and Z axis is *orthogonal* (*i.e.* it does not affect the other). This is very easy to see, since we have to reconstruct straight lines. By writing the equation of a line in parametric form

$$\begin{cases} x = & x_0 + mt \\ y = & y_0 + lt \\ z = & z_0 + nt \end{cases}$$

where (x_0, y_0, z_0) is the intercept with the $\hat{z}\hat{y}$ plane and (m, l, n) the vector defining the direction of the trace. It is clear that the intercept positions on $\hat{z}\hat{y}$ are given by the combinations on the individual directions using for Z the first and third equation and for Y the first and the second. This is only valid since we are reconstructing straight line, with a curve, the parametric equation wouldn't be linear and the same reasoning wouldn't be valid. We will show this also during the simulation analysis. A clear example can be seen in in the reconstructed event shown in figure 5.9. As can be seen the combinatorial steps combining lines on the $\hat{x}\hat{z}$ plane and on the $\hat{x}\hat{y}$ plane increase dramatically the number of line, but it does not add any information about the position of the intercepts on the $\hat{z}\hat{y}$ plane. I therefore expect that the final step of combining the two information on the individual directions Z and Y will bring no improvement, except a drastic increase in ghosts. For this reason, in the next two sections I will concentrate on evaluating the reconstruction process on separately on both directions. The other comment regards some option that I implemented in the recon-

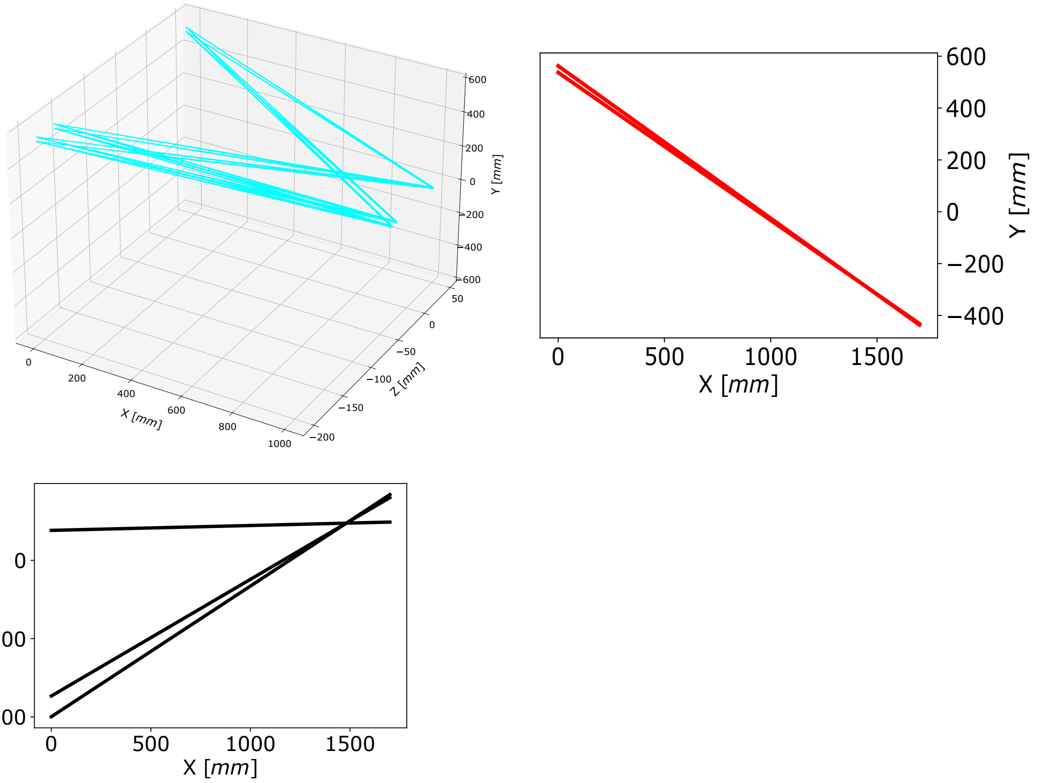

Figure 5.9: example of reconstructed event. Top right Y component of the tracks, reconstructed with the information given by the horizontal bars. Bottom left, Z component of the tracks. Left top, 3d tracks reconstructed by combining the Y and Z components. In this events 3 vertical and 2 horizontal bars on the panel closer to the CUSP and 1 vertical and 1 horizontal bar on the farthest one have been hit. The Z information on the $\hat{z}\hat{y}$ plane given by the Z component of the tracks is just replicated by combining the two components.

struction software. To partially address the ghosts problem, a fiducial area can be defined to cut all reconstructed traces with a parameter z_0 or a parameter y_0 outside that area. This represents the fact that all the tracks have to come from the CUSP. Another option that I implemented is that of considering adjacent bars as a single hit. To do that a clustering algorithm[5] is applied before the reconstruction phase. The position that is considered once several adjacent bars are grouped together is to take the midpoint given by the position of those bars. This was done because, given the width and thickness of the bars, it is possible for a single trace to deposit energy in more than one bar per panel or for electrons ionised by the particle generating the trace to deposit energy in adjacent bars. It is therefore interesting to see whether taking this possibility into account helps to increase the performance of the reconstruction.

5.2.2 DANTE simulations

Monte Carlo simulations can give us an idea of the problem we are going to face, so that we can choose the most appropriate approach. In this particular case they can give us two important pieces of information:

- Information regarding the acceptance of the detector and thus the amount of tracks we need to find and calculate. This can help, if the simulation are well calibrated on the experiment, during the data taking in establish the amount of trapped antiprotons depending on the number of reconstructed vertices.
- Information about the energy of the depositions. This information must be used, together with the signal thresholds used for the real data acquisition, to set the energy cuts for the hits to be used to reconstruct the tracks.

Geometrical acceptance
In order to assess the signal reconstruction problem the first thing we can do, even before using Monte Carlo transport software however, is to geometrically estimate the acceptance of the detector. To do this, we can calculate the solid angle covered by each panel and estimate, given the positions of the various panels, the percentage of the solid angle covered by the panels as a function of the initial position of the particles exiting the annihilation. In figure 5.10 is shown, for each side of the CUSP trap the solid angle fraction covered by the intersection of both modules (*i.e.* the chance that one particle hits both modules) depending on the starting point on the Z axis is showed. These fractions were

---

[5] For both cases where a clustering algorithm was applied, the *AgglomerativeClustering* algorithm of the Cluster SKlearn library was used.

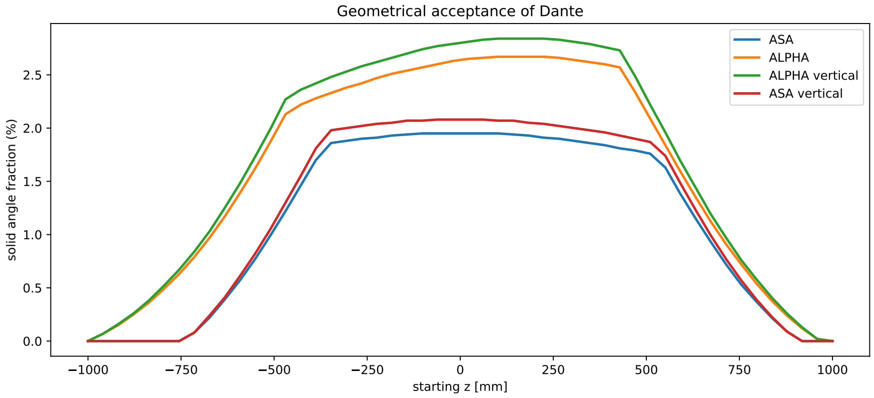

Figure 5.10: Percentage of solid angle covered by the panels of the detector seen by a particle depending on the starting point on the Z axis. In orange (for the ALPHA side) and blue (ASACUSA side) the solid angle covered by the union of both panels with vertical bars and panel with horizontal bars. In red (ASACUSA side) and green (ALPHA side) the solid angle covered by only the two panels with vertical bars.

calculated using the actual panel positions measured during the setup of the detector in the experimental area, where 0 refers to the centre of the outer shell of the CUSP trap. As can be seen, the fraction of the solid angle covered by both modules is about 2%. This fraction is roughly constant along more than one metre along the Z-axis. It should be noted that the trap is positioned between -400 and $+110$ mm in this graph, while the output of the entire CUSP structure is approximately at $+500$. I do not expect major problems with reconstructions at the edge of acceptance. The ALPHA side covers a slightly larger solid angle because, due to space constraints, the two outermost panels could not be placed as far apart as those on the ASACUSA side. We therefore expect to reconstruct more traces for the ALPHA side. In figure 5.11 we also add the solid angle fraction for the single modules for the ASACUSA side. As can been seen from this plot, we will expect a lot more hit on the first panel, for tracks that will not interact with the second one. This should increase the number of reconstructed ghost traces, however, these should be mostly discarded by fiducial cuts, since hits given by traces that fall within the acceptance of only the first module should give divergent[6] ghost traces.

Simulations

After this first consideration we can then use the simulation software presented in section 5.1.3, to test the reconstruction procedure and estimate its performance. To make this assessment, we simulated 120 K antiprotons at rest inside a hydrogen target that was placed

---

[6] With divergent here I mean not pointing toward the CUSP trap region.

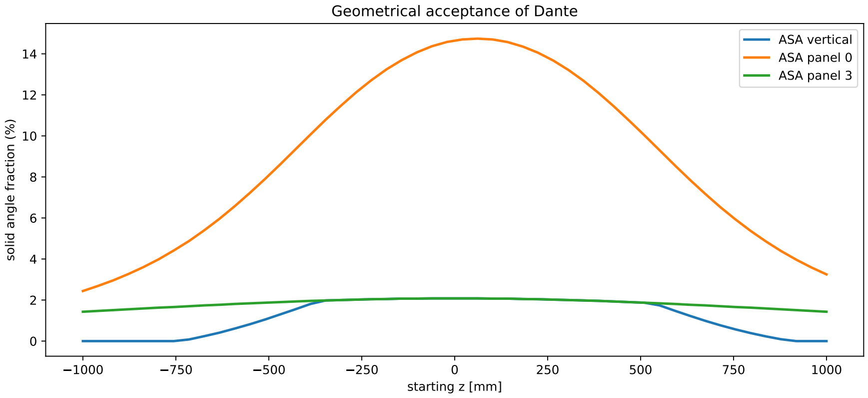

Figure 5.11: Percentage of solid angle covered by the panels of the detector seen by a particle depending on the starting point on the Z axis. In blue the angle covered by the two panel with vertical bars. In orange the angle covered only by the panel nearest to the CUSP trap, in green the angle covered by the farthest panel.

in $(0, 0, 0)$ so as to have a fixed point for annihilations. The origin of the axis was also the center of the CUSP trap. The positions used for the detector were the ones took when the detector was installed. This simulation was also repeated by omitting the CUSP material to evaluate the effect given by the material. Before applying the reconstruction software to the simulated data, we can analyze these two simulations to derive useful information.

First let's consider the simulation with the CUSP material and let's make some considerations about the energy distribution. Figure 5.12 shows the probability density distribution of deposited energy of all the hits on all the panels for all simulated events for the case with the CUSP trap material. In the simulation there is no cutoff on these depositions and as can be seen from the plot there is a peak of very low energy depositions. Three cuts applied to the deposited energy per hit are marked in black. I expect the last of these cuts to be the most significant. This is because, if we consider pions, we expect these to lose an average of 3 MeV of energy passing perpendicularly through a bar. This is a crude estimate made knowing the stopping power of the plastic scintillator: if we consider the average kinetic energy of the pions emitted by annihilation (236 MeV) and the fact that they have to pass through roughly 1.9 cm of the plastic material of the bars which has an average density of $1.28\,\frac{\mathrm{g}}{\mathrm{cm}^3}$ we can see from figure 5.13[7] that the pions should released on average 2 MeV per centimeter, thus 3.5 MeV passing through the entire width of the bar. I chose to look also at the other two cuts in order to study the behavior of reconstruction as noise increases, but once a fine calibration of the detector is done, they should no longer be relevant. In figure

---

[7] Considering the curve for carbon material, since that the plastic are mainly composed by carbon and hydrogen

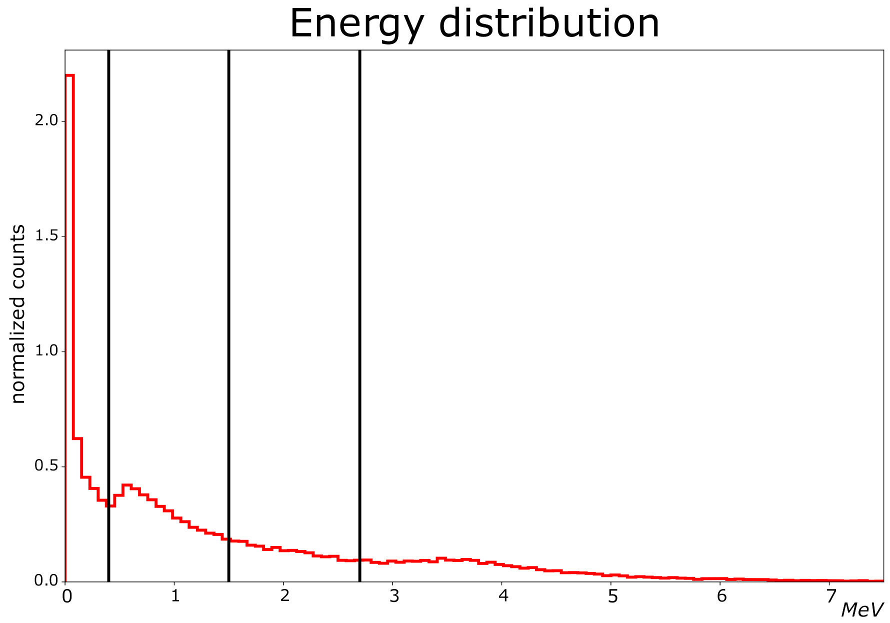

Figure 5.12: Probability density distribution of deposited energy of all the hits registered by the detector in all the events. In black the 3 values of the cuts used in the analysis. The first narrow peak is not of interest since it corresponds to tiny energy deposits that cannot be seen by the detector. The small broad peak at 3.5 MeV is the one corresponding to the MIPs in plastic scintillators (see the text). The cut in the middle has been chosen to see the behaviour of the reconstruction procedure depending on the increase of the background signal.

5.14, I have also reported four histograms that show well the effect of these energy cuts. The first shows the number of total hits per particle type as the energy cut increases. As can be seen, as the energy cutoff increases the hits that decrease most in number are those associated with electron and gamma particles. With the last cutoff we see that the number of hits associated with gamma and electrons is comparable to that of pions. The other three histograms, on the other hand, show the positions on the X axis, associated with the point of creation of the particles to which the hits are associated. I reported only the particles with the highest multiplicities besides pions, *i.e.* electron, gammas and protons. It is interesting to note that most of the particles that generate a signal in the bars (except for pions) are created not at $X = 0$, but on the walls of the various layers forming the CUSP trap. This is one of the reasons why the reconstruction procedure does not focus on an exact reconstruction of the annihilation vertex. Most of the particles created in the annihilation process are absorbed inside the CUSP material producing secondary particles. Since these secondaries are created in collisions in which the centre of mass has a very pronounced momentum component (*i.e.* as in a fixed target experiment, the atoms of the CUSP material do not have a relevant momentum), they should be created mostly in the same direction of the primary particle coming from the annihilation. Thus the information of the annihilation vertex should still be in the hits associated to these particles. Moreover we can notice that as the value of the energy cut increases, it is not only photons and electrons that fall dramatically in number, but in particular those originated between ≈ -500 cm and $\approx +500$ cm . This region corresponds to the panels closest to the CUSP, so this is all electron background that creates ghost hits. We are evaluating the reconstruction based on two factors: efficiency and resolution. The analysis is differentiated by both sides of the detector (ALPHA and ASACUSA), in two directions (Z and Y) and with or without the CUSP trap material (Y/N). Table 5.1 and 5.2 shows the results of different simulations, where we can determine

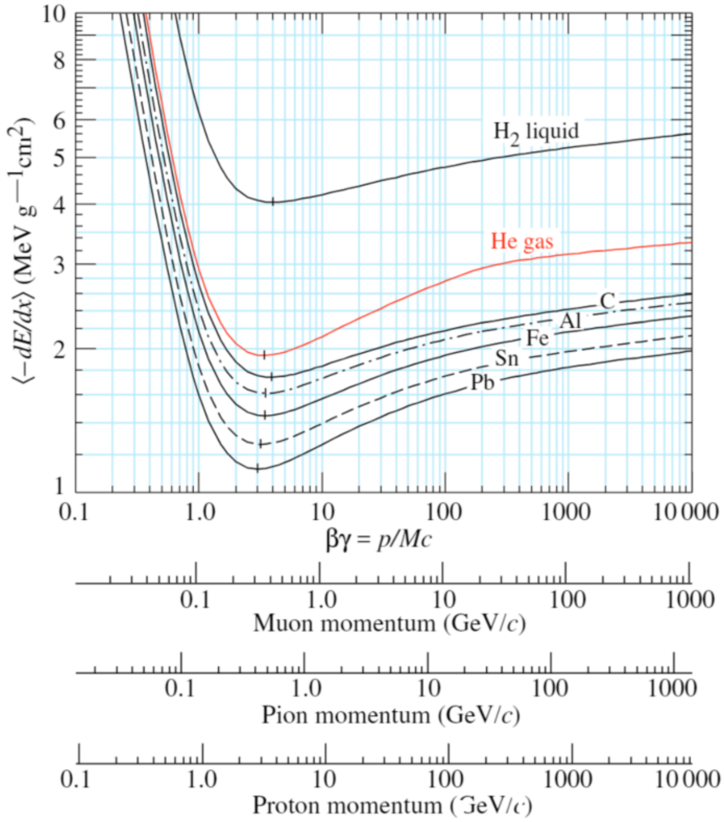

Figure 5.13: Stopping power for different materials depending on the momentum of different particles. Image from [137].

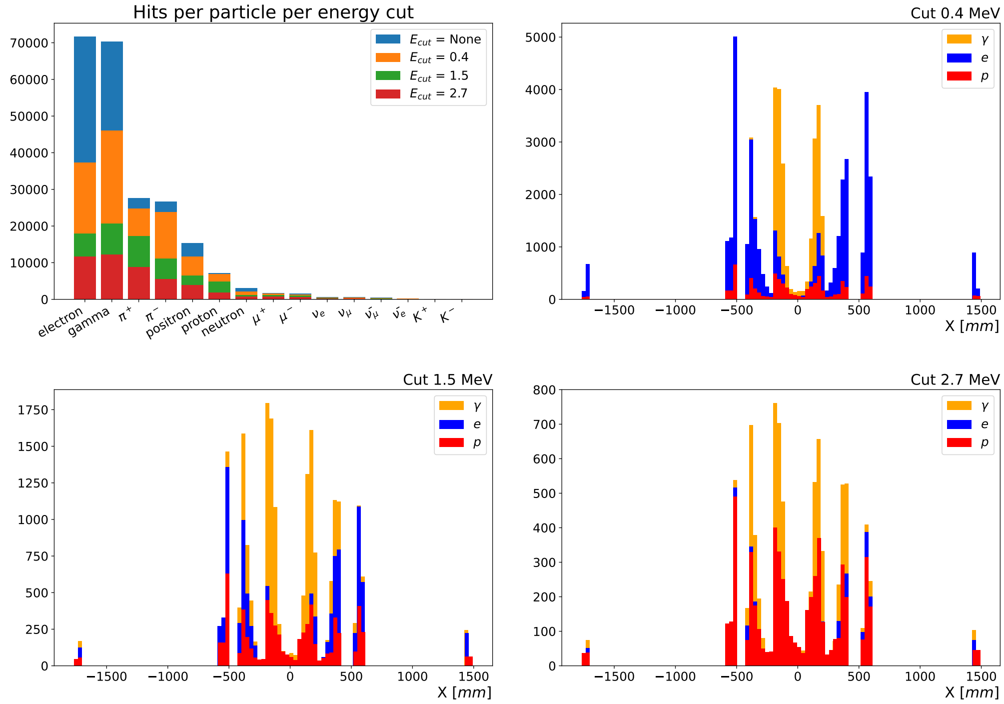

Figure 5.14: Background composition depending on the energy applied cut. Top left, overlapped bar diagrams showing the number of total hits registered in all the panels for all the events associated to a certain particle. In blue no cut was applied, in orange, green and red a cut of 0.4, 1.5 and 2.7 MeV was applied respectively. Top right and bottom left and right, X positions of the creation point of the particles that hit the detector. Only the three particles that form the majority of the hits other than pions are reported: proton (p), gamma and electron (e).

the number of events that can be reconstructed by counting the number of events that have at least one hit on the same side of the CUSP trap in a pair of panels with either vertical bars (table 5.1) or horizontal bars (table 5.2). We also count the total number of tracks in these events, which are selected based on the different ID tracks provided by the simulation. Finally, we determine the number of tracks that should be reconstructed, which are defined as all tracks that deposit energy in a pair of panels with the bar oriented on the same direction on the same side of the CUSP, referred to as *real tracks*. Out of the 120000 events, not all of them result in energy being deposited into the detector. In the case with the CUSP trap (Y in the "Cusp" column), only 50% of the events have at least one hit. Of these, only 5% of the events can be reconstructed. The penultimate column shows the percentage of events that can be reconstructed for each case. As the energy cuts increase, the percentage decreases.

However, the last column, which shows the percentage of real tracks compared to the total energy-depositing tracks, indicates that the percentage increases with the increase in energy cuts. This confirms that the selected hits correspond to real tracks.

Cusp	Side	Energy cut	# Ev	# Ev. rec.	# Track	# Real	ϵ_e	ϵ_v
N	Alpha	0.4	107983	3544	9449	5474	6.67	57.93
N	Alpha	1.5	107983	5119	5672	3727	4.74	65.71
N	Alpha	2.7	107983	3155	2989	2268	2.92	75.88
N	Asa	0.4	107983	5163	6510	3823	4.78	58.73
N	Asa	1.5	107983	3756	4024	2692	3.48	66.90
N	Asa	2.7	107983	2073	1018	1609	2.11	77.62
Y	Asa	0.4	60419	2110	1428	992	3.49	69.47
Y	Asa	1.5	60419	1147	796	640	1.90	80.40
Y	Asa	2.7	60419	622	443	397	1.03	89.62
Y	Alpha	0.4	60419	2669	1998	1396	4.42	69.87
Y	Alpha	1.5	60419	1530	1100	913	2.53	83.00
Y	Alpha	2.7	60419	806	626	563	1.33	89.94

Table 5.1: Analysis of the tracks detected by DANTE for the Z direction. First column indicate if the simulation has or not the CUSP material. Second column, side of the panel recostructing the tracks. Third column, energy cut selected. Fourth column, number of events which present at least one hit in the detector (considering both sides). Fifth column, number of events having at least one hit in the inner and outer panels. Sixth column, number of tracks for these events. Seventh column, number of tracks among the one of the previous selection, that deposited energy in both the inner and outer panel. Eighth column, $\frac{N_{rec.}}{N_{Ev.}}$ in percentage. Ninth column, $\frac{N_{real}}{N_track}$ in percentage.

With regard to signal resolution, it is possible to use the information given by the simulation to estimate the *maximum resolution* of the intercepts that we want to reconstruct. For each of the aforementioned cases, the coefficient for the real tracks can be computed using the entrance position of the particle into the bar. This estimation considers two effects: the first one is multiple scattering caused by the cusp material. The second effect is caused by the thickness of the bars. The bars have a thickness of 1.9 cm and a width of 1.5 cm. This thickness can cause a particle to pass through more than one bar in the same panel. To account for this, the positions of two hits of the same particle on the same panel are averaged. These effects are compared with simulations both with and without the cusp material. It is important to note that this estimation is not a measure of the resolution of the reconstruction, but rather an indication of the effects that can affect the reconstruction and cannot be avoided. In figure 5.15 I show the intercepts in the $\hat{z}\hat{y}$ plane of the actual traces for the simulation with and without the CUSP material, both for the Y and Z direction for

Cusp	Side	Energy cut	# Ev	# Ev. rec.	# Track	# Real	ϵ_e	ϵ_v
N	Alpha	0.4 MeV	107983	8145	11456	6494	7.54	56.69
N	Alpha	1.5 MeV	107983	5881	6955	4533	5.45	65.18
N	Alpha	2.7 MeV	107983	3493	3552	2671	3.23	75.2
N	Asa	0.4 MeV	107983	5870	7862	4548	5.44	57.85
N	Asa	1.5 MeV	107983	4177	4780	3155	3.87	66.00
N	Asa	2.7 MeV	107983	2538	2533	1930	2.35	76.19
Y	Alpha	0.4 MeV	60419	3407	2854	1956	4.30	68.54
Y	Alpha	1.5 MeV	60419	1839	1382	1142	2.29	82.63
Y	Alpha	2.7 MeV	60419	937	735	665	1.19	90.48
Y	Asa	0.4 MeV	60419	2595	1958	1368	5.64	69.87
Y	Asa	2.7 MeV	60419	1385	1040	843	3.04	81.06
Y	Asa	1.5 MeV	60419	716	548	486	1.55	88.69

Table 5.2: Analysis of the tracks detected by DANTE for the Y direction. See table 5.1 for column definition.

the alpha side. As can be seen from these plots the effect of the CUSP trap material is to make the intercepts distributions broader. For each histogram, a Gaussian fit is performed and the mean and standard deviation of the fit are reported to give an idea of the resolution of the reconstruction. The effect of the CUSP trap is not only to widen the central peak, but also to add a background signal at great distances from the annihilation point. These plots are refereed to the case of the minimum energy cut (2.7 MeV). As far as maximum resolution is concerned, there is little difference between this cut and the others. For the sake of completeness, I have reproduced the same plots for the other cases in the appendix B.1.

5.2.3 Testing the reconstruction

As far as reconstruction efficiency is concerned, since reconstruction takes all possible traces into account, all events and traces that we have defined in the tables 5.1 and 5.2 will be reconstructed. We are interested in the number of extra tracks reconstructed (the ghosts mentioned above). Therefore we define:

$$\epsilon_G = \frac{N_{T_{Ghost}}}{N_{T_{Real}}}$$

Where $N_{T_{Real}}$ is the number of actual tracks defined in the previous section and $N_{T_{Ghost}} = N_{T_{Reco}} - N_{T_{Real}}$ is the number of ghost tracks. Since the ghost rate may be dominated by a small subset of events with copious hit multiplicity, I will also specify the mean number of

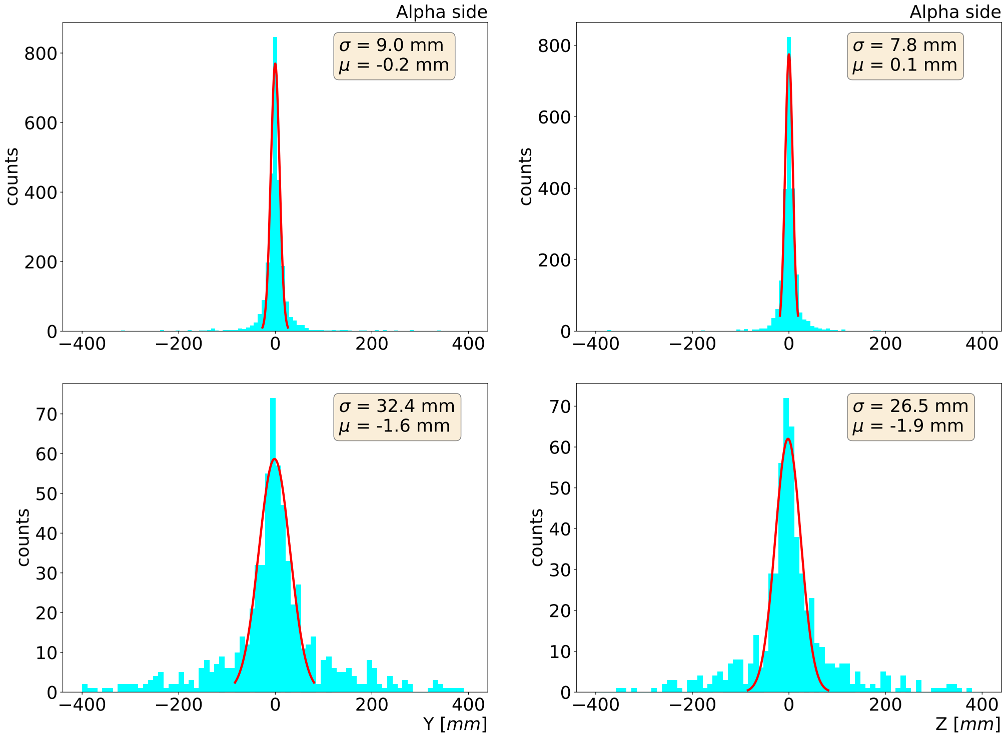

Figure 5.15: Intercepts distributions on the $\hat{z}\hat{y}$ plane for the Y (left) and Z (right) directions, for the ALPHA side, both for the case without (top) and with (bottom) CUSP material, for the *real tracks* in the case with a energy cut of 2.7 MeV. A Gaussian fit is superimposed on the histograms and its variance and mean (σ and μ) are reported.

ghosts per event $N_{G_{Ev.}}$.

As for the estimated resolution of the reconstruction procedure I will focus the quality of the estimate of a track parameter analysing the intercepts z_0 and y_0 and I will use the average of the parameter residual

$$< R >= \frac{1}{N_{Real}} \sum_i \left(X_{0_i}^{Rec} - X_{0_i}^{Real} \right) \tag{5.1}$$

where $X = z, y$ and X^{Rec} is referred to the reconstructed tracks only for those events where we have also a X^{Real}. In addition to this parameter, I will refer to the parameters of the Gaussian fit also used in figure 5.15 for estimating the maximum resolution, since this one will be the one used for real data.

As in the previous section, here too I show two tables, one for the Z-coordinate of the vertices, table 5.3, and one for the Y-coordinate, table 5.4. I have studied two approaches mentioned in section 5.2.1. In the tables I named *partials* the approach (i), where all the intercepts computed are considered and *averages* approach (ii), where an average of the intercepts is considered as the vertex of the event. I also tried to apply the cluster procedure before the reconstruction. I named this test *cluster* in the tables, where the approach (i) is considered after the initial clustering and the reconstruction. In addition also this part of the analysis of the reconstruction is divided in three different energy cuts. The tables show both the number of ghosts and the resolution for each test. I did not add the approach (iii) which consists in average the vertex position over cluster of position and all of them because, although the percentage of ghosts is very high (without eliminating the background, even without combining the information on the two directions we have 300% more traces than can be reconstructed), the average number of ghosts per event is relatively low (never getting more than 2 ghosts per event on average). This indicates that for most events it is not necessary to have to group the intercepts, but it is sufficient to average in those cases with are the most common one. In general the number of ghosts both overall and per event decreases dramatically increasing the energy cut as I was expecting.

As can be seen, the greatest effect on resolution is given by the right energy cutoff and as a second order, by the chosen approach. Another things that is relevant is that the clustering test does not bring any significant improvement to resolution. For Z direction, we can see that the achieved resolution for events with real traces is approximately 2 cm, whereas for Y direction is around 5 cm. The difference is probably due to the fact that the panels closer to the CUSP for the Y direction are composed by only 54 bars and not 60 as the Z direction. As I show in the next section, this is sufficient at least for Z to achieve a vertex resolution, comparable with the resolutions obtained before the upgrade phase. In figure 5.16 I show the histograms of the averaged positions (approach (ii)) of the vertices along Z for the three different energy cuts. Not only it can be seen that with the last cut the sigma of the Gaussian fit decreases by $\approx 40\%$, but also much of the combinatorial background leading to reconstructing vertices at large distances decreases.

5.2.4 Real signal reconstruction

The reconstruction of a real signal, was possible only with the commissioning of DANTE that took place between summer and autumn 2022. The detector was therefore only active for a short time in the last beam time, and furthermore, the work of optimising the parameters of the MUSASHI trap and commissioning the transfer line for antiprotons did not allow the transfer of antiprotons into the CUSP trap until the last weeks of the available beam. Nonetheless, it was possible to acquire a few runs of data, for a first quick check of the acquisition process, the pre-processing of the data and the reconstruction software. However, this was tested using only one of the two sides (ASACUSA side) of the detector

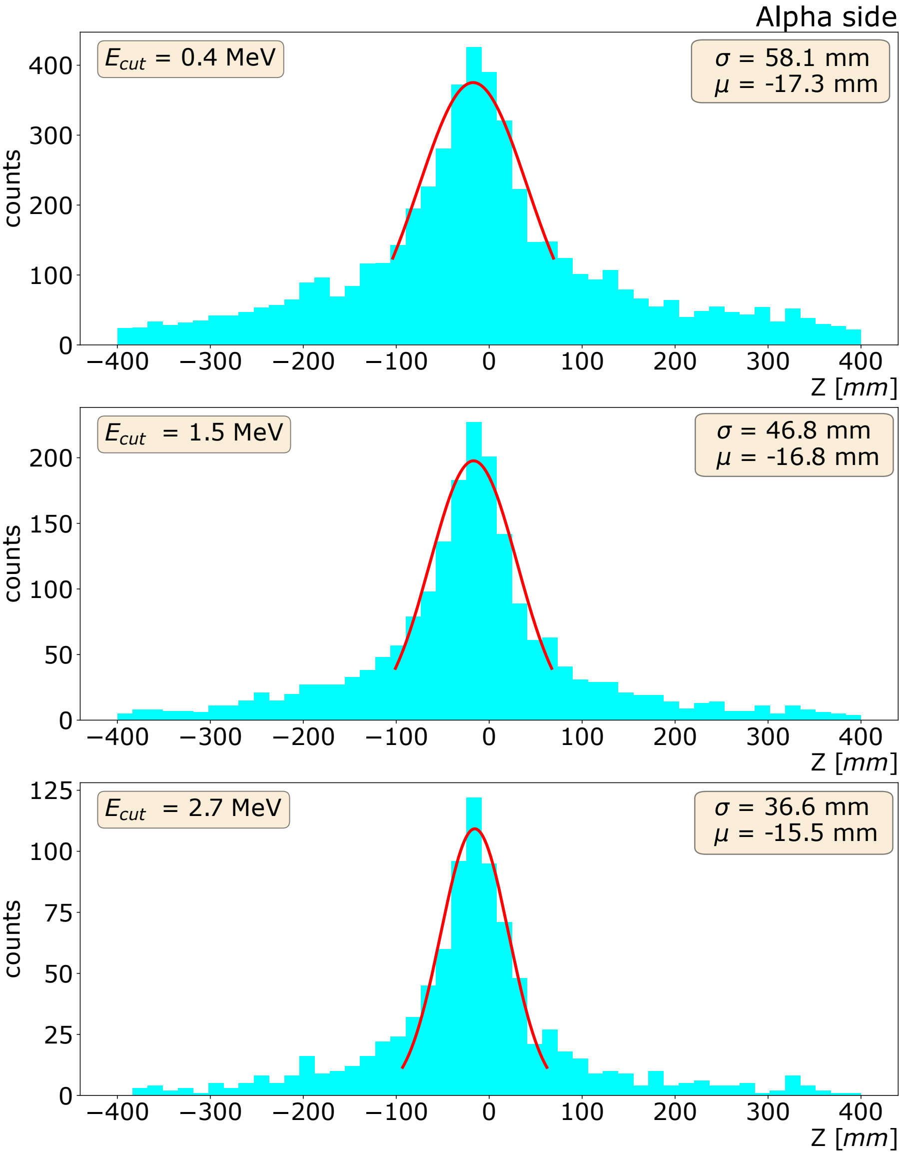

Figure 5.16: Tracks intercepts on the $\hat{z}\hat{y}$ for the Z direction reconstructed with approach (ii) (see the text for definition) for the three energy cuts: 0.4 MeV (top), 1.5 MeV (center), 2.7 MeV (bottom). Gaussian fits are superimposed and mean and variance reported on the top right corners.

Approach	Side	Energy cut	ϵ_{G}	$\mathrm{N}_{\mathrm{G}_{\mathrm{Ev.}}}$	R
Partial	Alpha	0.4MeV	312.0	1.64	55.09
	Alpha	1.5 MeV	129.46	0.77	32.92
	Alpha	2.7 MeV	64.48	0.45	23.54
	Asa	0.4MeV	342.14	1.60	50.54
	Asa	1.5 MeV	140.0	0.78	32.36
	Asa	2.7 MeV	78.34	0.50	26.40
Average	Alpha	0.4MeV	90.64	0.48	29.40
	Alpha	1.5 MeV	67.58	0.40	21.80
	Alpha	2.7 MeV	43.16	0.30	19.31
	Asa	0.4MeV	112.70	0.53	27.86
	Asa	1.5 MeV	79.22	0.44	22.73
	Asa	2.7 MeV	56.68	0.96	20.82
Cluster	Alpha	0.4MeV	166.43	0.87	28.94
	Alpha	1.5 MeV	92.88	0.55	21.66
	Alpha	2.7 MeV	53.10	0.37	19.59
	Asa	0.4MeV	192.14	0.90	27.41
	Asa	1.5 MeV	105.94	0.59	22.46
	Asa	2.7 MeV	67.50	0.43	20.82

Table 5.3: Efficiency and resolution analysis for reconstruction of simulated hits for the Z direction. First column, approach used for estimating intercepts per event (see the text for definition). Second column, side of panel analysed. Third column, energy cut selected. Percentage of ghost tracks, $\frac{N_{T_{Reco}}-N_{T_{Real}}}{N_{T_{Real}}}$. Resolution computed as in 5.1.

because of an issue with the electronics that we could not fix before the end of the runs.

A single run could last several tens of minutes. Antiprotons were accumulated over the course of one or more AD shots, thus every two minutes or more, then slowly released into a localised area of the MRE of the CUSP trap. Slow release means a lowering of the electrostatic confinement potential on the order of seconds. This is an important aspect to take into account. Since the acquisition is continuous during the same run, it is important to select the right time window associated with the slow release of antiprotons. This aspect is clear by referring to the figure 5.17. Here the reconstructed positions of the vertices on the Z axis are shown as a function of time. As can be seen, clusters in which the reconstructed peak is evident are located in time. However, if one were to consider the reconstructions of all the hits acquired over the time span of the run, these could be covered by background noise. As can be also seen, the peak of reconstructed events is present three times. This is because in the same run we tried multiple trapping in order to see if the position was

	Side	Energy cut	$\epsilon_{\text{GEV.}}$	$N_{\text{GEV.}}$	R
Partial	Alpha	0.4MeV	271.84	2.01	113.12
	Alpha	1.5 MeV	118.63	0.89	80.69
	Alpha	2.7 MeV	63.61	0.52	79.60
	Asa	0.4MeV	283.33	1.84	102.27
	Asa	1.5 MeV	119.81	0.88	73.31
	Asa	2.7 MeV	66.46	0.51	69.66
Average	Alpha	0.4MeV	72.86	0.42	86.84
	Alpha	2.7 MeV	60.89	0.38	67.53
	Alpha	1.5 MeV	40.90	0.29	70.14
	Asa	0.4MeV	88.86	0.47	79.70
	Asa	1.5 MeV	64.29	0.39	60.64
	Asa	2.7 MeV	47.36	0.32	59.38
Cluster	Alpha	0.4MeV	142.77	0.82	86.24
	Alpha	1.5 MeV	86.35	0.53	67.34
	Alpha	2.7 MeV	50.08	0.36	70.19
	Asa	0.4MeV	159.32	0.84	78.32
	Asa	1.5 MeV	89.56	0.55	60.20
	Asa	2.7 MeV	56.17	0.38	59.20

Table 5.4: Efficiency and resolution analysis for reconstruction of simulated hits for the Y direction. See table 5.3 for columns definitions.

consistent over time.

As with the analysis of the simulations, I wanted to study the behaviour of the reconstruction of the real signal by considering a cut-off in energy. In this case, since a calibration of the detector acquisition has not yet been done, the cut is referred to the ADC value, which corresponds to the (digitized) value of the collected light of a given channel. Figure 5.18 shows the signal in ADC, for one of the panels for all the hits acquired during the run under consideration. As can be seen, again after an initial peak due to the noise, there is one at higher values that should correspond to the signal from the MIPs. I therefore chose to apply reconstruction using approach (ii) without cutting the signal in ADC and with a cut indicated by the black line in figure 5.18. The two results are shown in figure 5.19b and 5.19a for the test with and without cut, respectively. From these figures we can see how the correct energy cutoff brings the sigma of the Gaussian fit of the reconstructed vertices distribution to a value that can make us distinguish the location of the annihilations between one electrode and another. The peaks are at ≈ -350 mm because the electrode in which to trap the antiprotons chosen for this run was the most upstream, the first coming

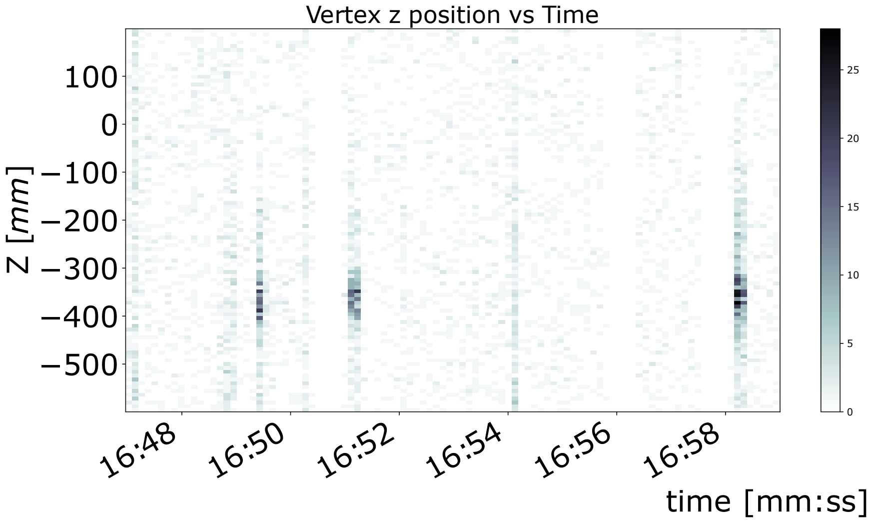

Figure 5.17: Distribution of intercepts on $\hat{z}\hat{y}$ for the Z direction, reconstructed for real data vs time of acquisition. The time axis is divided into 1s bins. Intercepts are reconstructed with approach (ii) (see the text for definition).

from MUSASHI. With this reconstruction, it is also possible to make a first estimation of the number of antiprotons trapped in this run. In total for this specific shot 3150 event have been reconstructed. If we refer to table 5.3 in the *avarage* case, with a energy cut value of 2.7 MeV we have roughly 36% of ghost tracks more than the real. If then we take into account the efficiency estimates in table 5.1, for this energy cut and for the ASACUSA side, we see that the events that can be reconstructed are 1.03% of all the events where we have at least one hit and 0.55% of the total 120000 events. This gives us approximately $\approx 3.7 \cdot 10^5$ antiprotons trapped in this run. However this is only an initial estimate which overestimates the number of antiprotons. In order to have an accurate estimate also the efficiency of the detector has to be taken into consideration. Moreover adding to the analysis of Monte Carlo simulation, consideration about the times needed for particles to cross the CUSP and the magnetic field could improve the estimate of the number of antiprotons. As can be seen, most of the reconstructed vertices that are eliminated with the energy cut are not about the peak, but about the background combinatorial noise.

5.3 Summary

In this chapter I have discussed my contribution to the commissioning and upgrade project of the DANTE detector. After presenting the history of this detector, discussing the rea-

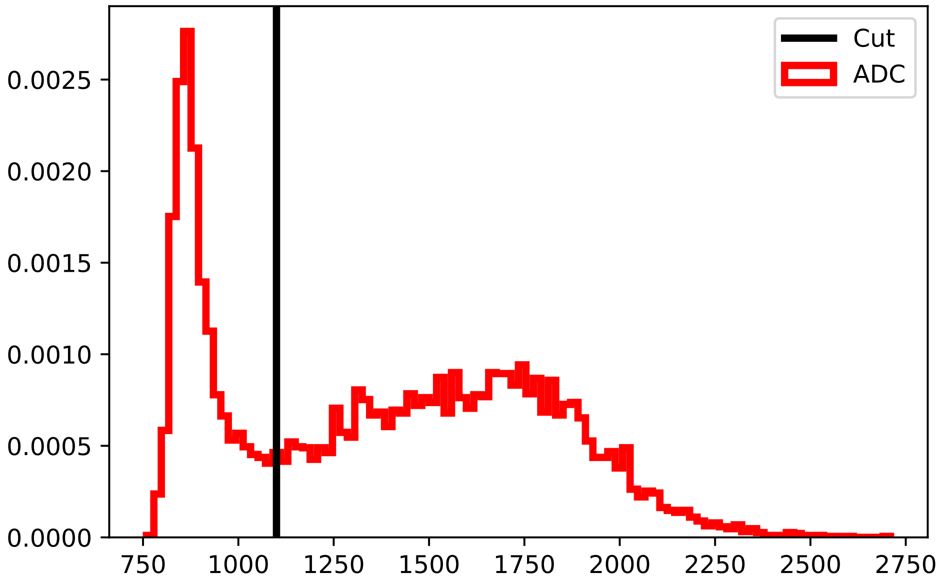

Figure 5.18: ADC distribution for all the events registered in one of the last run of 2022 for the inner panel of the ASACUSA side. In black the value of the ADC cut applied for the reconstruction.

sons for an upgrade and summarising the work done at both hardware and software level, I focused on the work concerning signal reconstruction, for which I was responsible.

In summary, my contribution consisted in developing and testing a reconstruction code for the detector. The code has to be able to adapt to different possible configurations that the detector can take over the course of its use. The code was tested for the configuration chosen for current use. The tests were accompanied by Monte Carlo simulations, which were first analyzed and then used as a test set for the reconstruction phase. I chose to test a few different types of approaches for locating the vertex position and studied the trend as the deposition energy changed, so as to estimate the reconstruction behavior with the different types of approaches. After testing on simulated data, the reconstruction algorithm was applied to the real ones. As Figure 5.19b shows, it was possible to reconstruct the signal in the last data-taking runs of 2022, and it was verified that the behaviour of the reconstruction algorithm follows that of the simulated tests to a first approximation. This result will be useful for the next data-taking period, the goal of which is the creation of an antihydrogen beam for spectroscopy measurement and for which the optimization of procedures to be performed with the CUSP trap will be crucial and will require the information provided by

DANTE.

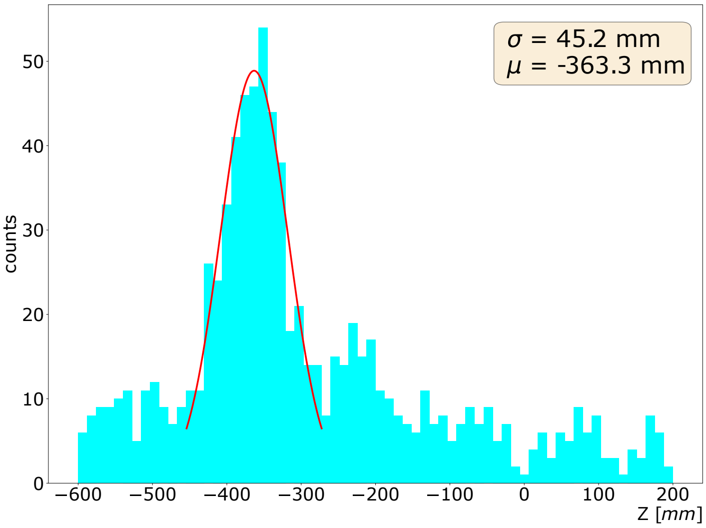

(a)

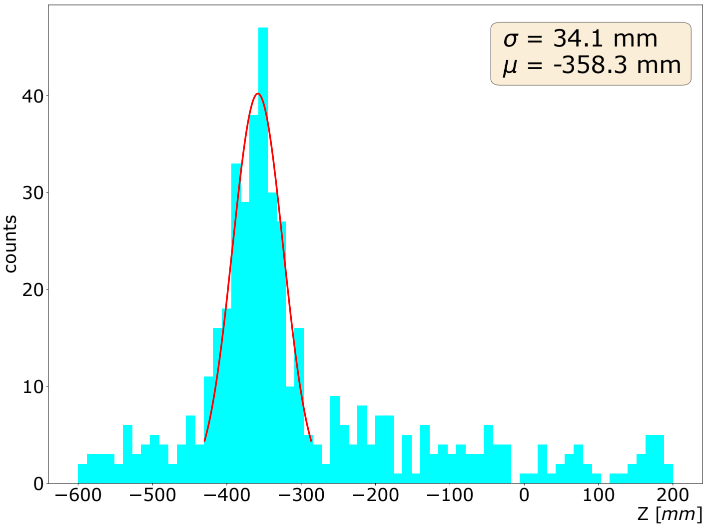

(b)

Figure 5.19: Distribution of the reconstructed intercepts on the $\hat{z}\hat{y}$ plane for real data. The intercepts are reconstructed with the hits of the panels of the ASACUSA side with the approach (ii) (see the text for definition). The events are selected by time acquisition around the third peak of figure 5.17. (a) Reconstruction with all the events. (b) Reconstruction after the ADC cut shows in figure 5.18 is applied. A Gaussian fit is superimposed and the resulting mean and variance are shown in the top right corner.

Chapter 6

Conclusion

In the development of this thesis work, two contributions were made to the core research lines of the ASACUSA collaboration. Below, I will summarize the results and main points achieved by these contributions. Finally, I will suggest possible developments for the projects in which I participated, particularly for the aspects to which I contributed.

6.1 Characterization of products of $\bar{p}$ annihilations at rest

In the project on the characterization of products of antiproton annihilations at rest, my contribution involved several aspects. At the beginning of my Ph.D., the data collection was complete, and I assisted in completing the remaining work required to conclude the project. The project required two key components: firstly, developing digitizations of the simulated signal using software developed in Geant4, and secondly, developing simulations using the FLUKA simulation software. The primary goal of the project is to test the Monte Carlo simulation software used in the field of particle physics, and these two steps were crucial to its completion.

As shown in Chapter 4, both goals were achieved. With respect to digitization, the main results of this step are reported in Figures 4.17, A.3, A.8, and 4.16, A.4, A.9, which compare the distributions of the deposited energy reconstructed for raw simulations and for digitized clusters with and without saturation of MIPs and HIPs for carbon, gold, and molybdenum. This information was crucial to faithfully reconstructing the clusters of HIPs and MIPs. Thanks to this reconstruction, it will be possible to directly compare the multiplicities and energy depositions of the simulations with the data acquired from the combination of the signal given by the hodoscope and Timepix3. In addition to simulations using Geant4 software, simulations using FLUKA software were also developed and digitized. The most significant results of this step are presented in Figures 4.23, A.6, A.11, A.2, 4.24, and A.13, which show the multiplicities per event of MIPs and HIPs for carbon, gold, and molybdenum using both Geant4 software with CHIPS and FTF models, as well as FLUKA software. These signals will ultimately need to be compared with the analyzed data leading up to the publication of the paper. Furthermore, my contribution to the project involved considering the effect of acceptance by applying a correction to the signal acquired by the hodoscope. The effect of this correction is shown in Figures 4.26a, 4.26b, and 4.26c, which compare the number of prongs measured by the hodoscope with those corrected for detector acceptance for the three targets used in the measurement.

6.2 DANTE signal reconstruction

With regard to the work on the DANTE detector reconstruction software, my contribution was essential for the completion of the entire project. As mentioned several times throughout my thesis, the entire ASACUSA experiment underwent a series of upgrades during the long-shutdown phase that covered much of my PhD. These upgrades included, among other things, the upgrade of the DANTE detector. As I mentioned in my thesis, in the next beamtime, this detector will be essential in optimizing the trapping and cooling processes of antiproton plasmas in the CUSP trap and in studying and optimizing the mixing processes of positron and antiproton plasmas to create the antihydrogen beam needed for spectroscopy measurements. A key step in this upgrade framework was to develop a detector signal reconstruction software.

As shown in Figure 5.19b, the final goal of my contribution can be considered achieved. The histogram shows the positions on the beam axis of vertices reconstructed for data acquired in December 2022 in some calibration runs that ASACUSA was able to acquire before the winter shutdown. These reconstructions will provide information on the location and number of annihilations (i.e., the number of trapped particles) during the optimization steps mentioned above. To assess the efficiency of the reconstruction algorithm and obtain the best possible resolution of the vertex position reconstruction, I used Monte Carlo simulations to study the behavior of the reconstruction by varying the energy cuts of the hits recorded by the detector. I also checked for possible improvements in approaching the reconstruction problem in different ways, such as applying a clustering algorithm to consider the inherent noise given by a particle crossing the same panel multiple times because of its thickness or considering an average of the reconstructed positions instead of considering them separately. The best-performing approach in terms of efficiency, resolution, and execution time was chosen and applied to real data.

6.3 Further developments

Although my thesis work can be considered complete and the goals I set have been achieved, there is still a vast amount of work that can be done and improvements that can be made, both to my work and to projects in which I have personally contributed.

The project on measuring annihilations of resting antiprotons has completed its first phase with my thesis work. However, as discussed in section 2.4 of the project presentation, a dedicated line for these measurements in ASACUSA is already under development and installation. The plan is to extend the study of annihilation products to various types of targets in 2023 and 2024, with much more comprehensive data. This will be possible with the new detector designed specifically for this measurement, which has a much higher acceptance and efficiency than the previous one. The work presented in my thesis will also contribute to these measurements, with simple modifications to the simulation geometry in Fluka, and the digitization process can be replicated for new simulations. However, the digitization process needs to improve the reproduction of cluster size, as pointed out in section 4.3.3. The only limitation of the digitization work was related to this aspect. Therefore, there is a plan to use machine learning (ML) techniques to classify the signals produced by the Timepix according to the signal clusters, and if this digitization flaw is solved, simulations could be used for eventual training. The new line dedicated to the study of low-energy antiprotons opens up possibilities for other projects currently under development and feasibility analysis. For example, one project is to perform a quantum interferometry measurement of antiprotons, using an interferometer to be installed inside the line specifically for the measurement. Another project already under development is designing a calorimeter for measuring the Pontecorvo reaction (mentioned in section 2.3.5) for three mesons. To date, these reactions have not been observed, and this project could contribute significantly to determining which model to use to describe these rare processes

In terms of the work on the DANTE signal reconstruction, a natural continuation of my thesis work would be to extend the software to cover cases where the detector has a different configuration from the one chosen for this beam-time. Although I was unable to deal with this during my Ph.D., as explained in the appendix, I have set up the software to allow for an easy extension to different detector configurations. As mentioned in a later section, a final study to further define the efficiency of the reconstruction would be to simulate the effect of different annihilations as a function of time and implement the magnetic field of the CUSP trap in Monte Carlo simulations.

Appendix A

FLUKA and $Allpix^2$ simulations details

A.1 FLUKA code details

The code of this part of the theis work is available to the collaboration via the GitLab dedicated directory *Hbar-flk-gshfs* in the ASACUSA GitLab directory. For anyone that is not part of ASACUSA, I will soon create a personal GitHub directory.

For the development work of the simulations in FLUKA, Flair software was used for the construction of the geometry and the basic configuration of the simulation. For typical FLUKA software use, a simulation can be defined through a series of commands entered via a configure file. Flair is a software that facilitates the construction of this file, allows the reconstructed geometry to be visualised in real time and also allows simulations to be compiled and executed. Both the version of FLUKA and Flair used for this thesis are the latest[1] versions released by the FLUKA working group at CERN. For this thesis, however, the basic options provided by the FLUKA software were not sufficient. Indeed, it was essential to produce an output file with the necessary information for the analysis and, no less important, with the same data structure, so that the analysis code could be applied independently of the simulation. The simulation output file was to consist of the following branches: even, energy (with two leaves Edopo and Ekin) position (with three leaves x, y, z) particle, PDG_code, detector, track_id, parent_id. The names I have given above are the names the branches must have in order for the cluster analysis software to be applied. In order to create it, I had to implement a macro that would convert the txt output of FLUKA into a ROOT file with these branches. In addition this has led to some additions that go beyond common usage of FLUKA. In particular, the USERDUMP command had to be added to the configu-

---

[1] As of the date of writing this thesis, December 2022.

ration file, which allows a customised output file to be created by the user. In addition, I had to modify the *mgdraw* library in order to obtain information about the deposited energy, position, PDG_code and detector and *stupre* and *stuprf* for information about the track_id and parent_id. A code in bash to automate the simulation, given the configuration name *.inp* and the number of simulations to be performed concludes the code

A.2 $Allpix^2$ code details

The code of this part of the theis work is available to the collaboration via the GitLab dedicated directory *Hbar-allpix-gshfs* in the ASACUSA GitLab directory. $Allpix^2$ is designed as a modular framework. This modular feature allows for an easy extension to more complex and specialized detector simulations and moreover to separate the core of the framework from the implementation of the algorithms in the modules. There are modules for creating the geometry of the various detectors, modules for specifying the characteristics of the detectors, for the models to be used and so on. For anyone that is not part of ASACUSA, I will soon create a personal GitHub directory.
For the digitization process, I created 3 files that$Allpix^2$ reads to select the various modules to be used:

- detector_tpx.conf
- timepix_bare.conf
- tmpix_digit.conf

The first file specifies the positioning of these detectors in space. Although in our case $Allpix^2$ is not used for a reproduction of the entire simulation, it is necessary to place the detectors in space so that $Allpix^2$ can reconstruct the position of individual detector pixels. Since the energy depositions are given by different codes, this placement in space of the detectors must be performed using those of the simulations as reference points.

The second file is used to set the type of detector in use, in our case a Timepix3. In this one, the specifications of the detector in particular are given:

- number_of_pixels = 256 256
- pixel_size = 55 μm 55 μm
- sensor_thickness = 300 μm
- sensor_excess = 0 mm
- bump_sphere_radius = 9.0 μm

- bump_cylinder_radius = 7.0 μm
- bump_height = 20.0 μm
- chip_thickness = 700 μm
- chip_excess = 0 mm

The third file is the one dedicated to digitisation per se. I report in table A.1 a list of the main module used in this file. These modules follow the various steps of the process discussed in the section 4.3.2. Most of the modules are standard modules of the $Allpix^2$ software and a full description of their parameters can be found in the dedicated manual [138]. Worthy of note are the modules and . In this module, an option has been implemented to include the saturation effect given by the Volcano effect, through a new parameter called Saturation. The second is a module dedicated to this work, which creates specific ROOT files for cluster data analysis on the Timepix sensor.

Module	Functionality
DepositionReader	This module is needed for reading energy depositions simulated by a MC simulation.
EletrctricFieldReader	This module generates a depletion field in the sensor.
ProjectionPropagation	This module operates the projection of the charges generated on the sensor.
SimpleTransfer	This module transports the charges on the sensor after the projection phase.
DefaultDigitizer	This module generates the ADC signal corresponding to the chagerges collected on the pixel. At this point we inserted the saturation modification.
DetectorHistogrammer	This module is needed for generating usefull plots.
ADTreeWriter	This module is a personalized module that writes a ROOT file with the cluster information needed for the analysis step.

Table A.1: List of modules used for the $Allpix^2$ simulations.

The code is concluded by a small bash script that allows the automation of the application of the digitisation procedure to a ROOT file[2]. This needs the path of the file to be digitised and a series of parameters to identify the name of the output files, in particular I

---

[2] The ROOT file in question must necessarily have the structure described in the previous section.

chose to identify the files with 3 parameters: *Simulation model*, *Target material*, *Identification number*.

A.3 Simulations material

The plots corresponding to targets of different materials with respect to those presented in chapter 4 are reported in the following figures. In general for every target the following list of plots is reported:

- A comparison between raw, digitized and digitized with saturation distributions generated by the FTF model of the energy deposited per cluster (or tracks in the raw case) for HIPs and MIPs.
- A comparison among the distributions generated by the different models of the energy deposited per cluster for HIPs and MIPs
- A comparison among the distributions generated by the different models of the number of HIPs and MIPs generated per events
- A comparison among the distributions generated by the different models of the number of tracks reconstructed by the hodoscope signals per event.

In particular, in Figures 4.17 and 4.16, in section 4.3.3, I showed the distribution of the energy deposited simulated with the FTF model for the raw simulation, digitized simulation and digitized with saturation simulation, respectively for MIPs and HIPs in the carbon target case. In Figures A.3 and A.4 I show the distributions for MIPs and HIPs for the gold target case and in Figures A.8 and A.9 for the molybdenum target case.

In Figure 4.21, in section 4.4.3 I showed the distributions of the number of tracks reconstructed with the hodoscope signal for the three models in the carbon target case. In Figure A.7 I show the same distributions for the gold target case and in Figure A.14 for the molybdenum target case.

Finally in section 4.4.4, I showed for the gold target case the HIPs distributions of the deposited energy for digitized simulation for the three models in Figure 4.25 and the HIPs multiplicities distribution in Figure 4.24. For the carbon target case I showed for MIPs the same deposited energy distributions in Figure 4.22 and multiplicities distributions in Figure 4.23. Here below I show the HIPs deposited energy and multiplicities distributions for the gold target case in Figure A.5 and A.6 respectively and for the carbon target case the energy and multiplicities distributions in Figure A.1 and A.2 respectively. In Figure A.10, A.11 I show the deposited energy and multiplicities distributions for MIPs in the molybdenum target case and in Figure A.12 and A.13 the same distributions for HIPs.

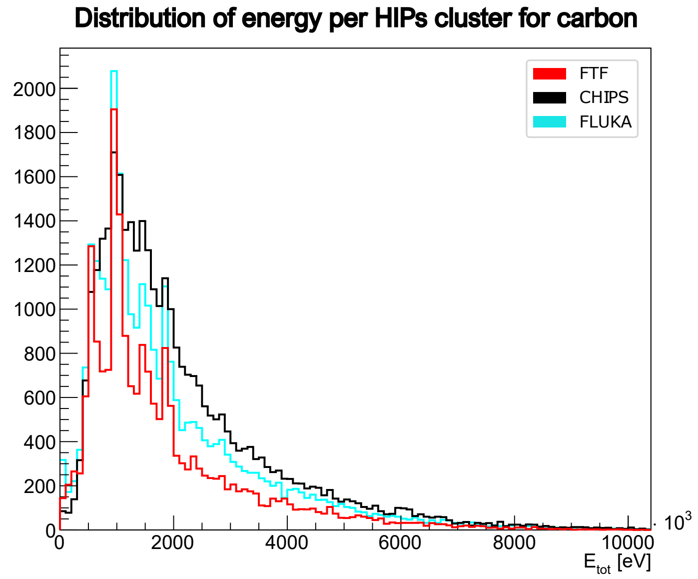

Figure A.1: Distribution of the total energy deposited in HIPs clusters from annihilations on carbon target, for the Geant4 simulation with the FTF model (red), with the CHIPS model (black) and the FLUKA simulation (light blue).

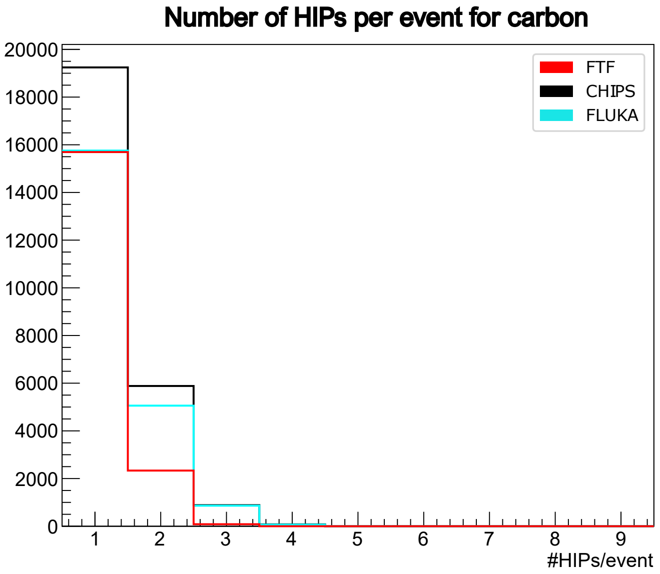

Figure A.2: Number of HIPs per event from $\bar{p}$ annihilations on carbon target for the Geant4 simulation with the FTF model (red), with the CHIPS model (black) and the FLUKA simulation (light blue).

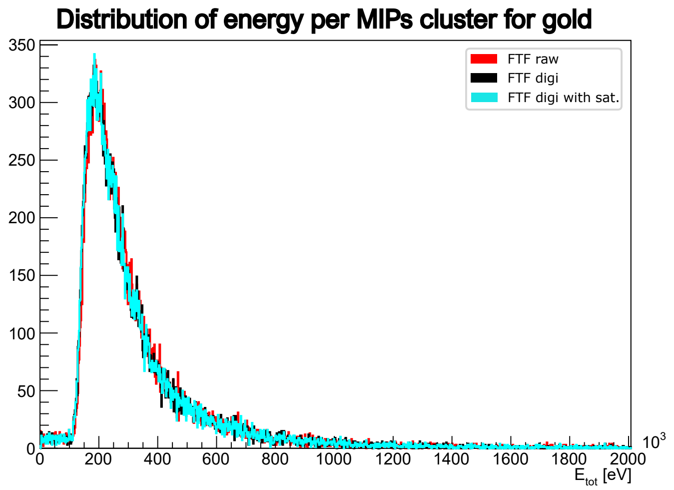

Figure A.3: Distribution of the total energy deposited by MIPs from annihilations on the gold target. (red) Total energy integrated on the path inside the sensor region in the raw Geant4 simulation for the FTF model. (black) Total energy integrated on the cluster given by digitization, without the saturation effect included. (light blue) Total energy integrated on the cluster given by digitization, with the saturation effect included.

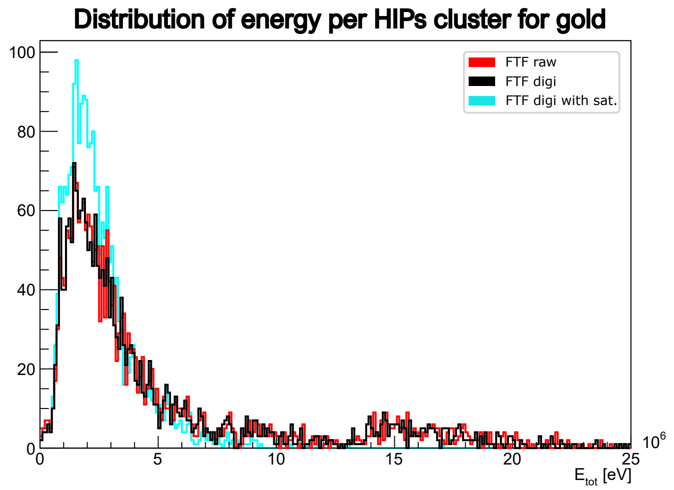

Figure A.4: Distribution of the total energy deposited by HIPs from annihilations on the gold target. (red) Total energy integrated on the path inside the sensor region in the raw Geant4 simulation for the FTF model. (black) Total energy integrated on the cluster given by digitization, without the saturation effect included. (light blue) Total energy integrated on the cluster given by digitization, with the saturation effect included.

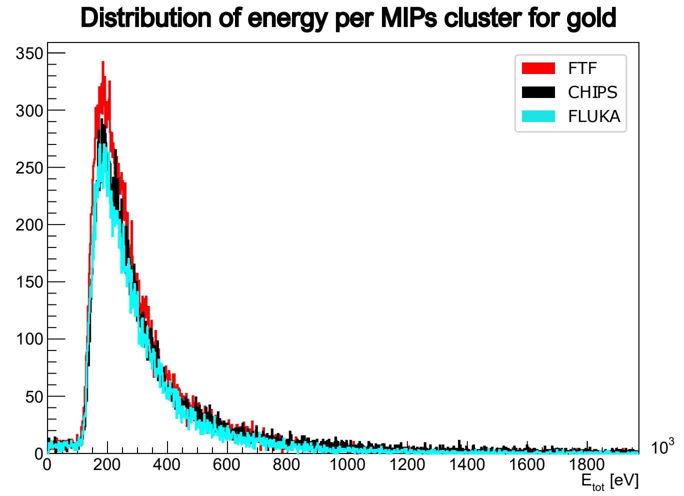

Figure A.5: Distribution of the total energy deposited in MIPs clusters from annihilations on the gold target, for the Geant4 simulation with the FTF model (red), with the CHIPS model (black) and the FLUKA simulation (light blue).

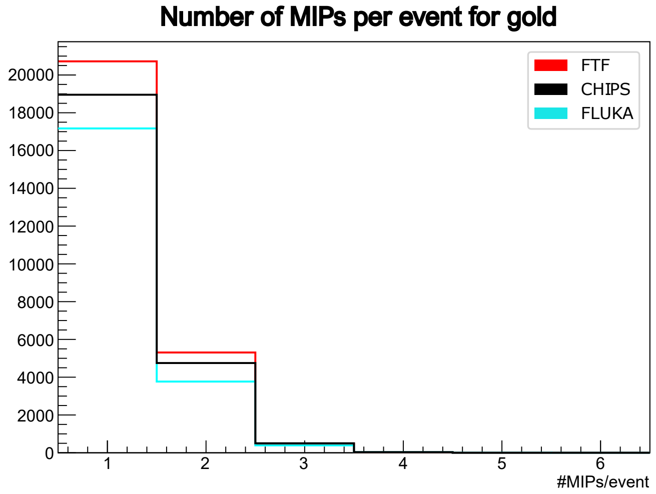

Figure A.6: Number of MIPS per event from $\bar{p}$ annihilations on the gold target for the Geant4 simulation with the FTF model (red), with the CHIPS model (black) and the FLUKA simulation (light blue).

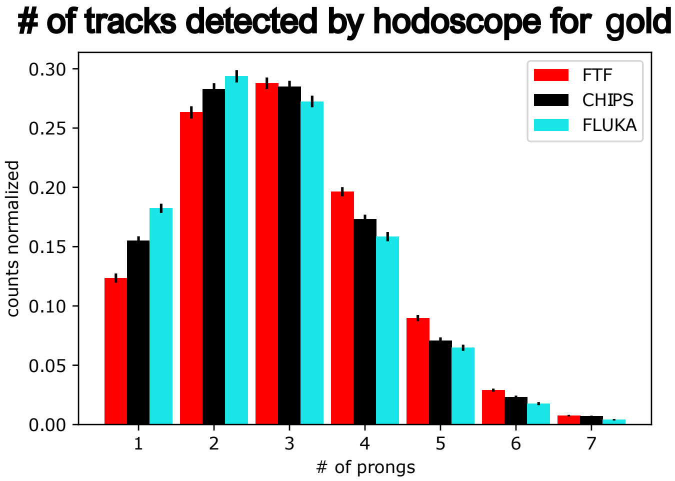

Figure A.7: Number of tracks of products of annihilations on the gold target, reconstructed per event with the hodoscope signal for: the Geant4 simulation with the FTF model (red), with the CHIPS model (black) and the FLUKA simulation (light blue).

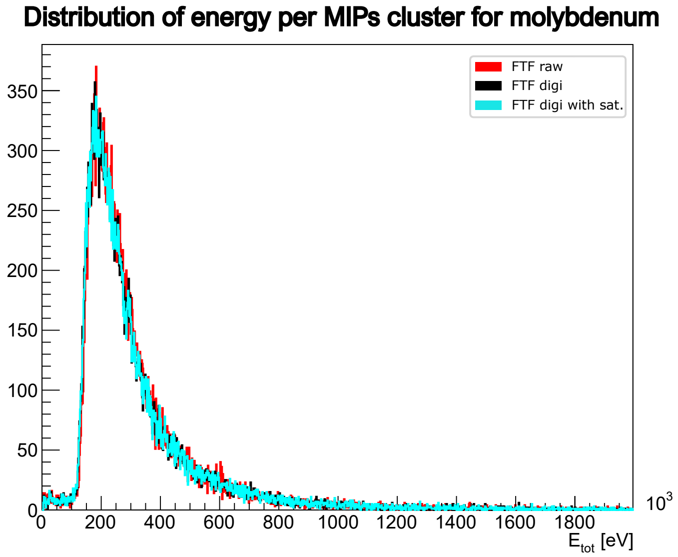

Figure A.8: Distribution of the total energy deposited by MIPs from annihilations on the molybdenum target. (red) Total energy integrated on the path inside the sensor region in the raw Geant4 simulation for the FTF model. (black) Total energy integrated on the cluster given by digitization, without the saturation effect included. (light blue) Total energy integrated on the cluster given by digitization, with the saturation effect included.

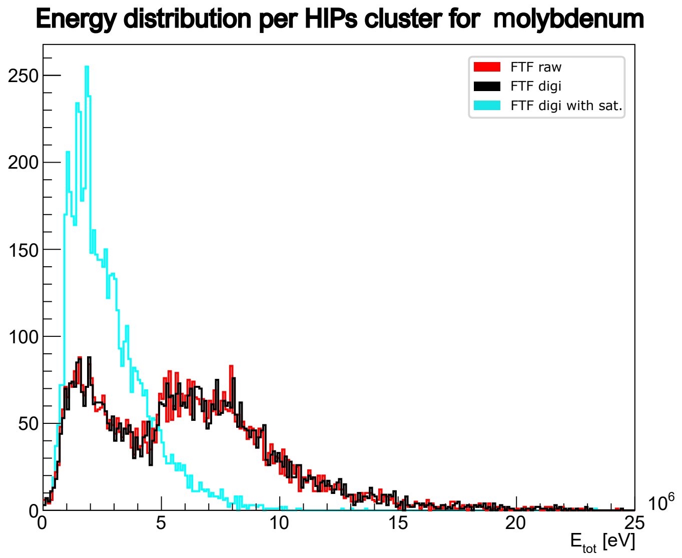

Figure A.9: Distribution of total energy deposited by MIPs from annihilations on molybdenum target. (red) Total energy integrated on the path inside the sensor region in raw Geant4 simulation for FTF model. (black) Total energy integrated on the cluster given by digitization, without saturation effect included. (light blue) Total energy integrated on the cluster given by digitization, with saturation effect included.

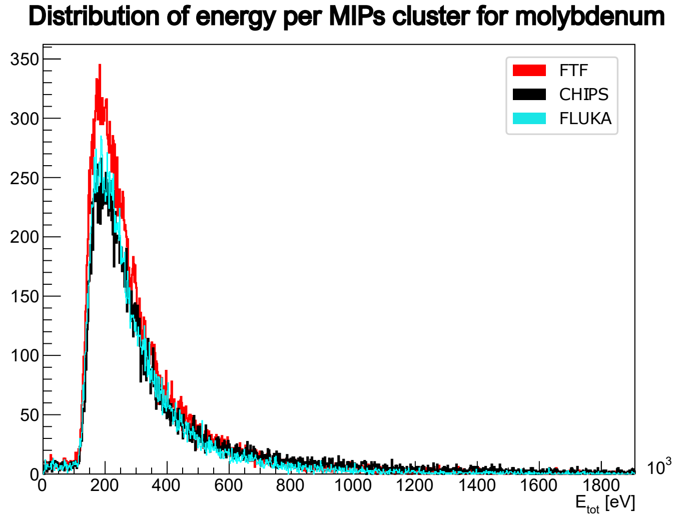

Figure A.10: Distribution of the total energy deposited in MIPs clusters from annihilations on the molybdenum target, for the Geant4 simulation with the FTF model (red), with the CHIPS model (black) and the FLUKA simulation (light blue).

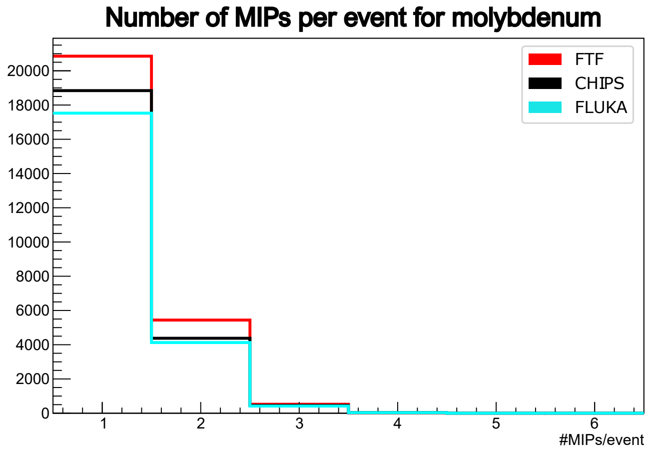

Figure A.11: Number of MIPS per event from $\bar{p}$ annihilations on the molybdenum target for the Geant4 simulation with the FTF model (red), with the CHIPS model (black) and the FLUKA simulation (light blue).

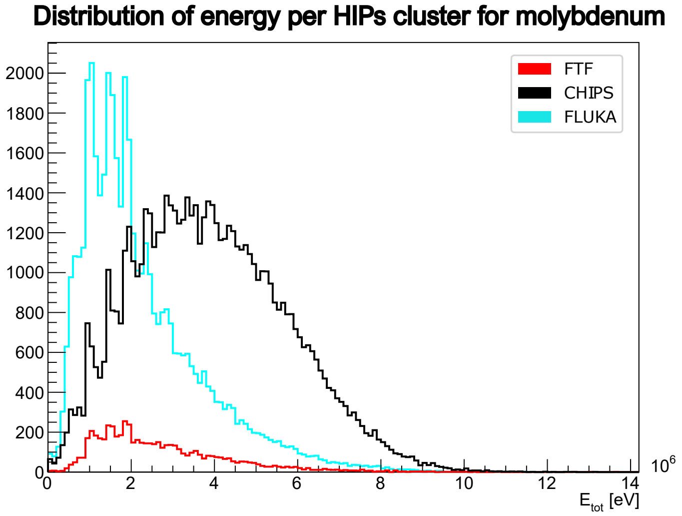

Figure A.12: Distribution of the total energy deposited in HIPs clusters from annihilations on the gold target, for the Geant4 simulation with the FTF model (red), with the CHIPS model (black) and the FLUKA simulation (light blue).

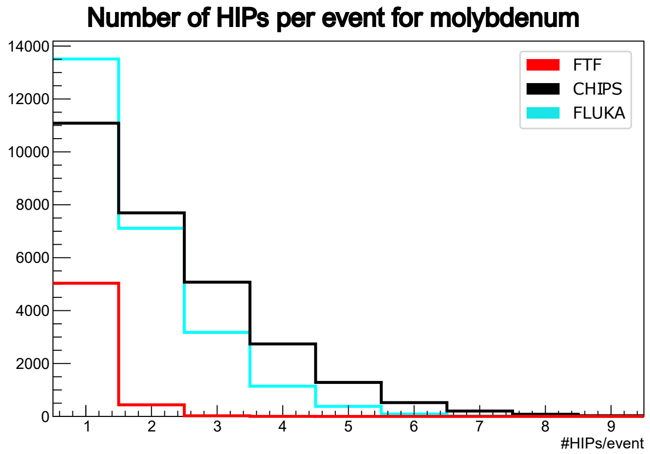

Figure A.13: Number of HIPs per event from $\bar{p}$ annihilations on the molybdenum target for the Geant4 simulation with the FTF model (red), with the CHIPS model (black) and the FLUKA simulation (light blue).

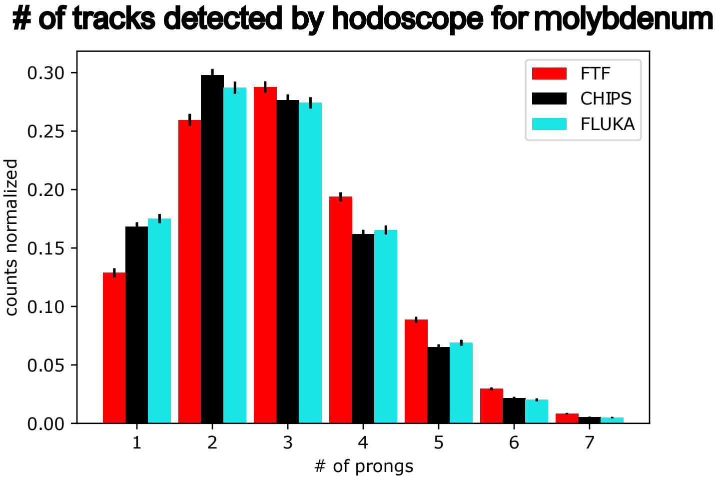

Figure A.14: Number of tracks of products of annihilations on the molybdenum target, reconstructed per event with the hodoscope signal for: the Geant4 simulation with the FTF model (red), with the CHIPS model (black) and the FLUKA simulation (light blue).

Appendix B

DANTE reconstruction

B.1 Code details

The code of this part of the theis work is available to the collaboration via the GitLab dedicated directory *brescia-detector* in the ASACUSA GitLab directory. Figure B.1 shows the general structure of the folder. As you can see, in addition to my contribution, this folder contains the work of other members of the collaboration regarding the code dedicated to simulation in Geant4, DAQ and pre-processing, plus some useful macros such as the one used to calculate the geometrical acceptance of the detector in the 5.2.3 section. As can be seen, the geometry configuration file (*panels.yaml*) is located at this general directory level. This is because the various specific codes use this file, which is updated according to the use of the detector. As for the signal reconstruction code, a structure of the code core is shown in figure B.2. For a higher adaptability of the code to different detector configurations, I thought of structuring the code in modules, each with a specific function. As you can see

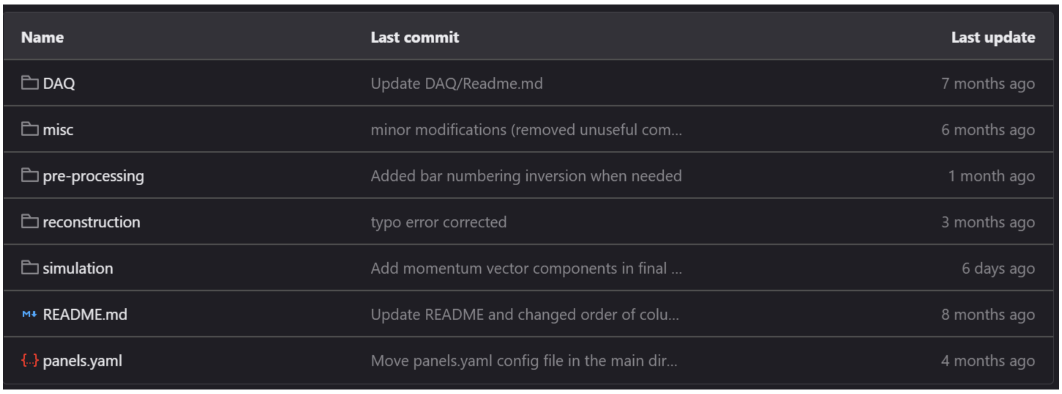

Name	Last commit	Last update
DAQ	Update DAQ/Readme.md	7 months ago
misc	minor modifications (removed unuseful com...	6 months ago
pre-processing	Added bar numbering inversion when needed	1 month ago
reconstruction	typo error corrected	3 months ago
simulation	Add momentum vector components in final ...	6 days ago
README.md	Update README and changed order of colu...	8 months ago
panels.yaml	Move panels.yaml config file in the main dir...	4 months ago

Figure B.1: Structure of the main directory of the code dedicated to DANTE.

from the figure, I have identified two basic structures, the panel (*panel.py*) and the track (*track.py*). The former contains the information (positions and energy) given by the DAQ or the simulations of the hits associated with that panel, as well as general information about the panel (i.e. directionality of the bars, position along the X-axis, panel ID, any angles of inclination of the panel, offsets and so on). On the other hand, the latter contains all the traces identified per side of the detector. The tracks per se are identified by the parameters discussed in the 5.2.1 section, these are entered into a pandas dataframe which identifies them by event number. I have dedicated a module (*patterreconstructor.py*) to the handling of line reconstruction, at the moment a module is implemented that applies the combinatorial procedure between points. In the future if the need arises, a module can be created in this file dedicated to the reconstruction of patterns given by several points per line. Another module (*vertexfinder.py*) is dedicated to the reconstruction of the vertex. Again, different types of modules can be designed depending on the problem. Finally, I have dedicated two modules to manage the entire reconstruction process. The first (*world.py*) handles the configuration of the modules, reads the yaml file and reads the information on the hits, then based on this information creates the various panels and associates the corresponding information with them. The second (*datamanager.py*), on the other hand, is a module of a general nature, it manages the process from start to finish, creating a world and associating the corresponding yaml file to it, it calls the various modules in order according to the

```
├── README.md
├── environment.yml
├── requirements.txt
├── scripts
│   └── run_reco.py
├── src
│   ├── apparatus.py
│   ├── datamanager.py
│   ├── panel.py
│   ├── patterreconstructor.py
│   ├── track.py
│   ├── vertexfinder.py
│   └── world.py
└── utils
    ├── patterrconstructor_utils.py
    ├── utils.py
    ├── datamanager_utils.py
    └── vertexfinder_utils.py
```

Figure B.2: Structure of the Reconstruction section of the code dedicated to DANTE.

problem selected and allows certain parameters to be set, such as the different clustering processes or energy cuts.

B.2 Simulations material

Here below the plots produced during the analysis of DANTE simulation and the development of the reconstruction software are reported. In Figure 5.15, in section 5.2.2, I showed the distribution of the intercepts of those tracks that are hitting at least two panel with bars in the same direction on the same side (ASACUSA or ALPHA side). That was the case for the ALPHA side for the energy cut at 2.7 MeV which is the most significant. Here below in Figures B.3a, B.4a, B.3b, B.4b, B.5 I show the same distributions for the ALPHA side for energy cuts at 0.4 MeV and 1.5 MeV and for the ASACUSA side for energy cuts at 0.4 MeV, 1.5 MeV and 2.7 MeV respectively.

In Figure 5.16, in section 5.2.3 I showed the distribution of reconstructed intercepts using hits of the panel with vertical bars of the ALPHA side for the three energy cuts, using the *average* approach, which consists in averaging the position of the intercepts reconstructed for a single event. In figure B.9, B.10, B.11 I show the same distributions for the ALPHA sides, for both vertical bars (right column) and horizontal bars (left column) for the *partial*, *average* and *cluster* approaches respectively. Figure 5.16 is repeated in Figure B.10 on the right column. In Figures B.6, B.7, B.8 I show the same distribution for the ASACUSA side.

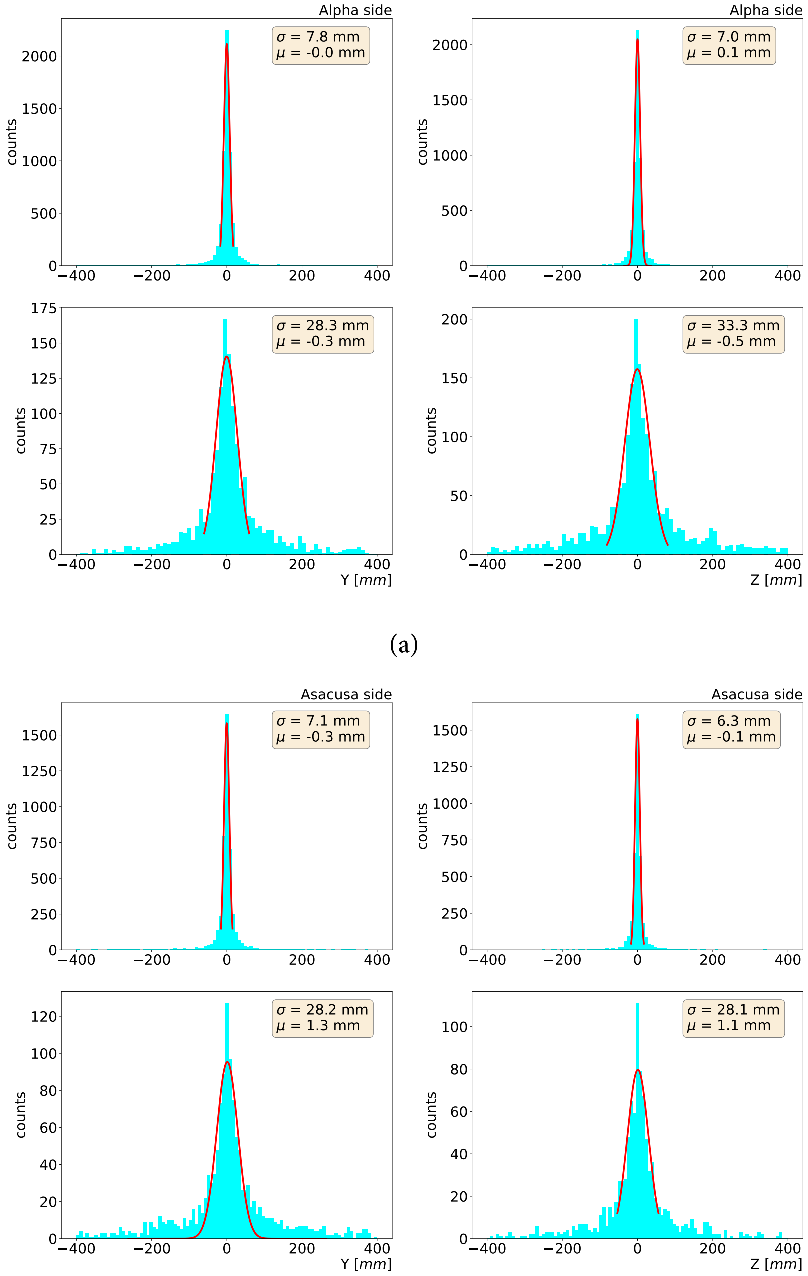

(a)

(b)

Figure B.3: (a) Intercepts distributions on the $\hat{z}\hat{y}$ plane for the Y (left) and Z (right) directions, for the ALPHA side, both for the case without (top) and with (bottom) the CUSP material, for the *real tracks* in the case with an energy cut of $0.4\,\mathrm{MeV}$. A Gaussian fit is superimposed on the histograms and its variance and mean (σ and μ) are reported. (b) Same distributions for the ASACUSA side.

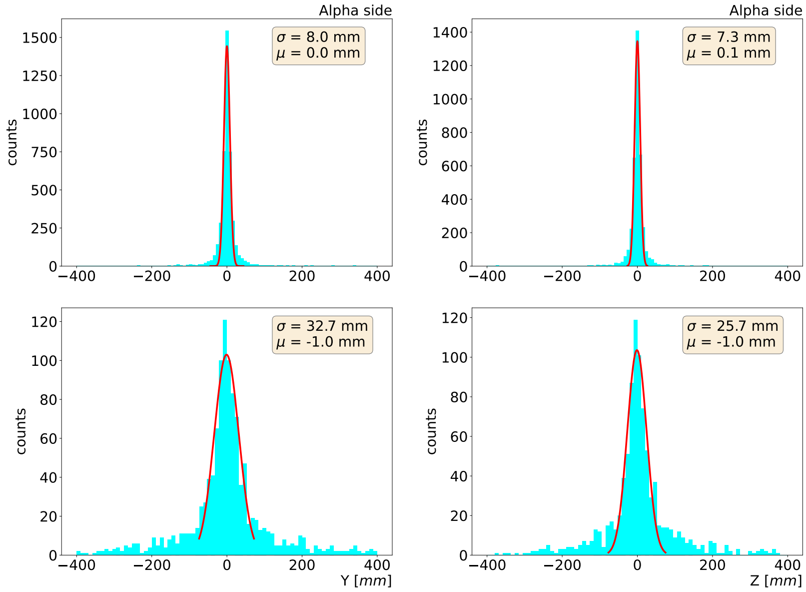

(a)

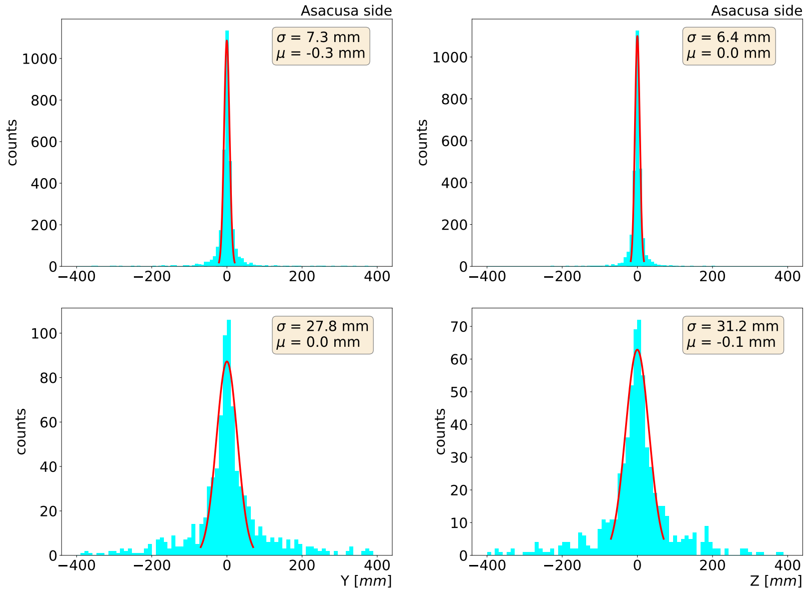

(b)

Figure B.4: (a) Intercepts distributions on the $\hat{z}\hat{y}$ plane for the Y (left) and Z (right) directions, for the ALPHA side, both for the case without (top) and with (bottom) the CUSP material, for the *real tracks* in the case with an energy cut of 1.5 MeV. A Gaussian fit is superimposed on the histograms and its variance and mean (σ and μ) are reported. (b) Same distributions for the ASACUSA side.

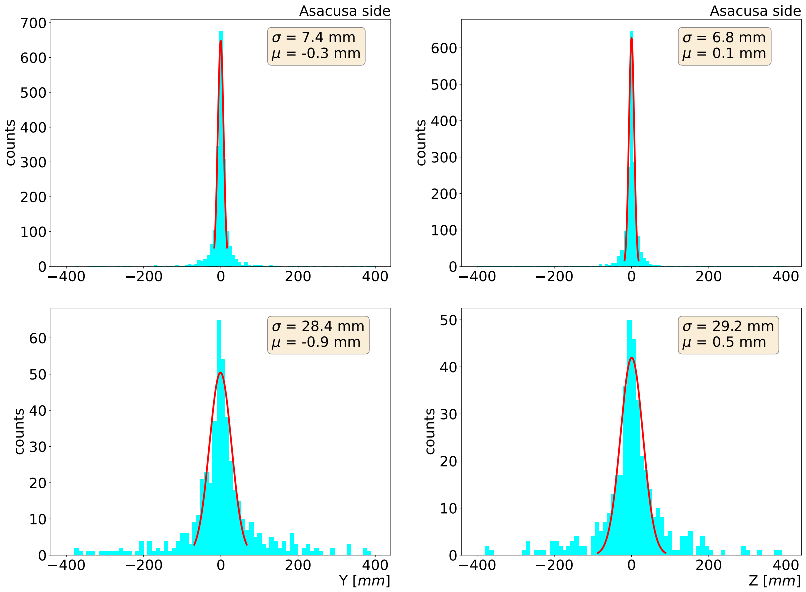

Figure B.5: Intercepts distributions on the $\hat{z}\hat{y}$ plane for the Y (left) and Z (right) directions, for the ASACUSA side, both for the case without (top) and with (bottom) the CUSP material, for the *real tracks* in the case with an energy cut of 2.7 MeV. A Gaussian fit is superimposed on the histograms and its variance and mean (σ and μ) are reported.

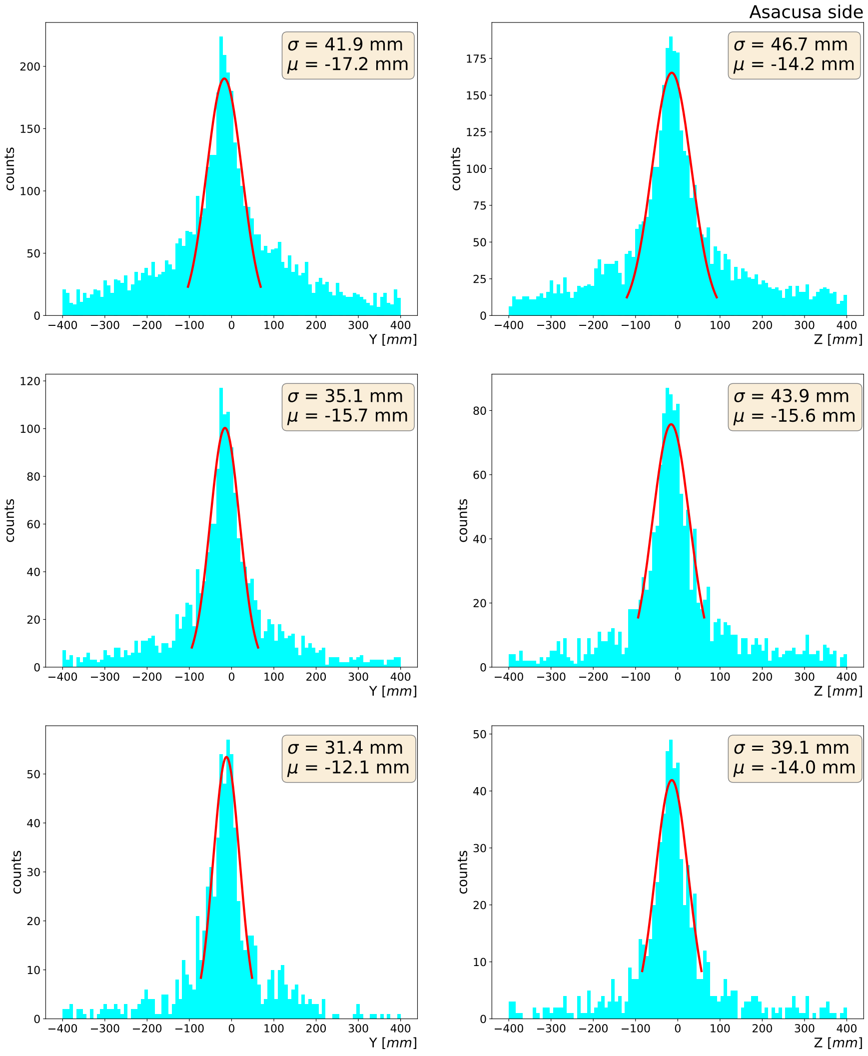

Figure B.6: Tracks intercepts on the $\hat{z}\hat{y}$ for the Z direction (left column) and Y direction (right column) reconstructed with approach (i) (see section 5.2.1 for definition) for the three energy cuts: 0.4 MeV (top), 1.5 MeV (center), 2.7 MeV (bottom), with hits on panels of the ASACUSA side. Gaussian fits are superimposed and mean and variance reported on the top right corners.

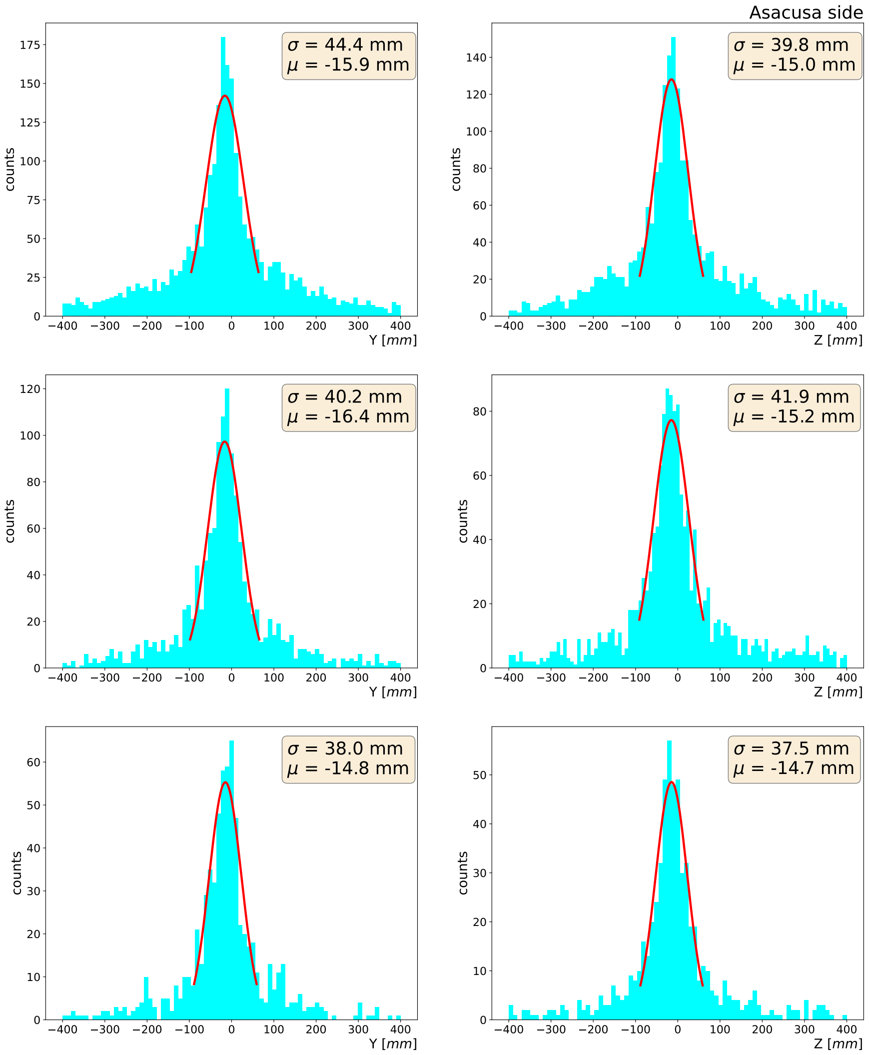

Figure B.7: Tracks intercepts on the $\hat{z}\hat{y}$ for the Z direction (left column) and Y direction (right column) reconstructed with approach (ii) (see section 5.2.1 for definition) for the three energy cuts: 0.4 MeV (top), 1.5 MeV (center), 2.7 MeV (bottom), with hits on panels of the ASACUSA side. Gaussian fits are superimposed and mean and variance reported on the top right corners.

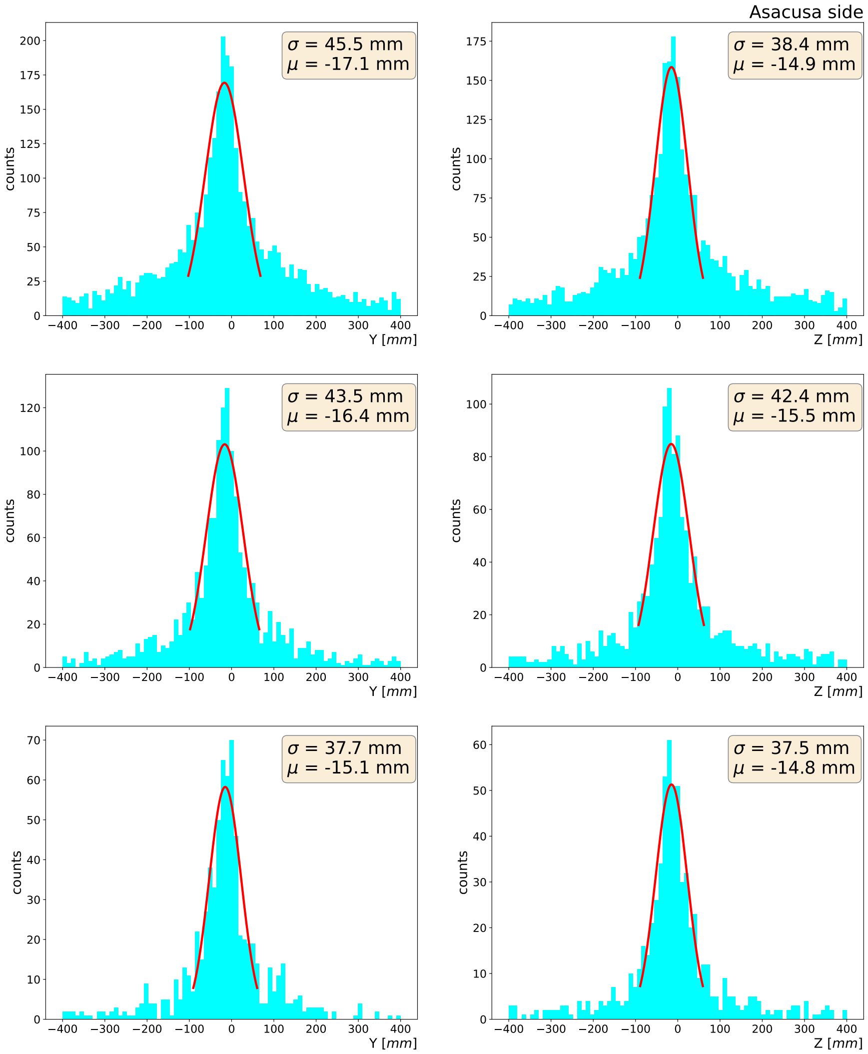

Figure B.8: Tracks intercepts on the $\hat{z}\hat{y}$ for the Z direction (left column) and Y direction (right column) reconstructed with approach *cluster* (see section 5.2.1 for definition) for the three energy cuts: 0.4 MeV (top), 1.5 MeV (center), 2.7 MeV (bottom), with hits on panels of the ASACUSA side. Gaussian fits are superimposed and mean and variance reported on the top right corners.

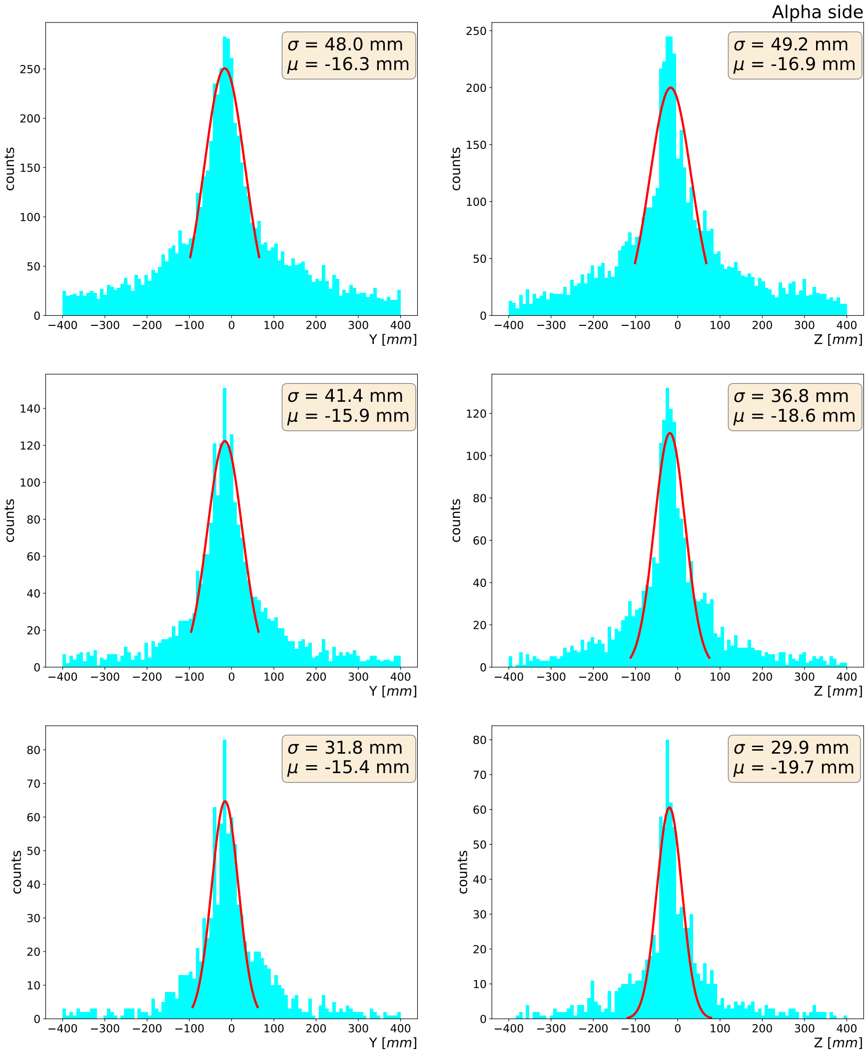

Figure B.9: Tracks intercepts on the $\hat{z}\hat{y}$ for the Z direction (left column) and Y direction (right column) reconstructed with approach (i) (see section 5.2.1 for definition) for the three energy cuts: 0.4 MeV (top), 1.5 MeV (center), 2.7 MeV (bottom), with hits on panels of the ALPHA side. Gaussian fits are superimposed and mean and variance reported on the top right corners.

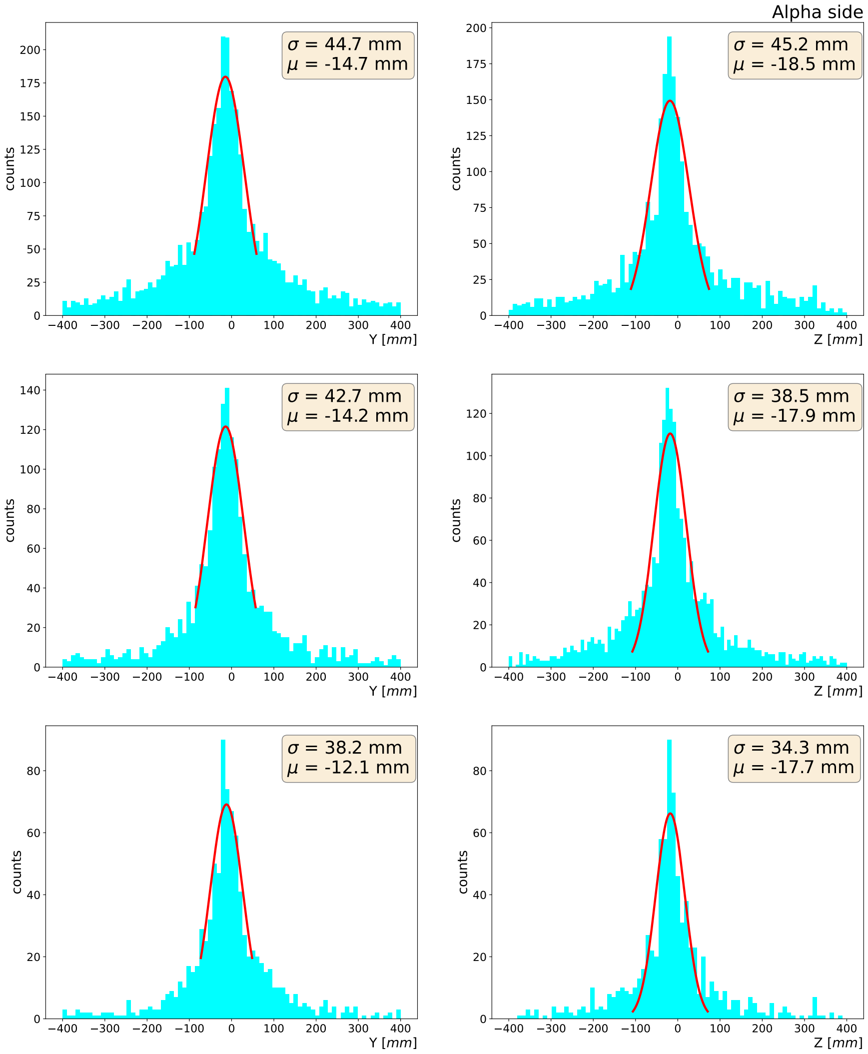

Figure B.10: Tracks intercepts on the $\hat{z}\hat{y}$ for the Z direction (left column) and Y direction (right column) reconstructed with approach (ii) (see section 5.2.1 for definition) for the three energy cuts: 0.4 MeV (top), 1.5 MeV (center), 2.7 MeV (bottom), with hits on panels of the ALPHA side. Gaussian fits are superimposed and mean and variance reported on the top right corners.

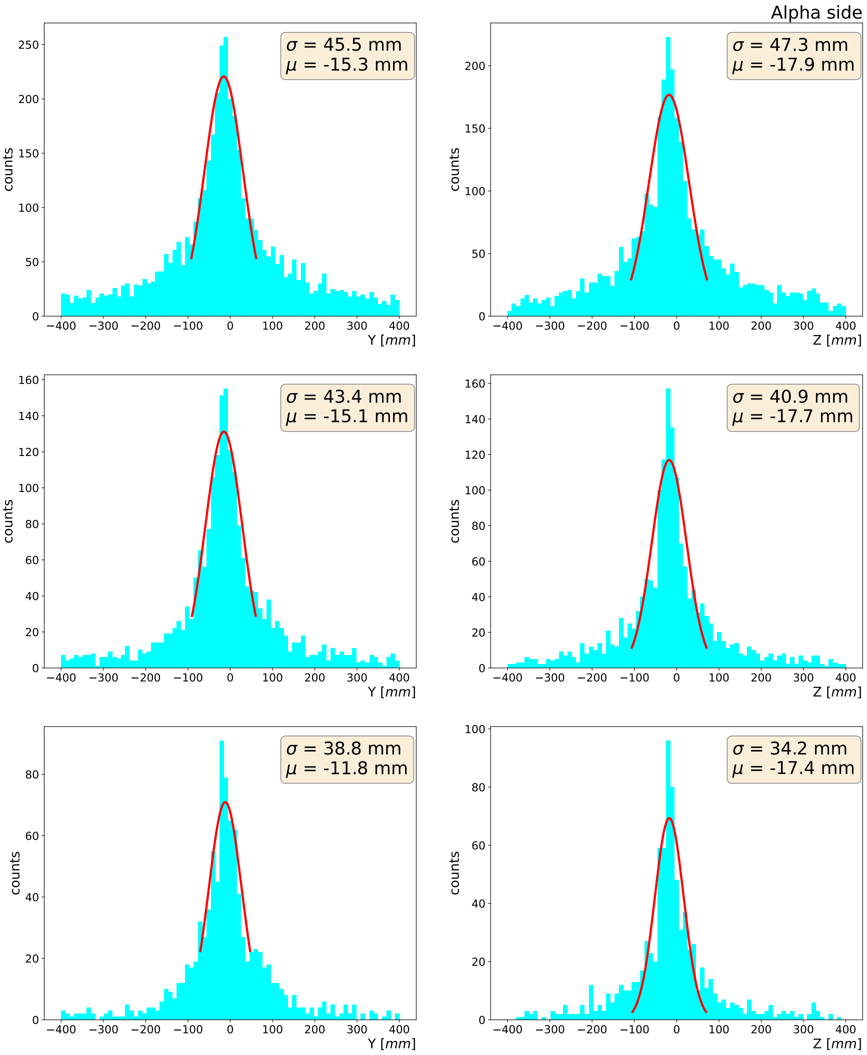

Figure B.11: Tracks intercepts on the $\hat{z}\hat{y}$ for the Z direction (left column) and Y direction (right column) reconstructed with approach *cluster* (see section 5.2.1 for definition) for the three energy cuts: 0.4 MeV (top), 1.5 MeV (center), 2.7 MeV (bottom), with hits on panels of the ALPHA side. Gaussian fits are superimposed and mean and variance reported on the top right corners.

List of Figures

List of Tables

Acronyms

AD Antiproton Decelerator. 7, 27, 29, 31, 33, 37, 111

AMT ASACUSA Micromegas Tracker. 40, 41, 44, 145

ASACUSA Antimatter Spectroscopy And Coherent Upward-going Scattering experiment. iv–vii, 1, 5, 84–87, 92, 93, 101, 104, 109, 113, 114, 116, 149–151

BGO Bismuth germanate. 19, 30, 41–44, 60, 145

BGT Buffer Gas trap. 35

BoPET Biaxially-oriented polyethylene terephthalate. 36

CPT Charge, Parity, Time. 10–18, 143, 144

DANTE Detector for Annihilation Tracking Experiment. v, vii, 19, 38, 41, 44, 45, 84–87, 92, 94–97, 106, 107, 109, 113, 115, 118, 119, 131–133, 145, 149, 150, 153, 155

ELENA Extra Low Energy Antiproton. 19, 32–34, 36, 144

FPS First Point Scientific. 33–35, 37, 144

HFS High Frquency State. 15, 19

HIP High Ionizing Particle. 26, 29, 49, 57–59, 61, 62, 64, 66–68, 75–78, 80, 96, 117, 123–125, 129, 130, 146–148, 151–153, 155

LFS Low Frquency State. 15, 19

LHC Large Hadron Collider. 31

MA-PMTs Multi-anode Photomultipliers. 43, 45, 145

MC Monte Carlo. 1, 3, 26, 30, 47, 69, 75

MIP Minimum Ionizing Particle. 22, 26, 29, 49, 57–59, 61, 62, 64, 67–69, 74–77, 79, 96, 103, 112, 117, 123, 125–129, 144, 146–148, 150, 152, 153, 155

MRE Multi Ring Electrodes. 29, 39, 40, 44, 98, 111, 145

MUSASHI Monoenergetic Ultra-Slow Antiproton Source for High-Precision Investigation. 19, 29, 30, 36, 37, 144

PM Penning-Malmberg. 39

PS Proton Synchrotron. 31

RFQD Radio frequency quadrupole decelerator. 36

SiPMs Silicon Photomultipliers. 42, 43, 45, 88–93, 149

SM Standard Model. 5, 13

SME Standard Model Extension. 14–18, 144

SPS Super Proton Synchrotron. 7

ToA Time of Arrival. 43

ToT Time over Threshold. 44

UHV Ultra High Vacuum. 43, 56

WLS Wavelength-shifting. 45, 145

Bibliography

[1] W. Tomasz. *Monte Carlo methods in HEP*. Slides online.

[2] R. Mankel. “Pattern recognition and event reconstruction in particle physics experiments”. In: *Reports on Progress in Physics* 67 (2004). DOI: `10.1088/0034-4885/67/4/R03`.

[3] P. A. M. Dirac and R. H. Fowler. “The quantum theory of the electron”. In: *Proceedings of the Royal Society of London. Series A, Containing Papers of a Mathematical and Physical Character* 117 (1928). DOI: `10.1098/rspa.1928.0023`.

[4] P. A. M. Dirac and R. H. Fowler. “The quantum theory of the Electron. Part II”. In: *Proceedings of the Royal Society of London. Series A, Containing Papers of a Mathematical and Physical Character* 118 (1928). DOI: `10.1098/rspa.1928.0056`.

[5] P. A. M. Dirac. “Quantised singularities in the electromagnetic field”. In: *Proceedings of the Royal Society of London. Series A, Containing Papers of a Mathematical and Physical Character* 133 (1931). DOI: `10.1098/rspa.1931.0130`.

[6] C. D. Anderson. “The Positive Electron”. In: *Phys. Rev.* 43 (1933). DOI: `10.1103/PhysRev.43.491`.

[7] O. Chamberlain et al. “Observation of Antiprotons”. In: *Phys. Rev.* 100 (1955). DOI: `10.1103/PhysRev.100.947`.

[8] O. Chamberlain et al. “Antiproton Star Observed in Emulsion”. In: *Phys. Rev.* 101 (1956). DOI: `10.1103/PhysRev.101.909`.

[9] MEA. Amoretti et al. “Production and detection of cold antihydrogen atoms”. In: *Nature* 419 (2002).

[10] Niels Bassler et al. “Antiproton radiotherapy”. In: *Radiotherapy and Oncology* 86 (2008). DOI: `https://doi.org/10.1016/j.radonc.2007.11.028`.

[11] G. Gabrielse et al. “Thousandfold improvement in the measured antiproton mass”. In: *Phys. Rev. Lett.* 65 (1990). DOI: `10.1103/PhysRevLett.65.1317`.

[12] S Eriksson. "Precision measurements on trapped antihydrogen in the ALPHA experiment". In: *Philosophical Transactions of the Royal Society A: Mathematical, Physical and Engineering Sciences* 376 (2018).

[13] A. Kellerbauer et al. "Proposed antimatter gravity measurement with an antihydrogen beam". In: *Nuclear Instruments and Methods in Physics Research Section B: Beam Interactions with Materials and Atoms* 266 (2008).

[14] P. Perez and A. Rosowsky. "A new path toward gravity experiments with antihydrogen". In: *Nuclear Instruments and Methods in Physics Research Section A: Accelerators, Spectrometers, Detectors and Associated Equipment* 545 (2005).

[15] C. Smorra et al. "BASE–the baryon antibaryon symmetry experiment". In: *The European Physical Journal Special Topics* 224 (2015), pp. 3055–3108.

[16] T. Aumann et al. "PUMA, antiProton unstable matter annihilation: PUMA collaboration". In: *The European Physical Journal A* 58 (2022).

[17] M. Hori et al. "Two-photon laser spectroscopy of antiprotonic helium and the antiproton-to-electron mass ratio". In: *Nature* 475 (2011). DOI: `doi.org/10.1038/nature10260`.

[18] A. Bianconi et al. "Measurement of the antiproton–nucleus annihilation cross section at 5.3 MeV". In: *Physics Letters B* 704 (2011). DOI: `10.1016/j.physletb.2011.09.069`.

[19] M. Ahmadi et al. "Observation of the hyperfine spectrum of anti-hydrogen". In: *Nature* 548 (2017). DOI: `10.1038/nature23446`.

[20] Laurent C., Marco D., and Mikhail S. "Matter and antimatter in the universe". In: *New Journal of Physics* 14 (2012). DOI: `10.1088/1367-2630/14/9/095012`.

[21] B. Kolbinger. "Machine learning for antihydrogen detection in ASACUSA". PhD thesis. Wien University, 2019.

[22] A. D Sakharov. "Violation of CP invariance, C asymmetry, and baryon asymmetry of the universe". In: *Soviet Physics Uspekhi* 34 (1991). DOI: `10.1070/PU1991v034n05ABEH002497`.

[23] M. Belén Gavela et al. "Standard model CP-violation and baryon asymmetry". In: *Modern Physics Letters A* 9 (1994).

[24] P. S. B. Dev et al. "Searches for Baryon Number Violation in Neutrino Experiments: A White Paper". In: *arXiv preprint arXiv:2203.08771* (2022).

[25] E. Widmann et al. "Hyperfine spectroscopy of hydrogen and antihydrogen in ASACUSA". In: *Hyperfine Interactions* 240 (2018). DOI: `10.1007/s10751-018-1536-9`.

[26] R. Bluhm, V. A. Kostelecký, and N. Russell. “Hydrogen and antihydrogen spectroscopy for studies of CPT and Lorentz symmetry”. In: *AIP Conference Proceedings* 457 (1999). DOI: `10.1063/1.57439`.

[27] R. Bluhm. “Probing the Planck scale in low-energy atomic physics”. In: *2nd Meeting on CPT and Lorentz Symmetry*. 2002, pp. 16–25. DOI: `10.1142/9789812778123_0003`. arXiv: `hep-ph/0111323`.

[28] V. A. Kostelecký and A. J. Vargas. “Lorentz and CPT tests with hydrogen, antihydrogen, and related systems”. In: *Phys. Rev. D* 92 (2015). DOI: `10.1103/PhysRevD.92.056002`.

[29] D. Colladay and V. A. Kostelecký. “CPT violation and the Standard Model”. In: *Phys. Rev. D* 55 (1997). DOI: `10.1103/PhysRevD.55.6760`.

[30] J. Beringer et al. “Review of Particle Physics”. In: *Phys. Rev. D* 86 (2012). DOI: `10.1103/PhysRevD.86.010001`.

[31] S. Ulmer et al. “High-precision comparison of the antiproton-to-proton charge-to-mass ratio”. In: *Nature* 524 (2015). DOI: `10.1038/nature14861`.

[32] D. Griffiths. *Introduction to elementary particles*. John Wiley & Sons, 2020.

[33] H. Hellwig et al. “Measurement of the Unperturbed Hydrogen Hyperfine Transition Frequency”. In: *IEEE Transactions on Instrumentation and Measurement* 19 (1970). DOI: `10.1109/TIM.1970.4313902`.

[34] S. G. Karshenboim. “Some possibilities for laboratory searches for variations of fundamental constants”. In: *Canadian Journal of Physics* 78 (2000). DOI: `10.1139/p00-045`.

[35] A. G. Prodell and P. Kusch. “The Hyperfine Structure of Hydrogen and Deuterium”. In: *Phys. Rev.* 88 (1952). DOI: `10.1103/PhysRev.88.184`.

[36] P. Kusch. “Redetermination of the Hyperfine Splittings of Hydrogen and Deuterium in the Ground State”. In: *Phys. Rev.* 100 (1955). DOI: `10.1103/PhysRev.100.1188`.

[37] M. Diermaier et al. “In-beam measurement of the hydrogen hyperfine splitting and prospects for antihydrogen spectroscopy”. In: *Nature Communications* 8 (2017). DOI: `10.1038/ncomms15749`.

[38] G. Breit and I. I. Rabi. “Measurement of Nuclear Spin”. In: *Phys. Rev.* 38 (1931). DOI: `10.1103/PhysRev.38.2082.2`.

[39] A. Tureanu. “CPT and Lorentz invariance: Their relation and violation”. In: *Journal of Physics: Conference Series*. Vol. 474. 2013.

[40] V. A. Kostelecký and M. Mewes. “Fermions with Lorentz-violating operators of arbitrary dimension”. In: *Phys. Rev. D* 88 (2013). DOI: `10.1103/PhysRevD.88.096006`.

[41] C. Malbrunot et al. “The ASACUSA antihydrogen and hydrogen program: results and prospects”. In: *Philosophical Transactions of the Royal Society A: Mathematical, Physical and Engineering Sciences* 376 (2018). DOI: `10.1098/rsta.2017.0273`.

[42] I. I. Rabi et al. “A New Method of Measuring Nuclear Magnetic Moment”. In: *Phys. Rev.* 53 (1938). DOI: `10.1103/PhysRev.53.318`.

[43] B. Kolbinger et al. “Measurement of the principal quantum number distribution in a beam of antihydrogen atoms”. In: *The European Physical Journal D* 75 (2021). DOI: `10.1140/epjd/s10053-021-00101-y`.

[44] C. Amsler et al. “Reducing the background temperature for cyclotron cooling in a cryogenic Penning-Malmberg trap”. In: *Physics of Plasmas* 29 (2022). DOI: `10.1063/5.0093360`.

[45] V. Kraxberger et al. “Upgrade of ASACUSA’s antihydrogen detector”. In: *Nuclear Instruments and Methods in Physics Research Section A: Accelerators, Spectrometers, Detectors and Associated Equipment* 1045 (2023). DOI: `https://doi.org/10.1016/j.nima.2022.167568`.

[46] A. Gligorova. “Development of and data analysis of a position detector for AEg IS (Antimatter Experiment: Gravity, Interferometry, Spectroscopy)”. PhD thesis. Bergen University, 2014.

[47] R. Marshall. “Electron-positron annihilation at high energies”. In: *Reports on Progress in Physics* 52 (1989). DOI: `10.1088/0034-4885/52/11/001`.

[48] A.J. Apostolakis et al. “The annihilation of antiprotons on protons and neutrons”. In: *Il Nuovo Cimento* 37 (1965). DOI: `10.1007/BF02783345`.

[49] T. Armstrong et al. “Measurement of antineutron-proton total and annihilation cross sections from 100 to 500 MeV/c”. In: *Phys. Rev. D* 36 (1987). DOI: `10.1103/PhysRevD.36.659`.

[50] G. Bendiscioli and D. Kharzeev. “Antinucleon-nucleon and antinucleon-nucleus interaction. A review of experimental data”. In: *La Rivista Del Nuovo Cimento Series 3* (1994). DOI: `10.1007/BF02724447`.

[51] V. Girija and F. Tabakin. “Baryon exchange model for $\bar{p}p$ annihilation into strange mesons”. In: *Phys. Rev. C* 34 (1986). DOI: `10.1103/PhysRevC.34.1798`.

[52] J. Harte, R.H. Socolow, and J. Vandermeulen. “A study of the quark rearrangement model of nucleon-antinucleon annihilation”. In: *Il Nuovo Cimento A* 49 (1967).

[53] B. Moussallam. “$\bar{p}p \to \pi\pi$ in a baryon-exchange-potential model”. In: *Nuclear Physics A* 429 (1984). DOI: `10.1016/0375-9474(84)90690-0`.

[54] J. Haidenbauer, T. Hippchen, and K. Holinde. “The bonn $N\bar{N}$ potential and the range of $N\bar{N}$ annihilation”. In: *Nuclear Physics A* 508 (1990). DOI: `10.1016/0375-9474(90)90493-6`.

[55] E. Klempt, C. Batty, and J. Richard. “The antinucleon-nucleon interaction at low energy; annihilation dynamics”. In: *Physics Reports* 413 (2005). DOI: `10.1016/j.physrep.2005.03.002`.

[56] V. Mull et al. “Meson-baryon dynamics in the nucleon-antinucleon system. II. Annihilation into two mesons”. In: *Phys. Rev. C* 44 (1991). DOI: `10.1103/physrevc.44.1337`.

[57] T. Hippchen et al. “Meson-baryon dynamics in the nucleon-antinucleon system. I. the nucleon-antinucleon interaction”. In: *Phys. Rev. C* 44 (1991). DOI: `10.1103/physrevc.44.1323`.

[58] V. Mull and K. Holinde. “Combined description of anti-N N scattering and annihilation with a hadronic model”. In: *Phys. Rev. C* 51 (1995). DOI: `10.1103/physrevc.51.2360`.

[59] H.R. Rubinstein and H. Stern. “Nucleon-antinucleon annihilation in the quark model”. In: *Physics Letters* 21 (1966). DOI: `10.1016/0031-9163(66)90526-9`.

[60] M. Maruyama and T. Ueda. “$N\bar{N}$ annihilation at low energies in a quark rearrangement model and decay widths of $N\bar{N}$ bound states”. In: *Nuclear Physics A* 364 (1981). DOI: `10.1016/0375-9474(81)90573-X`.

[61] M. Maruyama and T. Ueda. “A quark rearrangement model with spatial overlap function for low energy $N\bar{N}$ annihilation”. In: *Physics Letters B* 124 (1983). DOI: `10.1016/0370-2693(83)91417-X`.

[62] M. Kohno and W. Weise. “Quark model description of low energy proton–antiproton annihilation into two mesons”. In: *Physics Letters B* 152 (1985). DOI: `10.1016/0370-2693(85)90500-3`.

[63] S. Furui, A. Faessler, and S.B. Khadkikar. “$p\bar{p}$ annihilation at rest into mesons in the quark rearrangement model and the quark annihilation model”. In: *Nuclear Physics A* 424 (1984). DOI: `10.1016/0375-9474(84)90007-1`.

[64] J. Vandermeulen. “$N\bar{N}$ annihilation creates two mesons”. In: *Zeitschrift für Physik C Particles and Fields* 37 (1988). DOI: `10.1007/BF01549715`.

[65] A.S. Iljinov, V.I. Nazaruk, and S.E. Chigrinov. “Nuclear absorption of stopped antiprotons: Multipion-nucleus interactions”. In: *Nuclear Physics A* 382 (1982). DOI: `10.1016/0375-9474(82)90352-9`.

[66] J. Rafelski. “$\bar{p}$ annihilation on heavy nuclei”. In: *Physics Letters B* 91 (1980). DOI: `10.1016/0370-2693(80)90450-5`.

[67] A. Boudard et al. “New potentialities of the Liège intranuclear cascade model for reactions induced by nucleons and light charged particles”. In: *Phys. Rev. C* 87 (2013). DOI: `10.1103/PhysRevC.87.014606`.

[68] A.S. Botvina, Iljinov, and A.S. Mishustin I.N. et al. “Statistical simulation of the break-up of highly excited nuclei”. In: *Nuclear Physics A* 475 (1987). DOI: `10.1016/0375-9474(87)90232-6`.

[69] C. Guaraldo. “Low energy antiproton-nucleus annihilation”. In: *Nuclear Physics B - Proceedings Supplements* 8 (1989).

[70] I. Dostrovsky, Z. Fraenkel, and G. Friedlander. “Monte Carlo calculations of nuclear evaporation processes. III. Applications to low-energy reactions”. In: *Physical Review* 119 (1959). DOI: `10.1103/PhysRev.119.2098.2`.

[71] J.P. Bondorf et al. “Statistical multifragmentation of nuclei: (I). Formulation of the model”. In: *Nuclear Physics A* 443 (1985). DOI: `10.1016/0375-9474(85)90266-0`.

[72] J. Bondorf et al. “Statistical multifragmentation of nuclei: (II). Application of the model to finite nuclei disassembly”. In: *Nuclear Physics A* 444 (1985). DOI: `10.1016/0375-9474(85)90463-4`.

[73] H.W. Barz et al. “Statistical multifragmentation of nuclei: (III). Decay of the fragments”. In: *Nuclear Physics A* 448 (1986). DOI: `10.1016/0375-9474(86)90440-9`.

[74] B.M. Pontecorvo. “One-meson and zero-meson annihilation of antinucleons”. In: *Zh.Eksp.Teor.Fiz.* 30 (1956).

[75] J. Riedlberger et al. “Antiproton annihilation at rest in nitrogen and deuterium gas”. In: *Phys. Rev. C* 40 (1989). DOI: `10.1103/PhysRevC.40.2717`.

[76] C. Amsler and et al. “First observations of Pontecorvo reactions with a recoiling neutron”. In: *Zeitschrift für Physik A Hadrons and Nuclei* 351 (1995). DOI: `10.1007/BF01290916`.

[77] L.A. Kondratyuk and M.G. Sapozhnikov. “Pontecorvo reactions of two-body antiproton annihilation in deuterium”. In: *Physics Letters B* 220 (1989). DOI: `10.1016/0370-2693(89)90882-4`.

[78] S. Aghion et al. “Measurement of antiproton annihilation on Cu, Ag and Au with emulsion films”. In: *Journal of Instrumentation* 12 (2017). DOI: `10.1088/1748-0221/12/04/p04021`.

[79] S. Aghion et al. “Detection of low energy antiproton annihilations in a segmented silicon detector”. In: *Journal of Instrumentation* 9 (2014). DOI: `10.1088/1748-0221/9/06/p06020`.

[80] S. Aghion et al. “Prospects for measuring the gravitational free-fall of antihydrogen with emulsion detectors”. In: *Journal of Instrumentation* 8 (2013). DOI: `10.1088/1748-0221/8/08/p08013`.

[81] D. Polster et al. “Light particle emission induced by stopped antiprotons in nuclei: Energy dissipation and neutron-to-proton ratio”. In: *Phys. Rev. C* 51 (1995). DOI: `10.1103/PhysRevC.51.1167`.

[82] P. Hofmann et al. “Charged-particle spectra from antiproton annihilation at rest in a = 12–238 nuclei”. In: *Nuclear Physics A* 512 (1990). DOI: `10.1016/0375-9474(90)90229-F`.

[83] H. S. Plendl et al. “Antiproton-nucleus annihilation at rest”. In: *Physica Scripta* 48 (1993). DOI: `10.1088/0031-8949/48/2/006`.

[84] E. Moser et al. “Yields of residual nuclei after antiproton annihilation in ^{95}Mo and ^{98}Mo”. In: *Physics Letters B* 179 (1986). DOI: `10.1016/0370-2693(86)90429-6`.

[85] T. von Egidy et al. “Yield of residual nuclei after antiproton annihilation in Ba”. In: *Zeitschrift für Physik A Atomic Nuclei* 335 (1990). DOI: `10.1007/BF01290193`.

[86] E. F. Moser et al. “Residual nuclei after antiproton annihilation in Mo and Ho”. In: *Zeitschrift für Physik A Atomic Nuclei* (1989).

[87] P. Lubinski et al. “Neutron Halo in Heavy Nuclei from Antiproton Absorption”. In: *Physical Review Letters* 73 (1994). DOI: `10.1103/PhysRevLett.73.3199`.

[88] J. Jastrzebski et al. “Signature of a neutron halo in ^{232}Th from antiproton absorption”. In: *Nuclear Physics A* 558 (1993). DOI: `10.1016/0375-9474(93)90409-Q`.

[89] M. Chiba et al. “Pontecorvo reactions in antiproton annihilation at rest in deuterium to $\pi^0 n$, $\pi^0\Delta^0$, ηn and $\eta\Delta^0$”. In: *Phys. Rev. D* 55 (1997). DOI: `10.1103/PhysRevD.55.2577`.

[90] O. Gorchakov et al. “Measurement of the $\bar{p}d \to \varphi n$ Pontecorvo reaction for antiproton annihilation at rest”. In: *Physics Letters B* 528 (2002). DOI: `10.1016/S0370-2693(02)01175-9`.

[91] J. Cugnon et al. “Antiproton and antilambda annihilations on several nucleons”. In: *Phys. Rev. C* 39 (1989). DOI: `10.1103/PhysRevC.39.181`.

[92] C. Amsler. “Nucleon-antinucleon annihilation at LEAR”. In: *ArXiv* (2019). URL: `http://arxiv.org/abs/1908.08455`.

[93] N. Kuroda et al. “Development of a monoenergetic ultraslow antiproton beam source for high-precision investigation”. In: *Physical Review Special Topics - Accelerators and Beams* 15 (2012). DOI: `10.1103/PhysRevSTAB.15.024702`.

[94] P. V. Degtyarenko et al. "Chiral invariant phase space event generator". In: *The European Physical Journal A* 8 (2000). DOI: `10.1007/s100500070108`.

[95] M. Kossov. "Simulation of antiproton-nuclear annihilation at rest". In: *IEEE Transactions on Nuclear Science* 52 (2005). DOI: `10.1109/TNS.2005.862878`.

[96] B. Andersson et al. "A model for low-pT hadronic reactions with generalizations to hadron-nucleus and nucleus-nucleus collisions". In: *Nuclear Physics B* 281 (1987). DOI: `10.1016/0550-3213(87)90257-4`.

[97] B. Nilsson-Almqvist et al. "Interactions between hadrons and nuclei: The Lund Monte Carlo - FRITIOF version 1.6 -". In: *Computer Physics Communications* 43 (1987). DOI: `10.1016/0010-4655(87)90056-7`.

[98] A. Galoyan et al. "Simulations of light antinucleus–nucleus interactions". In: *Hyperfine Interactions* 215 (2013). DOI: `10.1007/s10751-013-0780-2`.

[99] "The FLUKA Code: Developments and Challenges for High Energy and Medical Applications". In: *Nuclear Data Sheets* 120 (2014). DOI: `doi.org/10.1016/j.nds.2014.07.049`.

[100] H. Poth. "Electron cooling: Theory, experiment, application". In: *Physics Reports* 196 (1990). DOI: `https://doi.org/10.1016/0370-1573(90)90040-9`.

[101] J. H. Malmberg and J. S. deGrassie. "Properties of Nonneutral Plasma". In: *Phys. Rev. Lett.* 35 (1975). DOI: `10.1103/PhysRevLett.35.577`.

[102] C. Amsler et al. "Injection and capture of antiprotons in a Penning-Malmberg trap using a drift tube accelerator and degrader foil". In: (). in preparation.

[103] N. Kuroda. "Accumulation of a large number of antiprotons and production of an ultra-slow antiproton beam". PhD thesis. University of Tokyo, 2003.

[104] M. Tajima. "Development of injection scheme of antiprotons and production of antihydrogen atoms in low-lying excited states". PhD thesis. University of Tokyo, 2017.

[105] A. Mohri and Y. Yamazaki. "A possible new scheme to synthesize antihydrogen and to prepare a polarised antihydrogen beam". In: *Europhysics Letters* 63 (2003). DOI: `10.1209/epl/i2003-00509-0`.

[106] F. Robicheaux. "Atomic processes in antihydrogen experiments: a theoretical and computational perspective". In: *Journal of Physics B: Atomic, Molecular and Optical Physics* 41 (2008). DOI: `10.1088/0953-4075/41/19/192001`.

[107] B. Radics et al. "Scaling behavior of the ground-state antihydrogen yield as a function of positron density and temperature from classical trajectory Monte Carlo simulations". In: *Physical Review A - Atomic, Molecular, and Optical Physics* 90 (2014). DOI: `10.1103/PhysRevA.90.032704`.

[108] G. Gabrielse. "Atoms Made Entirely of Antimatter: Two Methods Produce Slow Antihydrogen". In: *Adances in atomic, molecular, and optical physics* (2004).

[109] G. Baur et al. "Production of antihydrogen". In: *Physics Letters B* 368 (1996). DOI: `10.1016/0370-2693(96)00005-6`.

[110] Y. Nagata and Yasunori Yamazaki. "A novel property of anti-Helmholz coils for in-coil syntheses of antihydrogen atoms: Formation of a focused spin-polarized beam". In: *New Journal of Physics* 16 (2014). DOI: `10.1088/1367-2630/16/8/083026`.

[111] T. F. Gallagher. *Rydberg Atoms*. Vol. 91. Cambridge Monographs on Atomic, Molecular and Chemical Physics. Cambridge University Press, 1994. DOI: `10.1017/CBO9780511524530`.

[112] G. Gabrielse et al. "Driven Production of Cold Antihydrogen and the First Measured Distribution of Antihydrogen States". In: *Physical Review Letters* 89 (2002). DOI: `10.1103/PhysRevLett.89.233401`.

[113] C. Sauerzopf et al. "Annihilation detector for an in-beam spectroscopy apparatus to measure the ground state hyperfine splitting of antihydrogen". In: *Nucl. Instrum. Meth. A* (2016). DOI: `10.1016/j.nima.2016.06.023`.

[114] Y Nagata et al. "Physical Society of Japan: The development of the antihydrogen beam detector: Toward the three dimensional tracking with a BGO crystal and a hodoscope". In: *JPS Conf. Proc.* Vol. 18. 2017.

[115] Y. Nagata et al. "Direct detection of antihydrogen atoms using a BGO crystal". In: *Nuclear Instruments and Methods in Physics Research, Section A: Accelerators, Spectrometers, Detectors and Associated Equipment* 89 (2016). DOI: `10.1016/j.nima.2016.10.019`.

[116] T. Poikela et al. "Timepix3: a 65k channel hybrid pixel readout chip with simultaneous ToA/ToT and sparse readout". In: *Journal of Instrumentation* 9 (2014). DOI: `10.1088/1748-0221/9/05/C05013`.

[117] B. Radics et al. "The ASACUSA Micromegas Tracker: A cylindrical, bulk Micromegas detector for antimatter research". In: *Review of Scientific Instruments* 86 (2015). DOI: `10.1063/1.4927685`.

[118] V. Mackel et al. "Imaging antimatter with a Micromegas detector". In: *Nuclear Instruments and Methods in Physics Research, Section B: Beam Interactions with Materials and Atoms* 422 (2018). DOI: `10.1016/j.nimb.2018.02.026`.

[119] M. Corradini et al. "Scintillating bar detector for antiproton annihilations measurements". In: *Hyperfine Interactions* 233.1 (2015). DOI: `doi.org/10.1007/s10751-015-1181-5`.

[120] G. Lutz. *Semiconductor Radiation Detectors*. Springer, 1999.

[121] L. Rossi et al. *Pixel detectors: From fundamentals to applications*. Springer Science & Business Media, 2006.

[122] C. H. Wang, K. Misiakos, and A. Neugroschel. "Minority-carrier transport parameters in n-type silicon". In: *IEEE transactions on electron devices* 37 (1990).

[123] K. N. Sjøbæk. "Full simulation of a testbeam experiment including modeling of the Bonn Atlas Telescope and Atlas 3D pixel silicon sensors". MA thesis. 2010.

[124] H. Holmestad. "Data analysis, simulations, and reconstruction of antiproton annihilations in a silicon pixel detector". PhD thesis. Oslo University, 2018. URL: `http://cds.cern.ch/record/2670395`.

[125] W. Shockley. "Currents to conductors induced by a moving point charge". In: *Journal of applied physics* 9 (1938). DOI: `https://doi.org/10.1063/1.1710367`.

[126] M. Hori and E. Widmann. *ASACUSA status report - recent progress and plans for 2018*. Tech. rep. CERN, 2018. URL: `http://cds.cern.ch/record/002300138`.

[127] T.E.J. Campbell-Ricketts, M. Kroupa, and L.S. Pinsky. "Spectroscopy of high-energy ions with Timepix3". In: *Journal of Instrumentation* 11 (2016). DOI: `10.1088/1748-0221/11/11/P11007`.

[128] C. Granja et al. "Response of the pixel detector Timepix to heavy ions". In: *Nuclear Instruments and Methods in Physics Research Section A: Accelerators, Spectrometers, Detectors and Associated Equipment* 633 (2011). DOI: `https://doi.org/10.1016/j.nima.2010.06.166`.

[129] S. M. Abu Al Azm et al. "Response of timepix detector with GaAs:Cr and Si sensor to heavy ions". In: *Physics of Particles and Nuclei Letters* 13 (2016). DOI: `10.1134/S154747711603002X`.

[130] S. Spannagel et al. "Allpix2: A modular simulation framework for silicon detectors". In: *Nucl. Instr. Meth. A* (2018). DOI: `10.1016/j.nima.2018.06.020`.

[131] S. Spannagel, K. Wolters, and P. Schütze. *Allpix Squared - Generic Pixel Detector Simulation Framework (2.2.0)*. 2022. DOI: `10.5281/zenodo.6387859`.

[132] M. Hori and E. Widmann. *ASACUSA status report - recent progress and plans for 2020*. Tech. rep. CERN, 2020. URL: `http://cds.cern.ch/record/2706194`.

[133] H. Aghai-Khozani et al. "Limits on antiproton-nuclei annihilation cross sections at 125 keV". In: *Nuclear Physics A* 1009 (2021).

[134] H. Aghai-Khozani et al. "First measurement of the antiproton-nucleus annihilation cross section at 125 keV". In: *Hyperfine Interactions* 234 (2015). DOI: `10.1007/s10751-015-1172-6`.

[135] H. Aghai-Khozani et al. “First experimental detection of antiproton in-flight annihilation on nuclei at 130 keV”. In: *The European Physical Journal Plus* 127 (2012). DOI: `10.1140/epjp/i2012-12125-8`.

[136] G. Costantini et al. “The upgrade of the ASACUSA scintillating bar detector for antiproton annihilation measurements”. In: *Journal of Instrumentation* 18 (2023).

[137] *Passage of Particles Through Matter*. URL: `https://pdg.lbl.gov/2022/reviews/rpp2022-rev-passage-particles-matter.pdf`.

[138] *Allpix^2 User Manual*. URL: `https://project-allpix-squared.web.cern.ch/usermanual/allpix-manual.pdf`.

Ringraziamenti

Al fondo (o all'inizio) di una tesi si suole metter dei ringraziamenti e seppur non sia bravo in questo, non voglio esimermi dal farlo. Vi sono alcuni ringraziamenti più formali, come quelli che devo al mio supervisore Luca Venturelli per l'opportunità di questo dottorato e altri meno formali come quelli ai miei colleghi Valerio, Marco, Giulia e Stefano e ai colleghi di Milano e d'oltr'alpe che hanno arricchito l'esperienza tutta. In particolare vorrei ringraziare Andreas, per la spontaneità e leggerezza con cui mi ha accolto e guidato al CERN.

Alla terza tesi poi potrà iniziare a sembrare banale o forse scontato spendersi in ringraziamenti per alcune persone che ci sono da sempre. Tuttavia, alcune di queste non smettono mai di meritarseli e a loro devo molto di più di qualche riga scritta al fondo di uno scritto. La persona più importante che vorrei ringraziare è Ilaria, per essermi stata accanto negli ultimi 7 anni e per avermi supporto in quella che per me, è stata un'avventura faticosa e quasi mai facile da affrontare. Le devo veramente tutto e lei ha dovuto sopportare veramente tanto. Vorrei lasciare un ringraziamento anche ai miei frattelli, Giulio, Mattia ed Andrea e ai miei genitori Walter e Letizia, per volermi bene nonostante i miei silenzi, il mio essere introverso e le mie altre difficoltà, in breve nonstante l'essere me. Infine mi sento in debito di ringraziamento anche verso alcuni amici cari, come Lore e Kito, che nonostante strade diverse, riescono ad essermi sempre vicino.

Ci sono altre persone che vorrei ringraziare perchè anche senza vederle periodicamente mi fan sentire fortunato ad avere la vita che ho. Tuttavia, come i migliori indecisi, rimango interdetto sul chi e quanti dovrei nominare. Mi limito quindi a rassicurarvi che un pensiero va a molte persone. Anche ad alcune che forse non si aspetterebbero nemmeno di essere stati influenti.

Aknowlegments

At the bottom (or beginning) of a dissertation it is customary to put thanks, and while I am not good at this, I do not want to shy away from doing so. There are some more formal thanks, such as those I owe to my supervisor Luca for the opportunity of this Ph.D. and some less formal ones such as those to my colleagues Valerio, Marco, Giulia and Stefano and those from Milano and beyond the Alps who enriched the whole experience. In particular I would like to thank Andreas, for the spontaneity and lightness with which he welcomed and guided me to CERN.

At the third thesis then it may begin to seem trivial or perhaps meaningless to spend in thanks for some people who have always been with me. However, some of these never cease to deserve them, and to them I owe much more than a few lines written at the bottom of a paper. The most important person I would like to thank is Ilaria, for being by my side for the past 7 years and supporting me in what for me, has been an exhausting and almost never easy adventure to face. I truly owe her everything and she has truly had to endure so much. I would also like to thank my brothers, Giulio, Mattia and Andrea and my parents, for loving me despite my silences, my being introverted and all my difficulties, in short despite me being me. Finally, I also feel I owe thanks to some dear friends, such as Lore and Kito, who despite different paths, always manage to be close to me.

There are other people I would like to thank, since even without seeing them periodically they make me fortunate to have the life I have. However, like the best indecisive people, I remain hesitant about who and how many I should name. I will simply end by reassuring you all that a thought goes to many people. Even to people that perhaps would not even expect to have been influential.